Massive stars on the main sequence

Dissertation

zur

Erlangung des Doktorgrades (Dr. rer. nat.)

der

Mathematisch-Naturwissenschaftlichen Fakultät

der

Rheinischen Friedrich-Wilhelms-Universität Bonn

vorgelegt von

Karen Köhler

aus

Karl-Marx-Stadt

Bonn 2017

Angefertigt mit Genehmigung der Mathematisch-Naturwissenschaftlichen Fakultät
der Rheinischen Friedrich-Wilhelms-Universität Bonn

1. Gutachter: Prof. Dr. Norbert Langer

2. Gutachter: Prof. Dr. Thomas H. Reiprich

Tag der Promotion: 14.12.2016

Erscheinungsjahr: 2017

Zusammenfassung / summary of doctoral thesis

Massive stars have a strong influence on their environment by chemical enrichment of the surrounding interstellar medium due to strong stellar winds. The influence of mass loss and rotation on the main-sequence evolution of massive stars is studied in this thesis with the focus on stars more massive than 100 $M_{\odot}$.

In Section 2, a method is presented to determine age and inclination angle of stars based on their surface nitrogen enhancement (published in Köhler et al. (2012)). The derived equations are based on stellar evolution models of Brott et al. (2011a) for rotating single stars. The method is applied to early B-type main-sequence stars (LMC: NGC 2004 and N 11; SMC: NGC 330 and NGC 346). Age constrained are derived for 17 stars. For 10 of these 17 stars, the method lines out that they can not be explained by rotational mixing in single stars. For stars, were only upper limits of the surface nitrogen abundance could be derived, the method can be used to deduce limits to their inclination angles.

In Section 3 detailed stellar evolution models of rotating very massive single stars are presented with initial masses of 70–500 $M_{\odot}$ and surface rotational velocities up to 550 km/s, assuming LMC metallicity (published in Köhler et al. (2015)). Very massive stars are strongly affected by mass loss. Until the end of the main-sequence phase, they lose more than 50% of their initial mass. For stars initially more massive than 160 $M_{\odot}$, mass loss becomes the main trigger to chemical homogeneous evolution, even for slow rotating stars. Additionally, the strong increase in mass loss at 25 000K leads to the truncation of the red-ward evolution for stars initially more massive than 80 $M_{\odot}$. All presented models reach the Eddington limit in the stellar envelope during hydrogen burning, what leads to envelope inflation.

Synthetic populations of stars are presented in Section 4 based on stellar evolution models presented in Section 3 and models published in Brott et al. (2011a), using the population synthesis code Starmaker (Brott et al. 2011b). The populations are calculated for two different initial distributions. First, the distributions are based on the observational data of the VLT-FLAMES Tarantula Survey (main-sequence stars; spectral type: O7–O2) assuming star bursts of one, two, three and five Myr old stars. Second, flat distributions in initial rotation rates and initial masses are applied, assuming continuous star formation. Based on the simulation results, the probability to observe evolutionary features related to mass loss and rotational mixing in very massive stars are derived (for example rapidly rotating stars in the Hertzprung-Russell diagram). First comparisons to a sub-sample of the VLT-FLAMES Tarantula Survey are presented (main-sequence stars of spectral type O7–O2).

Contents

1. Introduction

1.1. Massive stars

Within this work, stars with initial masses above 8 $M_{\odot}$ are referred to as massive stars. They are progenitors of core-collapse supernovae and gamma-ray bursts. Observationally massive stars relate zo the OB-type stars, Wolf-Rayet stars and later type supergiants.

Massive stars strongly affect their environment. They significantly influence the formation of stars and planets (Bally et al. 2005) as well as the structure and evolution of galaxies (Kennicutt 1998). For example, massive stars affect the temperature and structure of the surrounding interstellar medium by chemical enrichment, due to strong stellar winds, and ultra-violet radiation.

Even until know, the formation, evolution and death of massive stars are uncertain and discussed extensively. The formation process of massive stars is difficult to study due to extinction, rapidity of the formation process, and by their small number in stellar populations. Mass loss, rotation, convective core overshooting and binary interaction have a strong impact on the evolution of massive stars. Quantitatively, our knowledge about these effects is still fairly limited.

1.1.1. Formation of massive stars

Stars are formed out of molecular clouds when the pressure equilibrium is perturbed and the cloud collapses under its own gravity. With increasing density, the cloud becomes opaque to infra-red photons and radiation is trapped. That leads to an increase in temperature and pressure in the core. Surrounding material is accreted until hydrostatic equilibrium (pressure gradient balancing the gravitational force) no longer exists and a dynamical collapse occurs.

In case of massive stars, the gas accretion process is difficult. The radiation pressure which massive stars exert on their surrounding gas and dust can be stronger than the gravitation. One solution to overcome this problem are accretion discs causing non-spherical accretion (Nakano 1989; Jijina & Adams 1996; Cesaroni et al. 2006). The evidence of discs for massive proto-stars is discussed in Cesaroni et al. (2007). Outflows from young massive proto-stars are found for example in Richer et al. (2000) implying

discs to be present. However, for very luminous objects like early O-type stars discs have not been found yet.

There are several ways how massive stars can be formed. A detailed review and discussion of the main concepts are given in Zinnecker & Yorke (2007). One theory of producing a massive star involves a monolithic collapse in an isolated core (Yorke & Sonnhalter 2002; McKee & Tan 2003; Krumholz et al. 2009). In this model, fragmentation (Krumholz & Bonnell 2007) and successive disc accretion leads to star formation. The mass of the star is determined by the core it is formed of. But, this process creates only a small number of massive stars (Bressert et al. 2012).

Another theory of forming massive stars is that of competitive accretion (Bonnell et al. 2001, 2004; Bonnell & Smith 2011; Smith et al. 2009). Only low mass stars are formed up by fragmentation processes in this scenario. Massive stars are produced due to accretion of the surrounding gas caused by the overall potential towards the cluster center (e.g. Bonnell et al. (2001, 2006)).

Stellar collisions and mergers is the third common concept of massive star formation (Quinlan & Shapiro 1990; Portegies Zwart et al. 1999; Figer & Kim 2002; Gürkan et al. 2004; Freitag et al. 2006).

1.1.2. Evolution of massive stars

1.1.2.1. Evolution on the main sequence

Stars on the main sequence are burning hydrogen in hydrostatic equilibrium. Additionally, stars are in thermal equilibrium, when the energy produced in the center balances the energy radiated away at the surface. A star in hydrostatic and thermal equilibrium is described by the following differential equations

$$\frac{\partial r}{\partial m} = \frac{1}{4\pi r^2 \rho}, \tag{1.1}$$

$$\frac{\partial P}{\partial m} = -\frac{Gm}{4\pi r^4}, \tag{1.2}$$

$$\frac{\partial l}{\partial m} = \epsilon_{\mathrm{nuc}} - \epsilon_{\nu}, \tag{1.3}$$

$$\frac{\partial T}{\partial m} = -\frac{Gm}{4\pi r^4}\frac{T}{P}\frac{\mathrm{d}\log T}{\mathrm{d}\log P}. \tag{1.4}$$

with the gravitational constant G and the energy generation ϵ_{nuc} and of neutrino energy loss ϵ_{ν}. The properties density ρ, pressure P, luminosity l, temperature T and radial distance r within a star are functions of mass coordinate m and time t.

The pressure P within a massive star is a mixture of ideal gas pressure and radiation pressure. For ideal gas of temperature T and mean molecular chemical potential μ , particle momenta follow the Maxwell-Boltzmann distribution (R is the universal gas constant) leading to the gas pressure given by

$$P = \frac{R}{\mu}\rho T. \tag{1.5}$$

The radiation pressure (k: Boltzmann constant, h: Planck constant, c: speed of light in vacuum) is described by

$$P = \frac{1}{3}\frac{8\pi^5 k^4}{15h^3c^3}T^4. \tag{1.6}$$

Massive stars are mostly dominated by ideal gas pressure. The more massive a star, the more important the radiation pressure becomes compared to the ideal gas pressure. For the very massive stars with mass $M \geq 100\,M_\odot$ the radiation pressure becomes dominant.

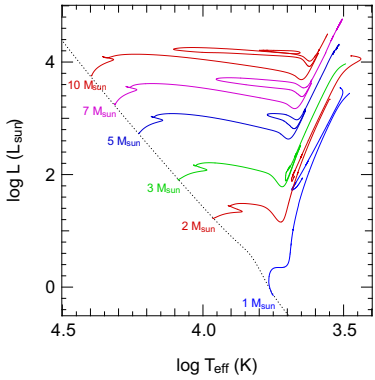

Figure 1.1.: Hertzsprung-Russel (HR) diagram showing the evolution of stars between $1\,M_\odot$ and $10\,M_\odot$ on the main sequence and beyond in luminosity L as a function of the effective temperature $T_{\rm eff}$ (Pols 2009). The black dotted line shows the zero-age main sequence (ZAMS).

Figure 1.1 shows the Hertzsprung-Russel (HR) diagram of stars. It gives the evolution of the luminosity L as a function of the effective temperature $T_{\rm eff}$. A star on the main sequence fuses hydrogen into helium in its core, changing the composition within continuously. As a result of the energy production by nuclear burning, the luminosity

and the core temperature increase with time. To keep up hydrostatic equilibrium, the layers around the core expand, leading to a decrease in effective temperature.

A section of a star with opacity κ is radiative if the following condition for the temperature gradient ∇ holds (a: radiation constant):

$$\nabla = \nabla_{\mathrm{rad}} = \left(\frac{\mathrm{d}\log T}{\mathrm{d}\log P}\right)_{\mathrm{rad}} = \frac{3}{16\pi acG}\frac{\kappa l P}{m T^4}. \tag{1.7}$$

In this case, the energy is transported by radiation within the star. The process is called radiative diffusion.

A section of a star is convective, if the Ledoux criterion given in Equation (1.8)

$$\nabla_{\mathrm{rad}} \leq \nabla_{\mathrm{ad}} - \left(\frac{\partial \log P}{\partial \log \mu}\right)_{\rho,T} \cdot \left(\frac{\partial \log T}{\partial \log P}\right)_{\rho,X_{\mathrm{i}}} \cdot \nabla_{\mu}, \tag{1.8}$$

is violated, with the adiabatic temperature gradient ∇_{ad}, the gradient of the mean molecular weight ∇_{μ} and the composition X_{i}. Assuming chemical homogeneous layers (∇_{μ} = 0), convection occurs when $\nabla_{\mathrm{rad}} \geq \nabla_{\mathrm{ad}}$. Material rises and expands adiabatically to restore pressure equilibrium, transporting energy efficiently along the way.

A massive star consist of a radiative envelope and a convective core. Small convective layers are located near the surface at temperatures where hydrogen and helium are partially ionized, leading to an increase in opacity. The time-scale of convective mixing is smaller than the thermal time-scale. This results in a fast, almost instantaneous, homogeneously mixed convective region. The mass of the convective core decreases with time as a consequence of $\nabla_{\mathrm{rad}} \propto \kappa \propto (1 + X)$, as the opacity κ decreases with decreasing hydrogen abundance X.

Convective overshooting due to the inertia of the transported material extends the convective region. The distance that is overshot is $d_{\mathrm{ov}} = \alpha_{\mathrm{ov}} \cdot H_{\mathrm{P}}$, with the overshooting parameter α_{ov}. d_{ov} is given in units of the pressure scale height H_{P} which is the radial distance over which the pressure changes by an e-folding factor.

1.1.2.2. Nucleosynthesis and post-main sequence evolution

Nuclear reactions within the stellar core, represented by the nuclei I, J, K and L,

$$I + J \longrightarrow K + L \tag{1.9}$$

depend on the number density and thermal velocity of the particles and the reaction rate $r_{\mathrm{ij,k}}$ of the reaction given in equation (1.9). The mass fraction X_{i} of element i, with mass number A and atomic mass unit m_{u}, varies as described by equation (1.10):

$$\frac{\partial X_\mathrm{i}}{\partial t} = \frac{A_\mathrm{i} m_\mathrm{u}}{\rho}\left(-\sum_{\mathrm{j,k}} r_{\mathrm{ij,k}} + \sum_{\mathrm{k,l}} r_{\mathrm{kl,j}}\right). \tag{1.10}$$

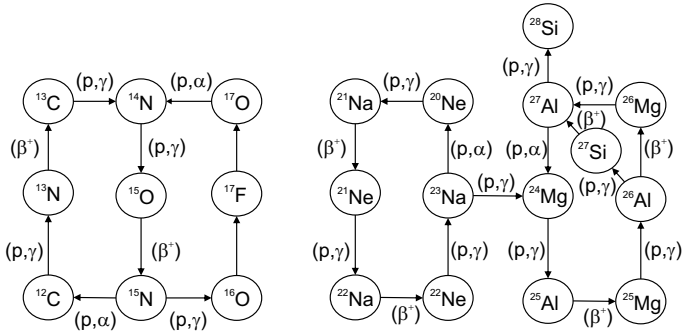

Figure 1.2.: The CNO cycle is shown in the left panel and the MgAl and NeNa cycles in the right panel.

Massive stars on the main sequence burn hydrogen in the core via the CNO cycle and the pp chain, with the CNO cycle being the dominant process. The CNO cycle is shown in the left panel of Figure 1.2. The CNO cycle starts at $14 \cdot 10^6$ K and becomes dominant for $T > 30 \cdot 10^6$ K. The overall reaction rate is determined by the slowest reaction $^{14}\mathrm{N}(p,\gamma)^{15}\mathrm{O}$. With time ^{14}N is enhanced, being the major product of the CNO cycle next to ^{4}He, while carbon, oxygen and fluorine are reduced.

Apart from the CNO cycle, the MgAl and NeNa cycle (shown on the right panel of Figure 1.2) occur within massive stars. The main product is sodium being produced within the NeNa chain. The light elements beryllium, boron and lithium are destroyed by proton capture at temperatures of 2.5–5·10^6 K (McWilliam & Rauch 2004). These elements can only exist in the outer layers of massive stars.

After hydrogen core burning, massive stars contract. With time, the shell surrounding the helium core becomes hot enough to ignite hydrogen. The star undergoes hydrogen shell burning. During this phase, the contraction continues, correlated to an expanding envelope. The short lifetime of stars in the hydrogen shell burning phase leads to a gap in the HR diagram called the Hertzsprung-gap.

With further increasing core temperature, helium is ignited stopping the core contraction. Stellar cores above 10^8 K undergo the triple-α reaction producing ^{12}C. After ^{12}C

is created in a sufficient amount, ^{16}O is produced. During helium core burning, most of the luminosity is created by hydrogen burning in the shell. Stars in the helium core burning phase show a loop in the HR diagram, which extends with increasing mass up to 12 $M_\odot$. After helium is ignited, massive stars are mostly convective and evolve along the Hayashi line with decreasing luminosity. When the envelope becomes radiative, the effective temperature increases and the star leaves the red giant branch (onset of the blue loop). Afterwards, the envelope of the star expands again with decreasing effective temperature leading it back to the red giant branch.

All stars with $M > 8\,M_\odot$ but $M < 11\,M_\odot$ ignite carbon off-center in a mild flash as the core becomes partially degenerate. After several of these flashes, the burning front moves toward the centre and leads to stable carbon burning in the core. A degenerate O-Ne-Mg core is produced, with no further nuclear burning occurring. All stars with $M > 11\,M_\odot$ undergo all burning stages and produce an iron core. It takes only about 10^3 yr from the onset of carbon burning at 5–8$\cdot 10^8$ K until the production of the iron core. These stars evolve through the following burning stages:

- neon burning (at 10^9 K), producing oxygen and magnesium due to alpha capture and photo-disintegration,
- oxygen burning (at $2 \cdot 10^9$ K), producing mostly ^{28}Si and ^{32}S and
- silicon burning (at $3 \cdot 10^9$ K), producing a final composition mostly consisting of ^{56}Fe and ^{52}Cr, by photo-disintegration and alpha capture reactions.

After iron is created in the core, no further thermonuclear energy can be produced by the core. It collapses and produces a cataclysmic event.

1.1.2.3. Evolution with mass loss by stellar winds

Mass loss by stellar winds plays a key role for the evolution of massive stars with an initial mass above 15 $M_\odot$. Many reviews in literature summarize and explain the physics of stellar winds for example Kudritzki & Puls (2000); Lamers & Cassinelli (1999); Puls et al. (2008b); Vink (2011); Puls et al. (2015).

Within a star, photons interact with matter multiple times by scattering, transferring their momentum in the process. This causes radiation pressure in absorption lines (Castor et al. 1975; Abbott 1982; Pauldrach et al. 1986; Vink et al. 2000, 2001), giving this kind of stellar wind the name "line-driven" or "radiation-driven" wind. The wind removes material from the surface of the star decreasing its total mass with time. Recent stellar wind models for massive stars are presented in Vink et al. (2011b); Pauldrach et al. (2012); Muijres et al. (2012).

The radiation pressure depends on the number of lines, the electron density and the optical thickness and the ionization of the stellar wind. As the radiation pressure in massive stars is raised by metals for the most part, mass loss is metallicity dependent. Observational evidence for the metallicity dependence has been found and discussed in Garmany & Conti (1985); Prinja (1987); Lamers et al. (1995).

When the effective temperature of a star reaches about 21 000 K, Fe IV recombines to Fe III (Vink et al. 2001). The terminal wind velocity reduces by a factor of two and the mass loss rate increases by a factor of 5 as the star evolves from $T_{\rm eff} > 21\,000$ K to $T_{\rm eff} < 21\,000$ K. This jump is called the bi-stability jump.

Stellar winds are expected to be non-stationary and inhomogeneous. Most of the gas in the wind is compressed into dense areas separated by large regions of low density. These small inhomogeneities are called clumps and make theoretical predictions of mass loss uncertain. For example, predictions of mass loss rates are revised downwards by about a factor of 10 when clumping is included (Puls et al. 2008a). A review and discussion of the consequences of clumping in stellar winds of hot massive stars is presented in Sundqvist et al. (2012).

Mass loss affects the evolution of a star in many aspects and enriches the interstellar medium. In Eggenberger et al. (2009) stellar evolution models from Maeder (1981) are compared with and without mass loss. It is shown, that the main sequence band is widened by mass loss as the core mass fraction increases with decreasing luminosity. For very massive stars the outer layers are removed by mass loss. The radius decreases leading to blue ward evolution in the HR diagram. Mass loss removes angular moment of rotating stars, changes the internal structure, lifetime and surface abundances. It determines the stellar mass before collapse and therefore the type of remnant left behind.

1.1.2.4. Evolution with rotational mixing

The physics of rotating stars is reviewed and summarized in Maeder & Meynet (2008b, 2011, 2012, 2015). Rotation affects the structure and evolution of massive stars depending on the metallicity, as it is studied for example in Meynet & Maeder (1997); Maeder (1998); Meynet & Maeder (2000); Maeder & Meynet (2001); Meynet & Maeder (2002); Brott et al. (2011a). The shape of a rotating stars is deformed. The pole of the oblate star is hotter than the equator. The transport of angular momentum is mainly caused by meridional currents (Maeder & Zahn 1998).

Differential rotation within a star causes instabilities, leading to chemical mixing. The main process causing rotational mixing in the stellar models, which are presented in Section 3, is the Eddington-Sweet Circulation (Heger et al. 2000). The effect of rotational mixing increases with stellar mass and initial rotation rate. The efficiency

of rotational mixing is higher at lower metallicity. Chemical mixing causes nitrogen enhancement at the surface of OB type stars (see e.g. Heap et al. (2006)).

Rotation does not only smooth out the chemical gradient in radiative zones, it also affects how stars evolve in the HR diagram. As the effective gravity is reduced, rotating stellar evolution tracks are shifted towards lower effective temperatures. Rotation causes hydrogen to be mixed into the convective core providing the star with fresh burning fuel. Therefore the stellar core decreases in mass slower than for the non-rotating case, leading to a higher luminosity compared to non-rotating stars (Langer 1992; Fliegner et al. 1996). Rapid rotation leads to stars being mixed homogeneously. Already in Maeder (1987), the difference in evolution of slowly and rapidly rotating stars in the HR diagram is presented. Above a critical rotational velocity of about 350 ± 50 km/s, a chemical gradient within the star is prevented to be build up due to very efficient mixing. These stars evolve bluewards in the HR diagram with increasing luminosity, referred to as chemically homogeneous evolution. They do not become red supergiants.

The main sequence lifetime increases with rotational velocity, as hydrogen is mixed into the core. Meynet & Maeder (2000) found an increase of about 30% of the main sequence lifetime for their solar metallicity models of 9 to 120 $M_{\odot}$.

Rotation affects the mass loss rate of massive stars (Meynet et al. 2006; Maeder & Meynet 2008a). The mass loss on the main sequence is enhanced with increasing rotation rate. A star of mass M rotates with critical velocity $v_{\rm crit}$, when the centrifugal force caused by rotation equals the gravitational force at the equator. This corresponds to the radius of the star at the equator $R_{\rm e,crit}$.

$$v_{\rm crit}^2 = \frac{GM}{R_{\rm e,crit}}. \tag{1.11}$$

When the stars reach critical rotation, a significant increase of the mass loss rate is the result. Material at the stellar surface is easily removed building up a disc in the equatorial plane (explained in detail in Bjorkman & Cassinelli (1993)).

1.1.2.5. The Eddington limit

The upper limit to the luminosity $L_{\rm edd}$ carried by radiation, for a star in hydrostatic equilibrium, is given by

$$L \leq L_{\rm edd} = \frac{4\pi c G M}{\kappa}, \tag{1.12}$$

depending on mass M and opacity κ.

This limit might be violated by intense nuclear burning or very high opacities causing convective transport of energy. With increasing initial mass the luminosity will exceed

the Eddington luminosity. Is the Eddington limit exceeded at the stellar surface, high mass loss should arise as the radiative acceleration is not balanced by the gravity anymore. Is the Eddington limit exceeded in the outer envelop of massive stars, as it has been found in Sanyal et al. (2015), the envelop of the star becomes inflated and the star might show pulsations.

In case a massive rotating star is near the Eddington limit, the rotation rate decreases the Eddington luminosity $L_{\rm edd}(\Omega)$ (Maeder & Meynet 2000a). The star reaches the $\Omega\Gamma$ – limit, when the luminosity equals the reduced Eddington luminosity $L_{\rm edd}(\Omega)$, leading to strongly increased mass loss. Maeder et al. (2005) suggests, that the HD limit is caused by the $\Omega\Gamma$ – limit.

1.1.2.6. Wolf-Rayet stars

Wolf-Rayet (WR) stars are very luminous hot stars with strong emission lines in their spectra. They have strong optically thick winds leading to mass loss of 10^{-5} to 10^{-4} $M_{\odot}$/yr. WR stars are often surrounded by circumstellar nebulae of the ejected material. They are classified based on the abundances at the surface.

- WNL: H present but < 40%, He increased, N consistent with CNO equilibrium abundance
- WNE: lack of H, He increased, N consistent with CNO equilibrium abundance
- WC: lack of H, He increased, C and O present, little to no N
- WO: lack of H, He increased, C present, increased O abundance, little to no N

Mass loss of Wolf Rayet stars is driven by radiation pressure (Eichler et al. 1995; Gräfener & Hamann 2008a) with photons being scattered multiple times or successive redistribution and absorption of thermalized photons. Heger & Langer (1996) investigated how optically thick winds affect the surface and core of WR stars. The inner structure is only slightly affected by strong wind, but Heger & Langer (1996) confirm large radii and small effective temperatures at the surface of WR stars.

The increased CNO abundance of WR stars indicate that they are exposed H- or He-burning cores of massive stars. Langer et al. (1994) suggested WN stars as core hydrogen burning objects and hot WN and WC stars as core helium burning stars. Their positions are shown in the HR diagram in Figure 1.3 (Gräfener & Hamann 2008b). Langer et al. (1994) indicated that very massive stars evolve into WR stars again, after they left a phase showing spectroscopic and photometric variability due to pulsational instabilities (Luminous blue variable phase; LBV) leading to the following evolutionary

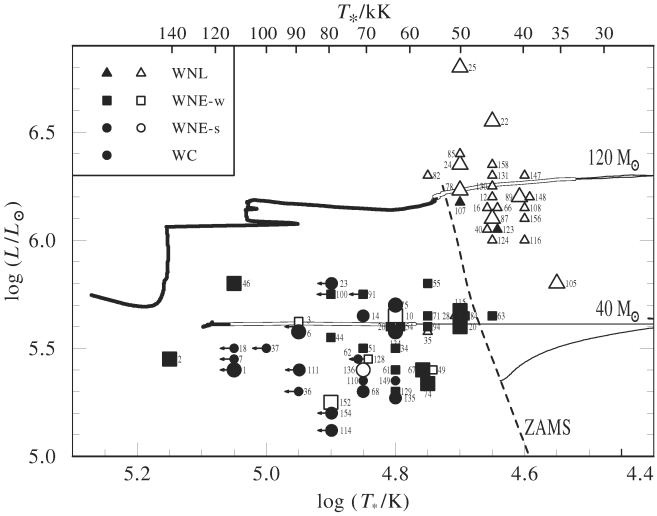

Figure 1.3.: Galactic Wolf-Rayet stars in the HR diagram (Figure from Gräfener & Hamann (2008b)). Light grey symbols correspond to WNL-stars, dark grey symbols correspond to WNE-stars and black symbols correspond to WC-stars. For objects shown by large symbols, estimates of the distance were available. Additionally, two evolutionary tracks of non-rotating models of 40 and 120 $M_\odot$ ((Meynet & Maeder 2003)) are shown as well as the zero-age main sequence (dotted line).

sequence of massive stars: O – Of – H-rich WN (core H burning) – LBV – H-poor WN (He core burning) – H-free WN – WC – SN.

1.1.3. Fate of massive stars

Stars with masses initially greater than 8 $M_\odot$, produce core-collapse supernovae (e.g. Smartt (2009)) and end their lives as neutron stars or black holes. A detailed review of the fate of massive single stars depending on their initial mass is given in Heger et al. (2003). In Yungelson et al. (2008) the evolution and fate of super-massive solar composition stars is studied.

Stars initially less massive than 20–25 $M_\odot$ typically produce neutron stars as they end their lives. For higher masses, stars can collapse to black holes when a large fraction of the core falls onto the neutron star. The resulting remnant mass is higher than the maximum mass for a neutron star. At approximately 35 $M_\odot$ the effect of mass loss during the evolution is so strong that the entire hydrogen envelope is lost before the explosion of the star occurs.

In case of metal-free stars (Population III stars), of more than 100 $M_\odot$ initially, electron-positron pair creation reduces the thermal pressure inside the star after central carbon burning (Bond et al. 1984; Woosley 1986), leading to oxygen and silicon being burned rapidly. Some of these stars will explode as pair instability supernova (PISN) (Belkus et al. 2007; Yungelson et al. 2008). For computations of Pop III stars, Umeda & Nomoto (2002) find PISNs with He-cores masses between 70 and 129 $M_\odot$. Similar results are found by Heger & Woosley (2002) with 63–133 $M_\odot$ for non-rotating He-stars. Between 140–260 $M_\odot$ the star is disrupted completely. For these stars, the energy of the first pulse is already high enough to entirely destroy the whole star leaving no remnant. Stars more massive than 260 $M_\odot$ undergo photo-disintegration of α-particles what reduces the pressure that far, that these stars directly turn into black holes (Woosley 1986; Fryer et al. 2001). A schematic summary of the fates of massive single stars depending on initial mass and metallicity is given in Heger et al. (2003).

1.2. Structure of this doctoral thesis

The effects of mass loss, rotation and metallicity on the evolution of massive and very massive stars are widely discussed in literature. In particular Heger et al. (2000), Brott et al. (2011a), Ekström et al. (2012) and Yusof et al. (2013) present detailed models of rotating massive stars in the Galaxy and the Magellanic Clouds.

Although numerous studies exist for the very massive stars with LMC metallicity, new stellar models are presented in Section 3 of this thesis with initial surface rotational velocities up to 550 km/s in steps of 50 km/s. One goal of this thesis is to study the influence of rotation on the main sequence evolution of the very massive stars and to simulate populations of O-type stars with LMC metallicity (later referred to as population synthesis) based on these models.

Population synthesis is important for statistical comparison and analysing observational data of star clusters. A review of population synthesis codes can be found in Leitherer & Ekstrom (2011), with discussions about the importance of multiplicity, stochasticity, rotation and stellar evolution on the outcome of the calculations. Several population synthesis codes can be found in Arnault et al. (1989); Maeder (1991); Cerviño & Mas-Hesse (1994); Meynet (1995); Brott et al. (2011a).

1.2.1. Nitrogen chronology of massive main sequence stars

Burning hydrogen into helium via the CNO cycle increases nitrogen in the core until the equilibrium abundance is reached. When adding rotation to the process, nitrogen is transported throughout the star by rotational mixing. Therefore the surface nitrogen abundance increases monotonically during the main sequence. In Section 2, this effect is used to obtain constraints on the age or inclination angle of rotating stars.

The method to calculate the surface nitrogen abundance of massive stars presented in Section 2 is based on stellar evolution models published in Brott et al. (2011a) for LMC, SMC and Galactic (MW) composition. Depending on mass and rotation rate at the zero-age main sequence (ZAMS), equations are presented for calculating the surface nitrogen abundance using an incomplete gamma–function. The population synthesis code Starmaker (Brott et al. 2011b) is used to predict the location of stars in the Hunter diagram (nitrogen abundance - projected surface rotational velocity) for which constraints on the age can be derived. 79 early B-type main sequence stars from the VLT FLAMES I survey (Evans et al. 2005, 2006) in the LMC clusters NGC 2004 and N 11 and the SMC clusters NGC 330 and NGC 346 are analyzed.

For 17 stars, age constraints are found and compared to ages derived from isochrones of non-rotating stellar models. 7 stars are consistent with the expected behaviour, while 10 stars are inconsistent, confirming the suspected unusual evolution of the fast rotators showing only low surface nitrogen abundances as discussed in Hunter et al. (2008a); Brott et al. (2011b). In case of 62 stars, constraints on their inclination angle are derived. The distribution of inclination angles in the SMC tells that the upper limits given for

the surface nitrogen abundances are on average significantly above the actual nitrogen abundances.

1.2.2. Stellar evolution models of massive rotating star

A study of the effect of mass loss and rotational mixing on the evolution of very massive rotating stars on the main sequence is given in Section 3. The focus lies on the main sequence evolution of very massive rotating models when they approach the Eddington limit and whether rotational mixing smooths out the chemical gradient within the star leading to chemically homogeneous evolution.

Detailed stellar evolution models are presented for LMC metallicity with initial masses between 70 and 500 $M_{\odot}$ and surface rotational velocities up to 550 km/s at the zero-age main sequence. The calculations are performed with a one-dimensional hydrodynamic binary stellar evolution code (BEC) which takes into account rotation, mass loss and transport of angular momentum by magnetic fields. A grid of stellar evolution models with a dense spacing in mass and rotation rate at the ZAMS is produced which is used for a high resolution population synthesis in Section 4.

The stellar evolution models are strongly affected by rotational mixing and mass loss. This can be seen in the HR diagram and by the increase of helium and nitrogen with time. The most rapidly rotating models evolve quasi-chemically homogeneous due to mass loss and rotational mixing. Additionally, a region at low effective temperatures in the HR diagram can be found were no stars are predicted. This region is similar to but not agreeing with the Humphreys-Davidson limit.

1.2.3. Populations of massive rotating stars in the LMC

In Section 4, a study of different population synthesis simulations is provided using the stellar evolution models of very massive rotating stars presented in Section 3 and massive stars from Brott et al. (2011a).

The presented stellar populations are simulated assuming a random orientation of the rotation axis of stars in space, and the Salpeter (1955) initial mass function. The initial surface rotational velocity distributions derived from the VFTS data (see Ramírez-Agudelo et al. (2013)) is used for stars of spectral type O7–O2. To study the effect of star formation history on the simulation outcome, five different age distributions are chosen: continuous star formation and starbursts represented by a delta function (one, two, three and five Myr).

The data of each star received from the simulation contains effective temperature, luminosity, radius, surface gravity, mass loss rate, surface rotational velocity, mass, sur-

face abundances of helium, boron, carbon, nitrogen, oxygen, neon, sodium and silicon, age and inclination angle. Additionally the following parameters are provided at the zero-age main sequence: mass and rotation rate. For the simulated populations, the HR diagram and the helium mass fractions at the surface as functions of the projected surface rotational velocity are shown, including the distribution of the simulated stars within these diagrams, given by the number of stars in a defined interval (later referred to as density plot). Additionally, histograms of surface rotational velocity and mass, comparing initial and current distributions, are provided.

The simulations confirm that the significantly different evolution of rapidly rotating stars compared to slow rotating stars, as seen in the underlying stellar models, is expected to be visible in the simulated populations of stars. In case of starbursts (age distribution: delta function), approximately 10% of the populations show signs of chemically homogeneous evolution, while it is only about 1% in case of continuous star formation. However, some special features only relate to the evolution of the very massive stars, as for example an area of slightly increased probability in the HR diagram due to Wolf-Rayet mass loss. They are conspicuous but, with only 1% of the stars in the population showing this effect, a very large sample of observed stars (including very massive stars), like the VLT-FLAMES Tarantula Survey (see Section 1.3), will be necessary for comparison.

The observational data of O-type stars in 30 Dor is used for a first qualitative analysis of the presented stellar populations.

1.3. The VLT-FLAMES Tarantula Survey (VFTS)

The VLT-FLAMES Tarantula survey (VFTS) is an ESO Large Programme during which multi-epoch spectroscopy of about 1000 OB-type stars in the Tarantula nebula is obtained (Evans et al. 2010; Taylor et al. 2011). The Tarantula nebula (30 Doradus, NGC 2070), located within the Large Magellanic Cloud (LMC), has been proven to be an ideal choice to study very massive stars. The dense cluster R136 in the core of 30 Dor contains the most massive stars known up to date (Crowther et al. 2010).

A detailed description of the target selection, as well as the spectroscopy and photometry performed can be found in Evans et al. (2011). The majority of targets within and near the Tarantula nebula are marked in Figure 1.4.

To assure a significant signal-to-noise ratio, a magnitude cut-off at $V = 17\,\mathrm{mag}$, and to avoid selection biases, no colour cut are applied. In total, the sample contains 300 O-type stars, 500 B-type stars, 20 Wolf-Rayet or 'slash' Of/WN emission-line stars, 90 stars with spectral class A–F and more than 100 foreground stars (Evans et al. 2010;

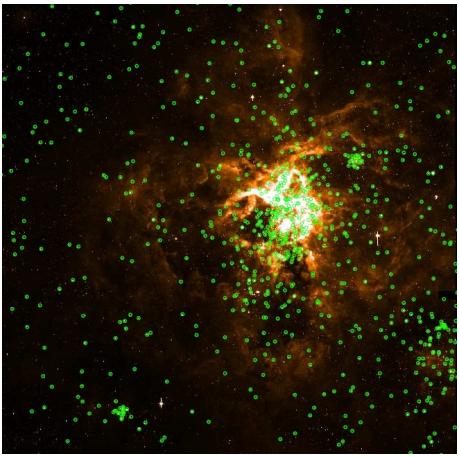

Figure 1.4.: The majority of targets observed in the VLT-FLAMES Tarantula survey are marked within a 14' x 14' V-band WFI image of the Tarantula nebula (Evans et al. 2010).

Taylor et al. 2011; Markova et al. 2011; Lennon et al. 2011). 30 Dor is an excellent environment to study the formation and evolution of massive and very massive stars as it is the largest survey until now.

Many very massive stars exist in 30 Dor with initial masses expected to be up to 300 $M_{\odot}$ (Crowther et al. 2010), what can be deduced from their luminosity. The basis to analyse these stars are stellar evolution models of very massive stars. Stellar evolution models up to 300 $M_{\odot}$ initially assuming LMC composition that are published until now (e.g. Crowther et al. (2010); Brott et al. (2011a); Yusof et al. (2013)) are insufficient for comparison to the VFTS. Either the mass range does not cover very massive stars, or the stellar models are only calculated for two different surface rotational velocities to differentiate between non-rotating and rotating stars.

Providing a suitable grid of stellar evolution models to analyse the stars observed with the VLT-FLAMES Tarantula survey was the major motivation to calculate the stellar evolution models presented in Section 3. These stellar evolution models are the only models published until now that are suited to analyse the data obtained by the VLT-FLAMES Tarantula survey.

2. Nitrogen chronology of massive main sequence stars

Published in Astronomy& Astrophysics, Volume 544, id.A76, 15 pp on 31 July 2012.
Authors: K. Köhler[1], M. Borzyszkowski[1], I. Brott[2], N. Langer[1] and A. de Koter[3,4]

[1] Argelander-Institut für Astronomie der Universität Bonn,
Auf dem Hügel 71, 53121 Bonn, Germany
[2] University of Vienna, Department of Astronomy,
Türkenschanzstr.17, 1180 Vienna, Austria
[3] Astronomical Institute, Utrecht University,
Princetonplein 5, 3584CC, Utrecht, The Netherlands
[4] Astronomical Institute Anton Pannekoek, University of Amsterdam,
Kruislaan 403, 1098 SJ, Amsterdam, The Netherlands

ABSTRACT:

Context: Rotational mixing in massive main sequence stars is predicted to monotonically increase their surface nitrogen abundance with time.

Aims: We use this effect to design a method for constraining the age and the inclination angle of massive main sequence stars, given their observed luminosity, effective temperature, projected rotational velocity and surface nitrogen abundance.

Methods: This method relies on stellar evolution models for different metallicities, masses and rotation rates. We use the population synthesis code STARMAKER to show the range of applicability of our method.

Results: We apply this method to 79 early B-type main sequence stars near the LMC clusters NGC 2004 and N 11 and the SMC clusters NGC 330 and NGC 346. From all stars within the sample, 17 were found to be suitable for an age analysis. For ten of them, which are rapidly rotating stars without a strong nitrogen enhancement, it has been previously concluded that they did not evolve as rotationally mixed single stars. This is confirmed by our analysis, which flags the age of these objects as highly discrepant

with their isochrone ages. For the other seven stars, their nitrogen and isochrone ages are found to agree within error bars, what validates our method. Constraints on the inclination angle have been derived for the other 62 stars,with the implication that the nitrogen abundances of the SMC stars, for which mostly only upper limits are known, fall on average significantly below those limits.

Conclusions: Nitrogen chronology is found to be a new useful tool for testing stellar evolution and to constrain fundamental properties of massive main sequence stars. A web version of this tool is provided.

Keywords: stars: massive – stars: evolution – stars: rotation – stars: abundances – stars: early type

2.1. Introduction

The age determination of stars is an important objective, and several methods are currently being used. For star clusters, which presumably contain stars of similar ages, comparing the main sequence turn-off point in a color-magnitude or Hertzsprung-Russell diagram with stellar evolution models can predict the age of all stars in the cluster (Jia 2002; Buonanno 1986). For individual stars, ages can be derived by comparing their location in the HR-diagram with isochrones computed from stellar evolution models. In the envelope of low mass main sequence stars lithium is depleted, resulting in a monotonous decrease of the surface lithium abundance with time, which can be used to determine their age (Soderblom 2010; Randich 2009).

Massive stars fuse hydrogen to helium via the CNO cycle. The reaction ^{14}N (p,γ)^{15} O has the lowest cross section, resulting in an increase of the nitrogen abundance compared to carbon. The evolution of massive stars is furthermore thought to be affected by rotation, which may cause mixing processes including large scale circulations and local hydrodynamic instabilities (Endal & Sofia 1978). The nitrogen produced in the core can be transported to the surface when rotational mixing is considered, causing a monotonic increase of the surface nitrogen abundance with time (Heger et al. 2000; Maeder 2000; Przybilla et al. 2010). Here, we suggest to utilize this effect to constrain the ages of stars.

Based on detailed stellar evolution models, we present a method which reproduces the surface nitrogen abundances of massive main sequence stars as a function of their age, mass, surface rotational velocity and metallicity. Three stellar evolution grids for the Milky Way (MW), the Large Magellanic Cloud (LMC) and the Small Magellanic Cloud (SMC) are used, providing stellar models of different metallicities, masses and

rotational velocities and include the effects of rotational mixing (Brott et al. 2011a). The mixing processes in these stellar evolution models were calibrated to reproduce the massive main sequence stars observed within the VLT-FLAMES Survey of Massive Stars (Evans et al. 2005, 2006).

The abundance analysis of massive stars is often focused on stars with small $v \sin i$ values, as this allows to obtain abundances with higher accuracies (Przybilla et al. 2010). However, those objects are not well suited for nitrogen chronology, as they are either slow rotators, or have a low inclination angle. In the latter case, the age can not be well constrained, since a large range of true rotational velocities is possible. Many stars analyzed in the VLT-FLAMES Survey, however, are particularly suited as targets for nitrogen chronology, since this survey did not concentrate on the apparent slow rotators.

On the other hand, results from the VLT-FLAMES Survey identified two groups of early B-type stars which could not be reconciled by the evolutionary models of single stars with rotational mixing (Hunter et al. 2008a; Brott et al. 2011b). The first group consists of slowly rotating stars which are nitrogen rich, to which the method of nitrogen chronology is not applicable. The second group contains relatively fast rotating stars with only a modest surface nitrogen enhancement. While such stars are in principle predicted by models of rotating stars (Brott et al. 2011a), they were not expected in be found in the VLT-FLAMES Survey due to the imposed V-band magnitude cut-off, since unevolved main sequence stars are visually faint, and the visually brighter more evolved rapid rotators are expected to be strongly nitrogen enriched (Brott et al. 2011b). Brott et al. (2011b) suggested that either these stars are the product of close binary evolution, or that rotational mixing is much less efficient than predicted by the stellar evolution models.

The nitrogen chronology is able to shed new light on this issue. In contrast to the population synthesis pursued by (Brott et al. 2011b), it does not use statistical arguments but is applied to each star individually. Its results can therefore be easily compared with classical age analyses, e.g., using isochrone fitting in the HR diagram. In this paper, we apply the nitrogen chronology to all LMC and SMC stars from the VLT-FLAMES Survey which have a projected rotational velocity larger than 100 km/s.

We organize our paper as follows. In Sect. 2.2 our method of nitrogen chronology is presented. Sect. 2.3 describes our analysis of the VLT-FLAMES sample. A discussion and evaluation of our new method is given in Sect. 2.4 and 2.5. Sect. 2.6 will round off with our conclusions.

2.2. Method

The enrichment of nitrogen at the surface of a massive star during its evolution on the main sequence depends on its mass and rotation rate. In Fig. 2.1 the surface nitrogen abundance is plotted against the fractional main sequence lifetime $\tau = t/\tau_{\mathrm{H}}$ for different initial masses and surface rotational velocities. Here, τ_{H} is the hydrogen burning lifetime of a stellar evolution sequence. A parameterization of τ_{H} as a function of mass and surface rotational velocity, for all three metallicities considered here, is given in Appendix A.1.2. For our method, we define "zero-age" as the time when the mass fraction of hydrogen has decreased by 2% in the center due to hydrogen core burning. This ensures that the stellar models are still unevolved but already thermally relaxed. The surface nitrogen abundance $\mathcal{N}$ is given by

$$\mathcal{N} = \log\left(\frac{N}{H}\right) + 12, \tag{2.1}$$

with the surface number density of nitrogen and hydrogen atoms N and H, respectively.

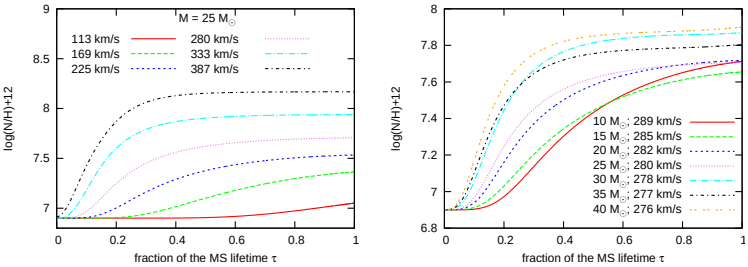

Figure 2.1.: For different models of the stellar evolution grid of Brott et al. (2011a) using LMC metallicity, the surface nitrogen abundance is plotted against the fractional main sequence lifetime. The left panel shows the influence of the initial rotational velocity v_{ZAMS} for a given mass of $M = 25\,M_{\odot}$. The right panel depicts the evolution of the surface nitrogen abundance for several masses at $v_{\mathrm{ZAMS}} \approx 280$ km/s.

Figure 2.1 shows that the nitrogen abundance rises smoothly over time starting with the surface nitrogen abundance at the ZAMS depending on the metallicity. It reaches its maximum value at the end of the main sequence evolution. The right panel of Fig. 2.1 depicts the mass dependence of the nitrogen enrichment at the surface. For a given initial surface rotational velocity, the models show a faster enrichment at the surface for higher initial mass. Furthermore, the faster the initial surface rotational velocity for a

given mass the greater is the effect of rotational mixing which leads to faster enrichment and a higher saturation value (Heger et al. 2000; Meynet & Maeder 2000; Maeder & Meynet 2001).

To constrain the age of an observed massive main sequence star using its surface nitrogen abundance, we derived an equation which fits the surface nitrogen abundance for a given mass, surface rotational velocity and metallicity to the models of rotationally mixed massive stars. In order to reduce interpolation errors in constructing this equation, stellar evolution grids are required which have a dense spacing in the grid parameters initial mass M and initial equatorial rotational velocity v_{ZAMS}. Presently, stellar evolution grids available for this purpose are those presented in Brott et al. (2011a).

The surface nitrogen abundance monotonically increases over the fraction of the main sequence lifetime (cf. Fig. 2.1). This can be reproduced well with an ansatz as

$$\mathcal{N} = a + c \cdot \gamma_d \left(b \cdot \tau\right). \tag{2.2}$$

The parameters a, b, c, and d are functions of the initial surface rotational velocity v_{ZAMS} and the initial mass M of a star. The incomplete gamma function $\gamma_d \left(b \cdot \tau\right)$ depends on the product $b \cdot \tau$, with the fraction of the main sequence lifetime τ and the parameters b and d. For calculating the surface nitrogen abundance according to Eq. (2.2) the incomplete gamma function is normalized by the complete gamma function Γ as

$$\gamma_d \left(b \cdot \tau\right) = \frac{1}{\Gamma\left(d\right)} \int_0^{b \cdot \tau} x^{d-1} e^{-x} \, \mathrm{d}x. \tag{2.3}$$

Considering the properties of the incomplete gamma function it is possible to make some statements about the parameters a, b, c, and d. The values of γ_d range from 0 to 1, so c is responsible for the height of the curve. The parameter a describes the initial surface nitrogen abundance, which is independent of mass and surface rotational velocity. The parameter b describes the speed of the nitrogen enrichment i.e. the steepness of the curves in Fig. 2.1.

The parameters b and c depend on initial mass and rotational velocity. By fitting Eq. (2.2) to the data of the stellar evolution models, both parameters can be determined for different values of M and v_{ZAMS}. Considering the parameter d, the best fits of Eq. (2.2) to the data of the three stellar evolution grids are obtained by a linear dependence of d on the surface rotational velocity v_{ZAMS} (see Appendix A.1.1).

Nitrogen profiles calculated by using Eq. (2.2) can be useful for binary population studies, where a quick knowledge of the surface nitrogen abundance is required.

2.2.1. Accuracy

Two stellar models are chosen to indicate the quality of the presented method to calculate the surface nitrogen abundance. All parameters of Eq. (2.2) are calculated from Eq. (A.1 - A.4) given in Appendix A.1.1 (Table 2.1). Using these values, the surface nitrogen abundance of the two sequences as a function of τ is calculated and shown as blue solid lines in Fig. 3.20. It is compared to the nitrogen abundance evolution which results from the detailed stellar evolution models of Brott et al. (2011a).

Table 2.1.: Parameters of the example sequence discussed in the text and displayed in Fig. 3.20.

parameter	model 2	model 1
M [$M_\odot$]	30	35
$v_{\rm ZAMS}$ [km/s]	169	168
Z	$Z_{\rm LMC}$	$Z_{\rm LMC}$
a	6.9	6.9
b	12.8	14.6
c	0.6	0.6
d	6.0	6.0

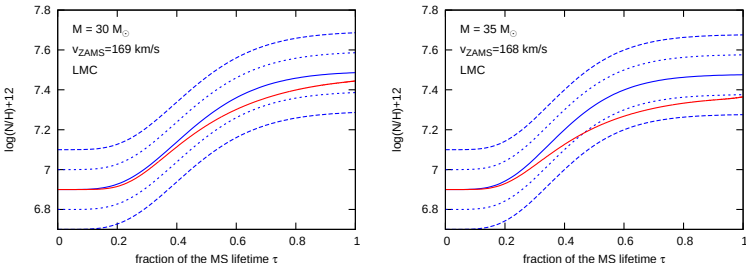

Figure 2.2.: Surface nitrogen abundance as function of the fractional main sequence lifetime for two specified stellar models (see legend) from the detailed stellar evolution grids of Brott et al. (2011a) (red lines), compared to the results of our fit (blue solid lines). The blue dashed lines represent error ranges of ±0.1 and ±0.2 dex for the nitrogen abundance. While the left panel shows a typical fit, the right panel depicts our worst case.

All calculated surface nitrogen abundance functions fit the detailed models very well for low values of τ, but show different levels of deviations towards the end of the main sequence evolution. In Fig. 3.20, a typical fit is shown on the left panel. At all times, the fit result deviates by less than 0.1 dex from the detailed model prediction. The right

panel of Fig. 3.20 shows our worst case. Even in this case, the fitted surface nitrogen abundance deviates by more than about 0.1 dex from the value of the detailed stellar evolution model for a fraction of the time.

Numerical noise in the detailed stellar evolution models does in rare cases lead to a non-monotonic behaviour of the nitrogen evolution as function of the initial rotation rate or as function of mass (cf., left panel of Fig. 1). These features are smoothed out by our analytic fitting method, which guarantees monotonic behaviour in the considered parameter space (Sect. 2.2). Therefore, a deviation of our nitrogen prediction from that of the detailed stellar evolution models does not necessarily flag a problem of our method. In summary, we consider the error in the predicted nitrogen abundance introduced by our fitting method to be smaller than 0.1 dex. In the present paper, the surface nitrogen abundances of the analyzed stars have an observational error of ±0.2 dex (Hunter et al. 2007).

2.2.2. Validity range

As the lowest mass of the underlying stellar evolution models used in our fitting method is 5 $M_\odot$, this defines the lower mass limit for its applicability. Towards very high masses, effects of stellar wind mass loss produce features which are not captured by our method above an upper limiting mass, which depends on metallicity (see Table 2.2).

The stellar evolution models of Brott et al. (2011a) for very rapidly rotating stars may undergo so called quasi-chemically homogeneous evolution. The behaviour of those models is also not captured by our fitting method. This problem is avoided when only initial rotational velocities below 350 km/s are considered, which thus defines the upper velocity limit for our method. This also ensures that 2D effects of very rapid rotation on the stellar atmosphere do not play a role here.

Table 2.2.: Range of initial stellar parameters for which our method is validated, for the three considered metallicities. In addition, for stars more massive than 30 $M_\odot$, the effective temperature should be higher than 25 000 K.

Galaxy	M $M_\odot$	$v_{\rm ZAMS}$ km/s
MW	5–35	0–350
LMC	5–45	0–350
SMC	5–50	0–350

As outlined in Sect. A.1.2, in applying our method we assume that the stellar surface rotation velocity remains roughly constant during the main sequence evolution. This is the prediction of the underlying stellar evolution models (Brott et al. 2011a) for stars

with initial masses below 30 $M_{\odot}$. For more massive stars, this feature still holds as long as the stellar effective temperature is larger than 25 000 K. For cooler temperatures, mass loss leads to a noticeable spin down of the stars. Our method is therefore valid in the ranges given in Table 2.2, with a restriction that for stars more massive than 30 $M_{\odot}$, their effective temperature should be higher than 25 000 K.

2.3. Application

2.3.1. Stellar sample

The obtained equations to calculate the surface nitrogen abundance for given initial mass and surface rotational velocity are applied here to constrain the properties of observed stars under the hypothesis that the underlying stellar models describe their evolution correctly. The VLT-FLAMES Survey of Massive Stars (Evans et al. 2005, 2006) has been chosen to provide the observational data.

The VLT-FLAMES Survey is a spectroscopic survey of hot massive stars performed at the *Very Large Telescope* of the European Southern Observatory. Over 700 O and early B type stars in the Galaxy and the Magellanic Clouds were observed. In Hunter et al. (2008b) (Magellanic Clouds) and Dufton et al. (2006) (Galaxy) the spectral data has been evaluated using the non-LTE TLUSTY model atmosphere code (Hubeny & Lanz 1995) to gain atmospheric parameters and projected rotational velocities of the observed stars. The surface nitrogen abundances were derived using the nitrogen absorption lines (Hunter et al. 2009). The evolutionary masses of the stars were determined in Hunter et al. (2008b) using the stellar evolution models of Meynet et al. (1994) and Schaerer et al. (1993) for LMC objects and in Meynet et al. (1994) and Charbonnel et al. (1993) for SMC objects. The derived evolutionary masses are in good agreement with evolutionary masses determined from the stellar evolution models used here.

For our analysis, we selected stars from the FLAMES LMC and SMC samples by several conditions. It is necessary to know the surface nitrogen abundance, the evolutionary mass and the (projected) surface rotational velocity of a star to use our method. We disregarded all sample stars for which this is not the case, or for which one of the parameters falls outside the validity range of our method (Sect. 2.2.2). We further discarded all stars with a projected surface rotational velocity below 100 km/s, as most of them are expected to be intrinsically slow rotators for which no significant age constraints from our method could be expected. In this way, 44 LMC and 35 SMC stars remain on the list, which we call “our” sample in the following (Tables A.2 and A.2).

While we need to exclude stars with rotational velocities above 350 km/s, it is possible that stars which rotate faster than this are present in our sample, since we only know the projected rotational velocities of our sample stars. The largest $v \sin(i)$ of all stars in our sample is 323 km/s. A priori, given the distribution of rotational velocities presented in (Brott et al. 2011b) (see Table B.1) of stars in the FLAMES LMC and SMC samples as well as a uniform distribution of orientations, 4.8% of all stars with $v \sin(i) < 350$ km/s have surface rotational velocities $v_{\rm rot}$ higher than 350 km/s. Such fast rotating stars rapidly enrich nitrogen at the surface. Within the first 10% of their main sequence lifetime, their surface nitrogen abundance increases above $\mathcal{N} = 8$ dex, in the LMC. For a rough estimate, assume that approximately 4.8% of all stars with $v \sin(i) < 350$ km/s could have a surface rotational velocity above 350 km/s with 10% of their main sequence lifetime corresponding to a surface nitrogen abundances $\mathcal{N} \leq 8$ dex. As we have no stars with $\mathcal{N} > 8$ dex in our sample, 0.48% of all stars within our sample could have a surface rotational velocity above 350 km/s, which we consider negligible.

The largest $v \sin(i)$ of our stars corresponds to about 50% of break-up velocity. Consequently, the largest centrifugal acceleration in the line of sight amounts to one quarter of the gravitational acceleration. In other words, the measured $\log g$ will be decreased by at most about 0.12 dex, and on average by less than half that value. This is smaller than the intrinsic measurement error of $\log g$ of about ± 0.15 dex. It is also small compared to the range of gravities of the sample stars, which is $4.4\,\text{dex} \leq \log g \leq 3.2$ dex. For this reason, we can neglect the correction of the gravity due to rotation.

2.3.2. Defining Class 1 stars

To constrain the age of an observed star through our method, its evolutionary mass, projected surface rotational velocity, metallicity and the surface nitrogen abundance need to be known. We want to mention, that in the case of differences between evolutionary and spectroscopic masses (Mokiem et al. 2006), this method will lead to different results when using the spectroscopic mass for deriving the nitrogen profile. The effect of changes in mass during the main sequence evolution, for stars within the validity range given in Table 2.2, on the calculated surface nitrogen abundance profile is smaller than the typical observational error of ± 0.2 dex. The mass, derived from the observational data is therefore used as the input value for M in Eq. (2.2).

If the true rotational velocity of the star is known (which is rarely the case, and not so for any of our sample stars), it can be used as input into Eq. (2.2), assuming that it still represents its initial rotational velocity. For a given metallicity the surface nitrogen abundance as a function of time is then calculated using the equations in Ap-

pendix A.1.1. Next, the fractional main sequence lifetime is determined by the condition that the calculated surface nitrogen abundance matches the observed one. By considering the main sequence lifetime of stars as function of mass and surface rotational velocity (cf. Appendix A.1.2), the age of the star is obtained.

If the true rotational velocity of a star is not known, but only its projected value $v \sin(i)$, we can compute the nitrogen surface abundance as function of τ for a model with the appropriate mass and metallicity, and with a rotational velocity equal to the projected rotational velocity of our target star. Since the projected rotational velocity is smaller than the true velocity, the nitrogen enrichment will be slower than in a model rotating with the true rotational velocity. We therefore obtain lower limits to the expected nitrogen abundance, for all times. The result of the analysis depends now on the measured nitrogen abundance of our star. If it is lower than the largest computed lower limit (which is obtained for $\tau = 1$), we can constrain the upper limit to the current age of the star.

We define stars of *Class 1* by the condition that their *observed surface nitrogen abundance, or its observationally determined upper limit, is lower than the maximum (final) calculated surface nitrogen abundance according to Eq. (2.2), when adopting the observed* $v \sin(i)$ *as rotational velocity in Eq. (2.2).*

Figure 2.3 illustrates our method at the example of the star N 11-95 from our LMC sample, with $M = 15\,M_{\odot}$, $v \sin(i) = 267$ km/s and $\mathcal{N} = 7.46$ dex. The observed abundance of nitrogen at the surface equals the calculated nitrogen abundance (which is a function of τ) at a value of $\tau = 0.43$. Considering a main sequence lifetime of 11.4 Myr, this leads to an upper age limit of 4.9 Myr for this star.

For some of the sample stars we only know upper limits to the surface nitrogen abundance. Since the nitrogen upper limit is larger than the true nitrogen abundance of the sample star, using the upper limit to the nitrogen abundance leads to an upper age limit of the observed star in the same way as for stars with determined nitrogen abundances.

2.3.3. Population synthesis of Class 1 stars

It is interesting to consider the location of Class 1 stars in the so called Hunter-diagram, where the surface nitrogen abundance of stars is plotted versus their projected rotational velocity. Since according to the stellar evolution models fast rotators are achieving higher surface nitrogen abundances, stars are likely to fall into Class 1 when they have a large $v \sin(i)$ (which makes their maximum nitrogen abundance large) as long as their measured nitrogen abundance is not too high. Conversely, nitrogen rich apparent slow rotators will not fall into Class 1.

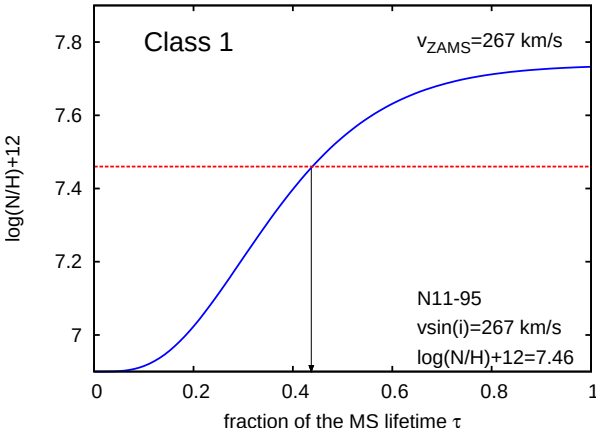

Figure 2.3.: The analysis of the Class 1 stars N 11-95 (LMC), which has an observed $v \sin(i)$ of 267 km/s. The blue solid line shows the calculated surface nitrogen abundance as function of the fractional main sequence life time τ of an LMC star with the mass of N 11-95 and assuming a rotational velocity of 267 km/s. The red dotted line indicates the measured surface nitrogen abundance of N 11-95. The black vertical arrow gives the derived upper limit on τ, i.e. $\tau < 0.43$.

To study this, we perform a population synthesis simulation for rotating single massive main sequence stars of LMC metallicity using the code STARMAKER (Brott et al. 2011b), with parameters as summarized in Table B.1.

To verify the Class 1 character of a simulated star with a given age, its mass and $v \sin(i)$ value have been used to compute its surface nitrogen abundance at the end of its main sequence evolution according to Eq. (2.2). If this value is higher than its actual surface nitrogen abundance, it is taken to be of Class 1. As all stars in the LMC and SMC sample have masses below 30 $M_\odot$ the maximum mass considered in this simulation was chosen as 30 $M_\odot$. Only stars with $v \sin(i) > 100$ km/s are evaluated.

Figure 2.4 shows the number density of simulated Class 1 stars in the Hunter-diagram. Stars are counted within intervals of $\Delta v \sin(i) = 10$ km/s and $\Delta \mathcal{N} = 0.05$ dex. The number of models in the intervals are indicated by the color coding.

Figure 2.4 illustrates for which stars the nitrogen chronology method can be used to derive an upper age limit. As expected, preferentially stars in the lower right corner of the Hunter-diagram can be evaluated as Class 1. For stars in the upper left corner of the Hunter-diagram we will be able to constrain their inclination angles (see below).

Table 2.3.: Parameters used in our population synthesis calculation (cf. Fig. 2.4).

parameter	
star formation rate	constant
considered time interval	35 Myr
velocity distribution	Gaussian distribution (Brott et al. 2011b) (σ = 141 km/s, μ=100 km/s)
velocity range	0 – 570 km/s
mass distribution	Salpeter (1955) IMF
mass range	5 – 30 $M_\odot$
stellar model grid	LMC (Brott et al. 2011a)

Finally, we note that if the inclination angle of a star is observationally determined (e.g. through a pulsation analysis, or a binary membership), its nitrogen age can be determined regardless of its location in the Hunter-diagram.

The majority of Class 1 stars in our sample are located in the LMC, only one star belongs to the SMC sample (see Appendix B.2). The reason is that nitrogen abundances of SMC stars are lower than those of comparable LMC (or Galactic) stars (Hunter et al. 2009), such that their abundance can not be determined if it is below a certain threshold which increases with the projected rotation velocity. That means, Box 1 in the Hunter-diagram of the SMC early B star sample is essentially empty (See Fig. 7 in Hunter et al. (2009)).

Furthermore, a comparison of Fig. 2.4 with Fig. 9 of Brott et al. (2011b) shows that only very few stars from the considered sample are expected in Box 1, due to the visual magnitude cut-off imposed in the sample selection. For this reason, Brott et al. (2011b) concluded that those stars of this sample which do appear in Box 1 are not evolving as rotationally mixed single stars.

2.3.4. Defining Class 2 stars

We define *Class 2* stars by the condition that the *observed nitrogen abundance, or its observationally derived upper limit, is higher than the maximum (final) calculated surface nitrogen abundance according to Eq. (2.2) when adopting the observed* $v \sin(i)$ *as rotational velocity in Eq. (2.2).* Stars are thus either of Class 1 or of Class 2. For Class 2 stars, the derived upper limit to the current age is the main sequence lifetime, which yields no age constraint.

However, for a Class 2 stars with a determined nitrogen abundance, we can find the minimum required rotational velocity $v_{\rm min}$ to achieve this nitrogen value for the given mass of the star. Since the surface nitrogen abundance is monotonically increasing with

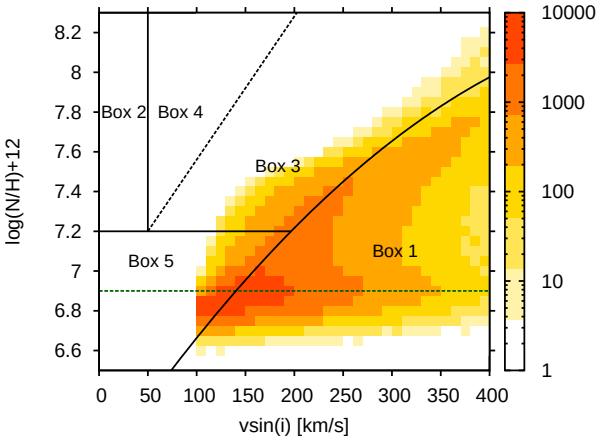

Figure 2.4.: Hunter-diagram of Class 1 stars of a synthetic population of main sequence stars obtained using the STARMAKER code (Brott et al. 2011b). The surface nitrogen abundance is plotted versus the projected surface rotational velocity. The colors indicate the number of Class 1 stars in a given pixel. The absolute scaling is arbitrary. The Hunter-diagram is divided into 5 areas as in (Brott et al. 2011b) to simplify the later analysis.

time, the observed nitrogen abundance will then be produced by a model star at the end of the main sequence evolution ($\tau = 1$), rotating with this minimum velocity. By using the minimum rotational velocity, the maximum inclination angle which is compatible with the observed nitrogen abundance, which we designate as nitrogen inclination i_N, can be derived for the star. The sine of i_N can be calculated as

$$\sin(i_N) = \frac{v \sin(i)}{v_{min}}. \tag{2.4}$$

Figure 2.5 illustrates the analysis of Class 2 stars at the example of the LMC star NGC 2004-30. To calculate the evolution of the surface nitrogen abundance, $M = 19\,M_\odot$ and $v_{ZAMS} = 123$ km/s have been used. The observed nitrogen value of $\mathcal{N} = 7.43$ dex is higher then the predicted one during the whole main sequence evolution. The observed nitrogen value can be reached with a minimum rotational velocity of $v_{min} = 172$ km/s, which leads to $\sin(i_N) = 0.71$ (blue dotted line), i.e. $i_N = 45.6°$.

For Class 2 stars where only an upper limit to the surface nitrogen abundance has been determined, a nitrogen inclination can be determined in the same way, by adopting the

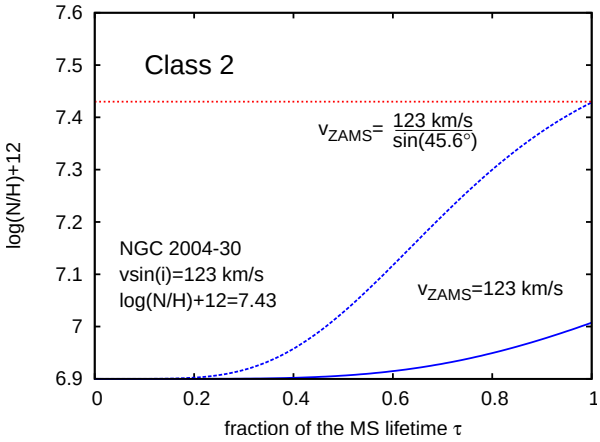

Figure 2.5.: The determination of the nitrogen inclination angle of a Class 2 star is shown for the example NGC 2004-30. The red dotted line indicates the observed surface nitrogen abundance and the blue solid line represents the calculated surface nitrogen abundance as a function of the fraction of the main sequence lifetime using $v_{\rm ZAMS}$ = 123 km/s in Eq. (2.2). The blue dashed line is calculated with a value of the surface rotation velocity of $v_{\rm ZAMS}$ = 173 km/s. This corresponds to an inclination angle of $\sin(i_{\rm N}) = 0.71$.

upper limit as nitrogen abundance. However, in this case, the nitrogen inclination does not provide an upper limit to the true stellar inclination, since lower nitrogen surface abundances would lead to larger nitrogen inclinations. Their values are nevertheless interesting, as shown in Sect. 5 for the Class 2 stars in the SMC.

2.4. Results: Class 1 stars

2.4.1. Isochrone ages

To evaluate the age constraints obtained for Class 1 stars via the nitrogen abundances they are compared to the results from the well proven method of estimating the age of a star through its position in the Hertzsprung-Russel (HR) diagram. The idea is to compare effective temperature and luminosity of the star with isochrones plotted in the HR diagram.

We computed isochrones using non-rotating models of the stellar evolution grids of (Brott et al. 2011a) up to an age of 50 Myr with a step size of 0.2 Myr. Comparing the isochrones with the position of a star the best fitting isochrone defines its isochrone age $t_{\rm isochrone}$ as shown exemplary for the star N 11-95 in Fig. 2.6. The observational error bars imply an uncertainty in the isochrone ages of about ± 1 Myr.

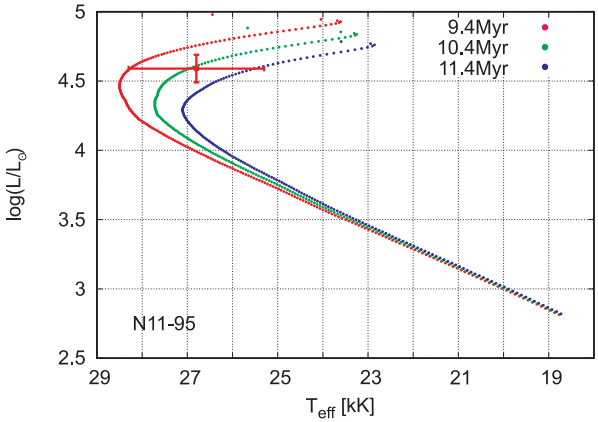

Figure 2.6.: Isochrone fitting in the HR diagram for the LMC star N 11-95, which is indicated by the red point with error bars. The red, green and blue lines are isochrones from non rotating stellar models for different ages. The green line defines the most likely age of the star while red and blue represent maximum and minimum possible current age when considering uncertainties in measured effective temperature and luminosity of the star.

All stars of Class 1 have been analyzed this way to obtain their isochrone age. Since non-rotating models were used, rotational mixing is not considered in estimating the isochrone ages of the stars. However it leads only to negligible errors in the mass and rotational velocity range considered here (see Fig. A.5 in Appendix A.1.1). All isochrone ages are given in Tables A.2 and A.2.

Assuming that the isochrone age reproduces the current age of a star well, our method allows to derive its inclination angle. Due to uncertainties in the isochrone age $t_{\rm isochrone}$, and when using Eq. (A.5) to derive the main sequence lifetime $\tau_{\rm H}$, it is possible that $\tau_{\rm H} < t_{\rm isochrone}$. In this case we limit $t_{\rm isochrone} = \tau_{\rm H}$ (occurred in 3 out of 16 cases). To derive the inclination angle, the isochrone age needs to be smaller than the upper limit to the current age using the nitrogen abundance. Amongst the stars of Class 1 (the method is similar to deriving the inclination angle for Class 2 stars, see Sect. 2.3.4), a

few stars fulfill this condition. The derived inclination angles are given in Tables A.2 and A.2. In particular, we find that the most likely inclination angles of stars L15 (N 11-120) and L42 (NGC 2004-107) are 66° and 62°, respectively, while L6 (N 11-89) and L8 (N 11-102) are seen nearly equator-on.

2.4.2. Nitrogen ages versus isochrone ages

The results of the age constraints through nitrogen are summarized in Tables A.2 and A.2 for all considered stars. Fig. 2.7 shows the upper age limits of our sample stars obtained via nitrogen chronology $t_{\rm N}$, plotted against the ages obtained through isochrone fitting, $t_{\rm isochrone}$. Only stars of Class 1 are depicted. Due to the distinction between Class 1 and Class 2, the stars in Fig. 2.7 are those which have preferentially low surface nitrogen abundances and high projected surface rotational velocities. Figure 2.9 shows the distribution of Class 1 stars in the HR diagram.

Since the projected rotational velocity provides a lower limit to the true rotational velocity of a star, the surface nitrogen abundance results in an upper age limit, i.e., the star is younger or as old as the obtained nitrogen age. Therefore, the upper age limit derived from the surface nitrogen abundance should be larger than the age determined using isochrones, under the assumption that the age of a star is approximated well by the second method. This means that stars should be placed below the green dotted line in Fig. 2.7, which corresponds to $t_{\rm isochrone} = t_{\rm N}$.

Considering that the error in mass is of the order of 10-25% (Mokiem et al. 2006) — which is insignificant given the weak mass dependence of the nitrogen enrichment in the considered mass range (Fig. 2.1) — and the error in $v \sin(i)$ is only about 10% (Hunter et al. 2008b), the error of ±0.2 dex for the surface nitrogen abundance (Hunter et al. 2009) is indeed the dominant one. To estimate its influence, we repeat the analysis for each star, comparing the surface nitrogen abundance according to Eq. (2.2) with an abundance which is 0.2 dex higher or lower than the measured surface nitrogen abundance. The lower nitrogen abundance leads to a decrease while the upper value results in an increase of the upper age limit for the star. The uncertainties of the upper age limit due to the uncertainties in the surface nitrogen abundance are given in Tables A.2 and A.2, and are plotted as horizontal error bars in Fig. 2.7.

The majority of our sample stars are placed above the green dotted line in Fig. 2.7, even when considering the error in their measured surface nitrogen abundance. This contradicts the expected behaviour. For example, the star N 11-95 (star L7 in our sample, see Table A.2) analyzed in Fig. 2.3 has an upper age limit from nitrogen chronology of 5.8 Myr. However, its isochrone age is 10.4 Myr. This means that, according to its

position in the HR diagram, this rapidly rotating star ($v \sin(i) = 267$ km/s) is seen near its TAMS position in the HR diagram, but it has only a modest surface nitrogen enhancement.

Only two out of 17 stars are found in the predicted area (N 11-120=L15, and NGC 2004-107=L42). Considering the uncertainty of ±0.2 dex in the measured surface nitrogen abundance, we see in Fig. 2.7 three more stars (N 11-102=L8, N 11-116=L12, and NGC 330-51=S25) with an error bar reaching into the allowed area, and two further stars (N 11-89=L6 and NGC 2004-88=L35) with an error bar getting very close to the allowed area.

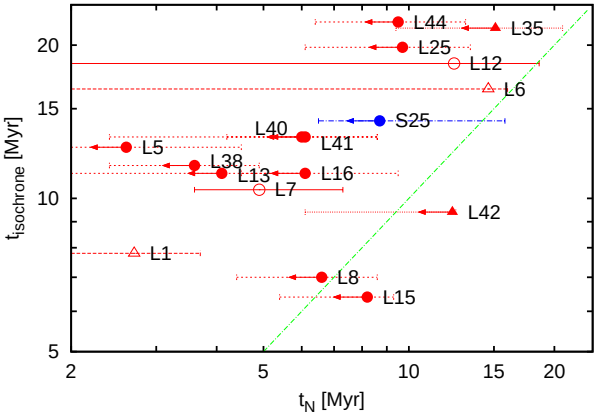

Figure 2.7.: The upper age limits t_N obtained from nitrogen chronology for Class 1 stars are plotted against the ages derived using isochrone fitting in the HR diagram, $t_{\rm isochrone}$. Stars located in the LMC are shown with red symbols while the SMC star is depicted in blue. Stars for which only upper limits to the surface nitrogen abundances could be determined are marked by filled symbols with arrows indicating the direction of change in the results when the surface nitrogen abundance is smaller then the value of the upper limit. Circles mark single stars and triangles indicate probable binaries. The green dotted line is defined by $t_{\rm N} = t_{\rm isochrone}$.

2.4.3. Discussion

As shown above, the nitrogen chronology clearly fails for 10 out of the 17 Class 1 stars in our sample. It is interesting to consider the location of these stars in the Hunter-diagram (Fig. 2.8). It turns out that all 10 stars are located in Box 1. In contrast, amongst

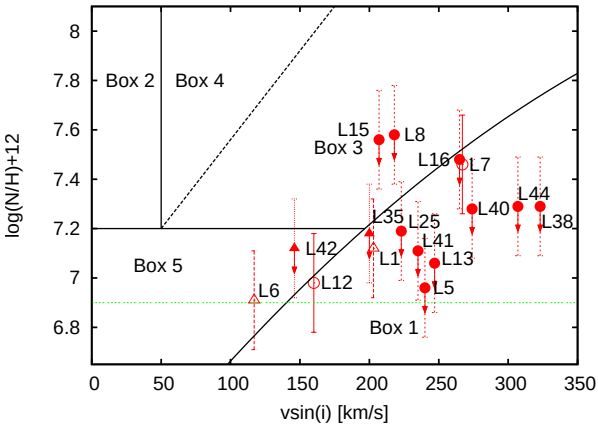

Figure 2.8.: Hunter-diagram of all stars shown in Fig. 2.7. The surface nitrogen abundance is plotted as a function of the projected surface rotational velocity for stars located in the LMC. Upper limits to the surface nitrogen abundance are marked by filled symbols. In addition there is a differentiation between single stars (circles) and probable binaries (triangles). A subdivision into five boxes as defined in Brott et al. (2011b) has been done to simplify the analysis. The green dotted line represents the initial surface nitrogen abundance for LMC B stars.

the 7 stars for which the nitrogen chronology might work, the six LMC stars are found in Box 3 (L8, L15), in Box 5 (L6, L42), or in Box 1 but very near Box 5 (L12, L35). The SMC star S25 can not be compared in the same Hunter-diagram. For the LMC Class 1 stars, also the reverse statement holds: Nitrogen chronology might work for all stars which are not in Box 1, or which are in Box 1 very near Box 5. In other words, a slight shift of the dividing line between Box 5 and Box 1 would result in separating the Class 1 stars for which nitrogen chronology clearly fails (Box 1) from those for which it might work (outside of Box 1).

The isochrone age of the 10 LMC stars in Box 1 for which nitrogen chronology fails is larger than the upper age limit derived from their surface nitrogen abundance, given their rather high projected rotational velocities. Due to the simplicity of our method the revealed conflict can only be due to the stars in Box 1 behaving differently than predicted by the evolutionary models for rotationally mixed single stars of Brott et al. (2011a).

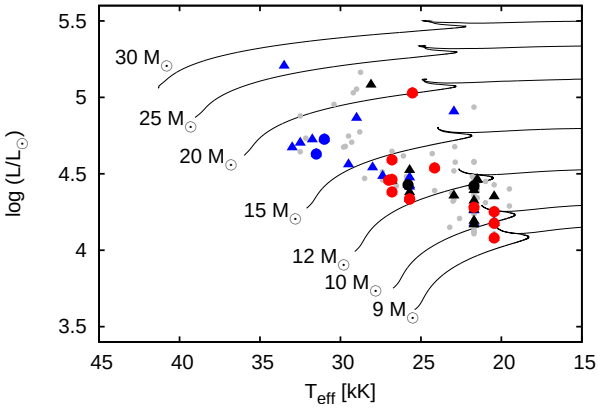

Figure 2.9.: The Hertzsprung-Russel diagram is shown for several evolutionary models (LMC) with initial masses from 9 to 30 $M_{\odot}$ and surface rotational velocities of approximately 200 km/s. Additionally, our sample with LMC-metallicity is depicted. Stars of Class 1 are indicated by circles and stars of Class 2 are represented by triangles. With respect to Fig. 2.8, stars in Box 1 are shown in red, star in Box 3 in blue and stars in Box 5 in black. Grey dots depict the remaining not analyzed stars of the VLT-FLAMES Survey (LMC) after the selection criteria applied in Brott et al. (2011b).

The detailed and tailored population synthesis of the LMC early B type main sequence stars from the FLAMES Survey by Brott et al. (2011b) already pointed out that the stars in Box 1 could, in a statistical sense, not be reproduced through the stellar models of single stars including rotational mixing. Our nitrogen chronology analysis is not a statistical method, but rather considers each star individually. While it uses the same underlying stellar evolution models as Brott et al. (2011b), the latter did not consider age constraints. In this respect, our chronology method provides a new test of the evolutionary models provided by Brott et al. (2011a) which is independent of the results of Brott et al. (2011b). Nevertheless, our result is very much in line with that of Brott et al. (2011b), i.e., that Box 1 stars in our sample are generally not consistent with the models of Brott et al. (2011a).

While the errors due to inaccuracies of our fitting method are mostly insignificant compared to the observational errors in nitrogen, the main theoretical error source could be the systematic error introduced by the physics included in the underlying stellar evolution models. However, the mixing physics (convective overshooting and rota-

tional mixing) in these models was specifically calibrated using the LMC sample of the FLAMES Survey.

We are left with the conclusion that either rotational mixing does not operate in massive stars, or that the stars in Box 1 of the Hunter-diagram (Fig. 2.8) are affected by physics which is not included in the stellar evolution models (e.g., binary effects). In this context, we point out that while rotating stars may well evolve into Box 1 in general (cf. Fig. 2.4), most of them would not be detected in the FLAMES survey, due to the employed magnitude cut-off (cf. Figs. 6 and 10 of Brott et al. (2011b)). The origin of these stars is therefore in question.

For example, it has been shown that binary evolution can place stars into Box 1 in the Hunter-diagram (Langer et al. 2008; de Mink et al. 2011) for which the age constraints derived from nitrogen chronology do not apply. However, while four Class 1 stars in our sample are likely binaries (Fig. 2.7), the remaining twelve show no indication of binarity, despite the fact that multi epoch spectra are available for them. The FLAMES Survey observing campaign was not tailored for binary detection. Applying the method developed by Sana et al. (2009) the limited number of epochs should roughly result in a detection probability of at least 80% for systems with periods up to 100 days, dropping rapidly to a detection rate of less than 20% for periods longer than a year. Furthermore, while some binaries amongst the Box 1 stars may remain undetected, it is the pre-interaction binaries which are more likely to be detected (de Mink et al. 2011). With the data at hand, it therefore seems unlikely that we can evaluate the possibility that binarity by itself can completely explain the situation.

When we apply nitrogen chronology to LMC stars outside of Box 1 in Fig. 2.8 — i.e., to the only stars which can be expected to be compatible with the single star models of Brott et al. (2011a) — the result is positive. While there are only four stars (L6, L8, L15, L42), their nitrogen age is consistent with their isochrone age: They are either in the allowed part of Fig. 2.7 (L42, L15), or nearest to its borderline (L6, L8). As explained above, a slight shift in the borderline between Boxes 1 and 5 in Fig. 2.8 includes two more stars (L12, L35) into this consideration. Together with the SMC star S25, for which can not be considered in Fig. 2.8, there are seven stars for which the nitrogen chronology yields promising and consistent results.

In summary, we conclude that our new method give results for Class 1 stars which are consistent with those from classical isochrones for all stars in the subgroup where this could be expected. Furthermore, it flags contradictions for all stars in the second subgroup which, according to Brott et al. (2011b), are not thought to have evolved as rotationally mixed single stars. For stars of both subgroups, the application of nitrogen chronology is fruitful and provides insights which are not obtainable otherwise.

Obviously, it would be desirable to apply nitrogen chronology to a stellar sample where the observational bias does not exclude Box 1 of the Hunter-diagram to be populated by rotationally mixed single stars — which according to Fig. 2.4 appears indeed possible. While a population of stars which contradict the underlying stellar models (presumably binaries) might still be present in such a sample, expectedly it would be diluted in a dominant population of single stars.

2.5. Results: Class 2 stars

Stars are of Class 2 if the observed surface nitrogen abundance is higher than the predicted value of a star rotating with an unprojected velocity equal to the $v \sin(i)$ of our star at the end of the main sequence. This is the case for most of our sample stars residing in Box 3 of the Hunter-diagram (see Fig. 2.8), which according to the statistical analysis of Brott et al. (2011b) agree reasonably well with the single star evolution models including rotational mixing. None of the LMC Class 2 stars is located in Box 1 of the Hunter-diagram. While we can not derive any age constraints, we can here, relying on single star models with rotational mixing, constrain their inclination angles.

The results of the analysis for our sample are summarized in Tables A.2 and A.2, where we give the upper limits on the inclination angle for all stars. Figure 2.10 depicts the histograms for the nitrogen inclination angles for the 28 LMC and 24 SMC Class 2 stars of our sample. Assuming random orientations of stars, the distribution of $\sin(i)$ increases for increasing values of $\sin(i)$. Since we derive upper limits on the inclinations for stars with determined surface nitrogen abundance, the distribution of those can be expected to be shifted to even higher values.

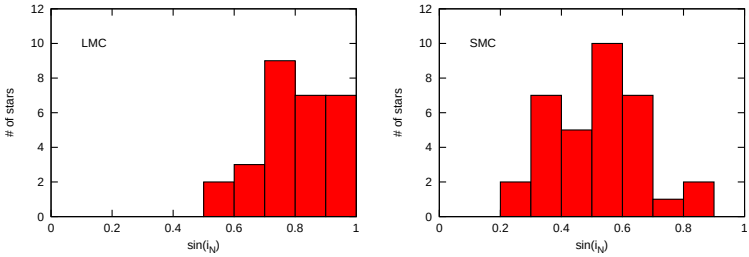

Figure 2.10.: Histograms of the $\sin(i_N)$-values for the Class 2 stars of our sample located in the LMC (left panel) and SMC (right panel). The number of stars within an area of $\Delta \sin(i_N) = 0.1$ were counted.

The expected behaviour is seen for our LMC stars, where the distribution of the sine of the nitrogen inclination angles favours high values with a maximum between 0.7 and 0.8. We refrain from a further analysis of this histogram since the selection of Class 2 stars introduces a bias against the fastest rotators (see Fig. 2.4). While the number of very fast rotators is small, this introduces a bias in our distribution which is difficult to account for.

However, it is interesting to note that the distribution of the nitrogen inclination angles of the SMC stars shows a different behaviour. Here, high values are rare and the average $\sin(i_{\rm N})$ value is about 0.5.

For most SMC stars, only an upper limit to the surface nitrogen abundance is known. The higher his limit, the lower is the $\sin(i_{\rm N})$ value required to reach this value. Thus, if the true surface nitrogen abundance is below the value of the upper limit, the $\sin(i_{\rm N})$ value derived from the upper limit will be smaller than the one which would be derived from the true nitrogen abundance. This implies that the $\sin(i_{\rm N})$ value derived from an upper limit on nitrogen may be smaller than the true $\sin i$-value of the star. Therefore the maximum, or mean, of the $\sin(i_{\rm N})$ distribution can be located at lower $\sin(i)$-values than the maximum of the true $\sin(i)$ distribution.

Interpreting the distribution of nitrogen inclinations of the SMC stars in Fig. 2.10 in this way, and assuming randomly oriented rotational axes of these stars, we conclude that the nitrogen upper limits derived for many of the SMC stars are significantly larger than their true nitrogen abundances. Considering Fig. 7 of Hunter et al. (2009), which compares the location of the SMC stars with evolutionary tracks in the Hunter-diagram, one can see that such a significant shift would indeed be required to bring the observations into agreement with the models.

Similar to the analysis of Class 1 stars, we can use the isochrone ages of Class 2 stars with determined nitrogen abundance to derive their inclination angles. If only an upper limit to the surface nitrogen abundance is known, a lower limit to the true inclination angle can be found. These inclination angles are designated as $i_{\rm isochrone}$ and their sine is given in Tables A.2 and A.2 for all sample stars.

2.6. Conclusions

We present a new method of nitrogen chronology, which can constrain the age of a star, and/or its inclination angle, based on its observed surface nitrogen abundance, mass and projected surface rotational velocity, by comparing the observed nitrogen abundance with the one predicted by the theory of rotational mixing in single stars.

This method can be applied to stars when their surface nitrogen abundance increases monotonically with time during the main sequence evolution. It has been worked out here for stars in the mass range between 5 $M_{\odot}$ and up to 35–50 $M_{\odot}$, and for metallicities adequate for the Milky Way, the LMC and the SMC, based on the stellar evolution models of Brott et al. (2011a). We apply our method to 79 stars from the early B type LMC and SMC samples of the VLT-FLAMES Survey of Massive Stars (Evans et al. 2005, 2006).

Age constraints from nitrogen chronology could be obtained for 17 of the 79 analyzed stars. In Sect. 4.2, we compared those to ages of these stars as derived from isochrone fitting in the HR diagram (Fig. 2.7). We found the isochrone ages of 10 objects to be incompatible with their nitrogen age constraints. Based on their rapid rotation and low nitrogen enrichment, Brott et al. (2011b) concluded that these 10 stars did not evolve as rotationally mixed single stars. Our star-by-star analysis of these objects is reinforcing their conclusion that the weakly enriched fast rotators in the LMC early B stars of the FLAMES Survey — which are 15% of the survey stars — can not be explained by rotating single stars.

For the remaining 7 stars with nitrogen age constraints, six LMC and one SMC star, nitrogen and isochrone ages are found to be consistent within error estimates. Four of them show good agreement, which also allows to derive their inclination angles (Sect. 4.2).

We conclude that our nitrogen chronology results are consistent with the isochrone method for stars which have no indication of an unusual evolution, but incompatible for stars which are suspected binary product according to Brott et al. (2011b). Therefore, our new method provides important new results for both groups of stars. However, it is clearly desirable to obtain larger samples of stars especially of the first group.

For the 62 stars (28 LMC and 34 SMC stars) for which no age constraint could be derived, our method provides limits on the inclination for each object (Sect. 5). While the results for the LMC stars are roughly consistent with random inclination angles, this appears to be different for the SMC stars, for which only upper limits to the nitrogen abundance are available in most cases (Hunter et al. 2009). We argue that random inclinations are also realized for the SMC stars, with the implication that the true nitrogen surface abundances of most SMC stars are significantly below the derived upper limits.

We believe that our new method can be used in the near future to provide further tests of the theory of rotational mixing in stars, and — if such tests converge to confirm this theory — to act as a new chronometer to constrain the ages of massive main sequence stars.

Based on the method presented here, a web tool[1] can be found online. For given mass, (projected) surface rotational velocity and metallicity, the surface nitrogen abundance is calculated and compared to the observed surface nitrogen abundance to constrain the age and inclination angle.

Acknowledgements: We acknowledge fruitful discussions with Hugues Sana, and are grateful to an anonymous referee for helpful comments on an earlier version of this paper.

[1] http://www.astro.uni-bonn.de/stars/resources.html

3. The evolution of rotating very massive stars with LMC composition

Published in Astronomy& Astrophysics, Volume 573, id.A71, 23 on 19 December 2014.
Authors: K. Köhler[1], N. Langer[1] A. de Koter[2,3], S. E. de Mink[2,4,5], P. A. Crowther[6], C. J. Evans[7], G. Gräfener[8], H. Sana[9], D. Sanyaland[1], F. R. N. Schneider[1] and J. S. Vink[8]

[1] Argelander-Institut für Astronomie der Universität Bonn,
Auf dem Hügel 71, 53121 Bonn, Germany
[2] Astronomical Institute Anton Pannekoek, University of Amsterdam,
Science Park 904, 1098 XH, Amsterdam, The Netherlands
[3] Instituut voor Sterrenkunde, KU Leuven,
Celestijnenlaan 200D, 3011 Leuven, Belgium
[4] Observatories of the Carnegie Institution for Science,
813 Santa Barbara St, Pasadena, CA 91101, USA
[5] Cahill Center for Astrophysics, California Institute of Technology,
Pasadena, CA 91125, USA
[6] Department of Physics & Astronomy, University of Sheffield,
Sheffield, S3 7RH
[7] UK Astronomy Technology Centre, Royal Observatory Edinburgh,
Blackford Hill, Edinburgh, EH9 3HJ, UK
[8] Armagh Observatory,
College Hill, Armagh BT61 9DG, UK
[9] Space Telescope Science Institute,
3700 San Martin Drive, Baltimore, MD 21218, USA

ABSTRACT:

Context: With growing evidence for the existence of very massive stars at subsolar metallicity, there is an increased need for corresponding stellar evolution models.

Aims: We present a dense model grid with a tailored input chemical composition appropriate for the Large Magellanic Cloud.

Methods: We use a one-dimensional hydrodynamic stellar evolution code, which accounts for rotation, transport of angular momentum by magnetic fields, and stellar wind mass loss to compute our detailed models. We calculate stellar evolution models with initial masses from 70 to 500 $M_\odot$ and with initial surface rotational velocities from 0 to 550 km/s, covering the core-hydrogen burning phase of evolution.

Results: We find our rapid rotators to be strongly influenced by rotationally induced mixing of helium, with quasi-chemically homogeneous evolution occurring for the fastest rotating models. Above $160M_\odot$, homogeneous evolution is also established through mass loss, producing pure helium stars at core hydrogen exhaustion independent of the initial rotation rate. Surface nitrogen enrichment is also found for slower rotators, even for stars that lose only a small fraction of their initial mass. For models above $\sim 150M_\odot$ at zero age, and for models in the whole considered mass range later on, we find a considerable envelope inflation due to the proximity of these models to their Eddington limit. This leads to a maximum zero-age main sequence surface temperature of $\sim 56\,000$ K, at $\sim 180\,M_\odot$, and to an evolution of stars in the mass range $50M_\odot \ldots 100M_\odot$ to the regime of luminous blue variables in the Hertzsprung-Russell diagram with high internal Eddington factors. Inflation also leads to decreasing surface temperatures during the chemically homogeneous evolution of stars above $\sim 180\,M_\odot$.

Conclusions: The cool surface temperatures due to the envelope inflation in our models lead to an enhanced mass loss, which prevents stars at LMC metallicity from evolving into pair-instability supernovae. The corresponding spin-down will also prevent very massive LMC stars to produce long-duration gamma-ray bursts, which might, however, originate from lower masses.

Keywords: stars: massive - stars: evolution - stars: rotation - stars: abundances - stars: early type

3.1. Introduction

Massive stars, with initial masses above $\sim 8M_\odot$, are powerful cosmic engines (Bresolin et al. 2008). They produce copious amounts of ionizing photons, strong stellar winds, energetic final explosions, and most of the heavy elements in the Universe. The most massive amongst them conduct a life very close to their Eddington limit, and may thus be prone to become unstable. They are thought to be able to produce the most spectac-

ular stellar explosions, like hypernovae, pair-instability supernovae, and long-duration gamma-ray bursts (Langer 2012).

While the value of the upper mass limit of stars is presently uncertain (Schneider et al. 2014a), there is a great deal of evidence of stars with initial masses well above $100 M_{\odot}$ in the local Universe. A number of close binary stars have been found with component initial masses above $100 M_{\odot}$ (Schnurr et al. 2008, 2009; Sana et al. 2013b). Crowther et al. (2010) proposed initial masses of up to $300 M_{\odot}$ for several stars in the Large Magellanic Cloud (LMC) based on their luminosities.

We present stellar evolution models of very massive rotating core-hydrogen burning stars, with initial masses up to $500\,M_{\odot}$. These models will be used for comparison with the VLT FLAMES Tarantula survey (Evans et al. 2011), which observed more than 800 O and early-B stars in the 30 Doradus region located in the Large Magellanic Cloud, to study the effects of rotational mixing and mass loss on the evolution of very massive stars.

Stellar evolution models for very massive stars have already been presented (see Table 1 in Maeder & Meynet (2011) and references therein). In particular, we refer to the rotating stellar models of Crowther et al. (2010); Yusof et al. (2013), who calculated models with initial masses up to $500\,M_{\odot}$. It is the aim of this paper to present a grid of stellar evolution models that has a dense spacing in mass and rotation rates, such that it is suitable for forthcoming population synthesis calculations. In this sense, our models are an extension of the LMC models of Brott et al. (2011a) to higher masses. In the mass range considered here, stellar wind mass loss and the proximity to the Eddington limit play prominent roles.

In Sect. 3.2 we briefly describe the employed stellar evolution code, including the input parameters for our calculations. Following that, we present and discuss the stellar evolution models in Sect. 3.3, including the evolution of their mass and their surface abundances, with emphasis on chemically homogeneous evolution, and we compare our models with previous work in Sect. 3.4. Section 3.5 contains our short summary. In Appendix A.1.1, we present isochrones derived from our models, as functions of age and initial stellar rotation rate.

3.2. Input physics and assumptions

Brott et al. (2011a) computed three grids of stellar evolution models for different metallicities (Galactic, SMC, LMC) for initial masses up to $60\,M_{\odot}$, which were compared with the results of the VLT-FLAMES Survey of Massive Stars (Evans et al. 2005, 2006). In particular, the convective core overshooting parameter and the efficiency parameters

for rotationally induced mixing used by Brott et al. (2011a) were calibrated to reproduce the results of this survey (Hunter et al. 2008a). The dense spacing in initial mass and rotational velocity used for the grid of Brott et al. (2011a) opened the door for statistical tests of the theory of massive star evolution (Brott et al. (2011b); Schneider et al., in preparation). Here, we extend the LMC grid of Brott et al. up to initial masses of $500\,M_{\odot}$, using the same numerical code, physical assumptions, and a similarly dense grid spacing.

To calculate rotating stellar evolution models, we use our one-dimensional hydrodynamic binary stellar evolution code (BEC) which is described in Heger et al. (2000); Petrovic et al. (2005), and Yoon et al. (2012). It contains a detailed treatment of rotation, angular momentum transport due to internal magnetic fields, and stellar wind mass loss. The code solves all five stellar structure equations throughout the stellar interior, including the stellar envelope up to a Rosseland optical depth of $\tau = 2/3$. Convection is considered throughout the star using the non-adiabatic mixing-length theory. Our code is suited to treating stars close to the Eddington limit, and to describe the effects of envelope inflation which occur in this situation (Ishii et al. 1999; Petrovic et al. 2006).

3.2.1. Chemical composition

The initial chemical composition for our models is chosen according to corresponding observations of young massive stars and of H II-regions in the LMC (Brott et al. 2011a). We thus adopt initial mass fractions for hydrogen, helium, and the sum of all metals of $X = 0.7391$, $Y = 0.2562$, and $Z = 0.0047$, respectively, with a non-solar metal abundance pattern (see Tables 1 and 2 in Brott et al.). We note that the applied opacities and mass loss rates (see below) are scaled with the LMC iron abundance, not with the total metallicity, which is reduced by 0.35 dex with respect to that of the Sun.

3.2.2. Convection and rotational mixing

Convection with a mixing-length parameter of $\alpha_{\rm MLT} = 1.5$ (Böhm-Vitense 1958; Langer 1991) is applied as well as semi-convection with an efficiency parameter of $\alpha_{\rm SEM} = 1$ (Langer et al. 1983; Langer 1991). In addition to convection, convective core overshooting is included with $\alpha_{\rm over} = 0.335$ local pressure scale heights, as calibrated in Brott et al. (2011a) with the rotational properties of B-type stars (Hunter et al. 2008a; Vink et al. 2010) from the VLT-FLAMES survey. While no observational calibration of the overshooting parameter exists for stars of the considered mass range, we point out that the role of overshooting in our models is minor because of the large convective core mass fractions of very massive stars.

Rotational mixing (Heger et al. 2000) is considered with the efficiency parameters of $f_c = 0.0228$ and $f_\mu = 0.1$ (Brott et al. 2011a). The most significant process causing rotationally induced mixing in our models is the Eddington Sweet circulation. Furthermore, the transport of angular momentum by magnetic fields due to the Spruit-Taylor dynamo (Spruit 2002) is applied, which is assumed here not to lead to an additional transport of chemical elements (Spruit 2006). Since the magnetic torques lead to a shallow angular velocity profile in our models, the effects of the shear instability, although included, are quite limited during the main sequence evolution.

3.2.3. Mass loss

The evolution of very massive stars is intimately connected to their mass-loss behaviour. Mass loss of very massive stars, for which few observational constraints exist, is a very active field of research. Here, we provide a brief overview of the mass loss prescriptions adopted in our calculations.

From the zero-age main sequence up to a surface helium fraction $Y_s = 0.4$, we use the mass-loss predictions by Vink et al. (2000, 2001) for O and B stars. These rates are valid for stars of one million solar luminosities or less, i.e. stars below $80\,M_\odot$ (Mokiem et al. 2007), which are not very close to their Eddington limit (i.e. have $\Gamma \lesssim 0.3$; see Eq. 3.3). Empirical tests of these predictions depend critically on the presence and properties of small scale structures in the outflows, known as clumping. Mokiem et al. (2007) showed on the basis of Hα and He II λ4686 analysis that the predicted rates agree with observations if the material is concentrated in clumps that have a 3–4 times higher density than in a smooth outflow. Other analyses, which include modelling of ultraviolet resonance lines, derive clumping factors that may reach values of 10 (e.g. Bouret (2004); Bouret et al. (2005, 2012); Fullerton et al. (2006)). In this last case, the Vink et al. prescription adopted here may overestimate $\dot{M}$ by about a factor of 2. An improved hydrodynamical treatment shows that for normal O stars the mass loss rates may be somewhat lower (Müller & Vink 2008; Muijres et al. 2012).

Predictions for stars in the 40–300 $M_\odot$ range have been presented by Vink et al. (2011a). Objects at the upper mass end of this range may have a very high Eddington factor Γ. It has been found that, at solar metallicity, the wind strengths agree with the standard Vink et al. recipe for objects that have an Eddington factor for Thomson scattering of $\Gamma_e \lesssim 0.7$. For higher Γ_e values these new predictions show an upturn in the mass-loss rate, leading to rates that are higher by up to about a factor of 2 compared to the Vink et al. values used here. The authors associate the upturn with the stellar wind becoming optically thick, i.e. leading to spectral morphology which is typical for

Wolf-Rayet stars of nitrogen subclass (WN) showing hydrogen emission lines. Interestingly, this predicted upturn may have been confirmed observationally (Bestenlehner et al. 2014). The relation between mass loss and Eddington factor has also been explored for late-WN stars by Gräfener & Hamann (2008a) and Gräfener et al. (2011). They find a behaviour that is similar to the results of Vink et al. (2011a), though the onset of Wolf-Rayet type outflows occurs at lower Γ_e values. Gräfener & Hamann however report a temperature dependence of their mass-loss rates that is steeper than that of Vink et al. (2011a).

Since the mass loss predictions for large Eddington factors cannot yet be implemented unambiguously into stellar evolution calculations, we extrapolate the Vink et al. (2001) rates for stars above $10^6 L_\odot$. We note that Crowther et al. (2010) found the Vink et al. rates to agree within error bars with those observed in stars of up to $\sim 10^7 L_\odot$ found in 30 Doradus. For objects in the range $60 \ldots 100\, M_\odot$ the objects are close to the model-independent mass-loss transition point between optically thin and thick winds. In this range mass-loss rates have recently been calibrated with an uncertainty of only ~30% (Vink & Gräfener 2012).

The Vink et al. mass-loss prescription shows a bi-stability jump at about 25 000 K, leading to an increase of the mass-loss rate by a factor of 5 for stars of spectral type B1.5 or later. We include this bi-stability jump in our calculations (cf. Brott et al. (2011a)).

Additionally the Nieuwenhuijzen & de Jager (1990) empirical mass-loss rate is applied to cope with an increase in mass loss when approaching the Humphreys-Davidson limit (HD limit). The transition from Vink et al. (2000, 2001) to Nieuwenhuijzen & de Jager (1990) occurs at any effective temperature smaller than 22 000 K where the Nieuwenhuijzen & de Jager (1990) mass-loss rate exceeds the Vink et al. (2000, 2001) mass-loss rate.

To account for Wolf-Rayet mass loss, the Hamann et al. (1995) mass-loss rate divided by a factor of 10 is applied for the surface helium fraction $Y_s \geq 0.7$. Figure 1 in Yoon et al. (2010) shows that this corresponds well to the Wolf-Rayet mass-loss rate proposed by Nugis & Lamers (2000) for Wolf-Rayet masses in the range $5M_\odot$ to $20M_\odot$. For surface helium mass fractions from $0.4 \leq Y_s \leq 0.7$ the mass-loss rate is linearly interpolated between either the Vink et al. (2000, 2001) or the Nieuwenhuijzen & de Jager (1990) mass-loss rate and that of Hamann et al. (1995).

We apply a mass-loss enhancement for stars near critical rotation as in Yoon & Langer (2005) which considers a reduction of the critical rotational velocity for stars near their Eddington limit. It is still unclear whether rapid rotation per se leads to an enhanced mass loss (Müller & Vink 2014), but it appears reasonable to consider that the mass-

loss rate increases close to the Eddington limit, which is indeed reached sooner for rotating objects (Langer 1997).

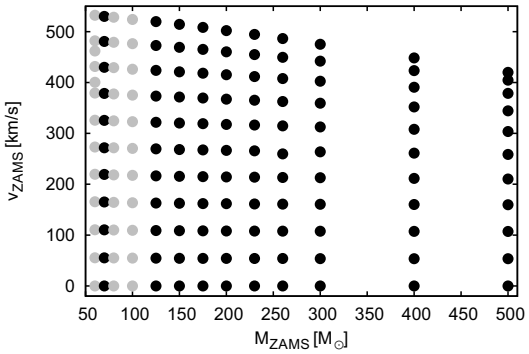

Figure 3.1.: Initial equatorial rotational velocity versus initial mass. Each dot in this diagram represents the evolutionary sequence in our model grid with the corresponding initial parameters. Grey dots correspond to models presented in Brott et al. (2011a) as well as previously unpublished models calculated by I. Brott, while black dots represent the 110 newly computed evolutionary sequences.

3.2.4. Model grid

Figure 3.1 gives an overview of our grid of evolution models by indicating the initial masses and initial surface rotational velocities of all computed model sequences. Because of the increase in the Eddington factor with mass, we decrease the maximum initial rotational velocity for higher masses in order to avoid strong rotationally induced mass loss already on the zero-age main sequence (Langer 1998). Whereas most sequences are computed to core-hydrogen exhaustion, some of the most massive and most rapidly rotating models were stopped shortly before their proximity to the Eddington limit caused numerical difficulties.

3.3. Results

3.3.1. Evolutionary tracks in the HR-diagram

A selection of stellar evolution tracks is presented in Fig. 3.2. The luminosity of the stellar models for a given initial mass and initial surface rotational velocity is shown as a function of their effective temperature. Tracks are shown for nine different initial masses from 60 $M_\odot$ to 500 $M_\odot$, with initial surface rotational velocities of 0 km/s, 400 km/s, and 500 km/s.

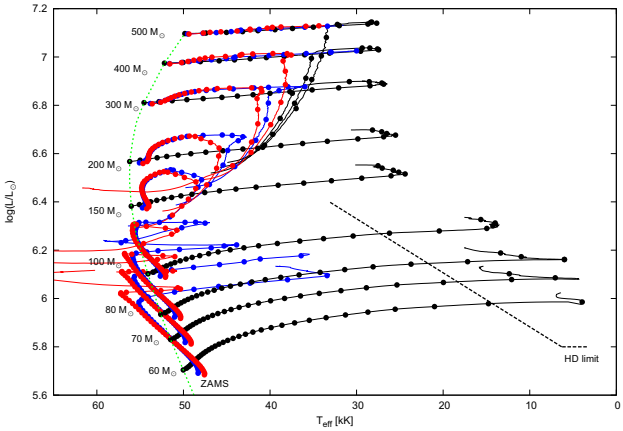

Figure 3.2.: Evolutionary tracks of massive stars during their core hydrogen burning evolution in the Hertzsprung-Russell diagram. For each selected initial mass (as labelled), tracks are shown for three different initial surface rotational velocities, $v_{\rm ZAMS} = 0, 400, 500$ km/s, in black, blue, and red, respectively. The time difference between two successive dots on each track is 10^5 yr. The zero-age main sequence is drawn as a green dashed line. The end of the tracks corresponds to the terminal age main sequence. The approximate location of the Humphreys-Davidson limit is indicated by the black dashed line (Humphreys & Davidson 1994).

Up to a luminosity of $\log L/L_\odot \simeq 6.5$, at about 190 $M_\odot$, the effective temperature of the ZAMS increases with increasing luminosity. For higher initial masses this behaviour

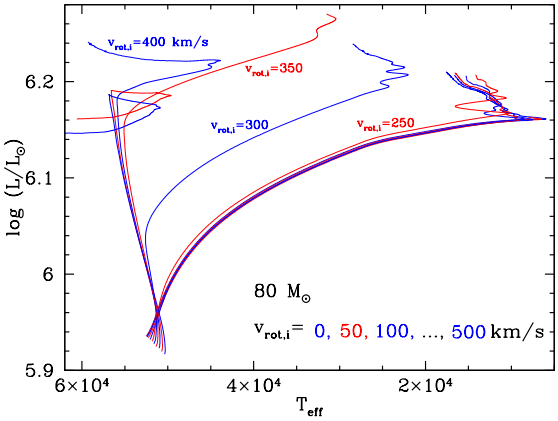

Figure 3.3.: Evolutionary tracks of stars with an initial mass of $80 M_{\odot}$, for initial rotational velocities of 0, 50, 100, 150, 200, 250, 300, 350, 400, 450, and 500 km/s. Tracks with initial velocities that are even multiples of 50 km/s are drawn in blue, odd multiples in red.

changes. The ZAMS moves towards lower effective temperature with increasing luminosity as a result of stars having significantly increased radii and as a consequence of their proximity to the Eddington limit. This effect is discussed in more detail in Sect. 3.3.6.

Figure 3.2 shows only the tracks of the slowest and fastest rotators in our grid. However, we point out that in the HR-diagram, the evolutionary tracks do not change much below an initial rotational velocity of ~ 250 km/s. This is demonstrated by the example of $80 M_{\odot}$ models in Fig. 3.3, for which only the tracks with initial rotational velocities of ~ 300 km/s and higher deviate significantly from the track of the model without rotation. As shown in Sect. 3.3.3, this is due to the absence of significant rotationally induced mixing of helium below the threshold rotational velocity for quasi-chemically homogeneous evolution (cf. Brott et al. (2011a)). We note that although the evolutionary tracks of the sequences computed with initial rotational velocities below ~ 250 km/s are almost identical, the corresponding models show significant differences concerning the evolution of the surface abundances of trace elements, e.g. boron and nitrogen (cf. Sect. 3.3.3).

The models without significant mixing of helium, in the mass range between $60 M_{\odot}$ and $80 M_{\odot}$, expand during core hydrogen burning to surface temperatures as low as

5000 K. This occurs partly because of the relatively large amount of convective core overshooting in our models. A second reason is that when these models evolve through core hydrogen burning, they approach the Eddington limit because their L/M ratio is increasing, and at the same time their envelope opacity is increasing as cooler surface temperatures are achieved (cf. Sect. 3.3.6). For higher initial masses, the redward evolution is truncated at $T_{\rm eff} \simeq 25\,000$ K because of the bi-stability mass-loss enhancement in the Vink et al. (2000) mass-loss recipe and the assumed mass-loss enhancement for stars near their Eddington limit (Sect. 3.2).

Figure 3.2 shows that the evolutionary tracks of even our slowly rotating models avoid the upper-right corner of the HR diagram. This is remarkable, since our very massive star models evolve very close to their Eddington limit, which leads to an inflation of the envelope (cf. Sect. 3.3.6). We find that the high mass-loss rates at temperatures below $\sim$ 30 000 K lead to significant helium enrichments for all stars above $\sim 60 M_\odot$ (cf. Sect. 3.3.3) such that, as core hydrogen burning continues, they evolve towards hotter rather than cooler surface temperatures.

Figure 3.2 also contains the empirical upper luminosity boundary of stars in the Milky Way, as derived by Humphreys & Davidson (1994). As we see, our slowly rotating models do penetrate the Humphreys-Davidson (HD) limit and spend a significant amount of time at cooler temperatures. Whether this prediction is in contradiction with observations for the LMC is currently unclear. The stellar statistics near the HD limit for LMC stars from published work is not very good (Fitzpatrick & Garmany 1990). And even in the Milky Way, stars above the HD limit are observed, the most prominent example being η Carinae with a luminosity of $\log L/L_\odot = 6.7$ and $T_{\rm eff} \simeq 30\,000$ K (Smith 2013).

In any case, our models predict a short lived ($\sim 10^5$ yr) yellow or red supergiant phase of stars in the mass range $60 M_\odot$ to $80 M_\odot$ during which the core is still burning hydrogen. Our models obtain a stellar wind mass-loss rate of the order of $10^{-4} M_\odot\,{\rm yr}^{-1}$ during this stage. However, in this part of the HR diagram, mass-loss rates are very uncertain. We note that in particular higher mass-loss rates (which may be due to the pulsational instability of these models; Sanyal et al., in prep.) would lead to shorter life times in this evolutionary stage.

The higher the initial mass of our model, the higher is their convective core mass fraction. While it exceeds 80% in zero-age main sequence stars above $100 M_\odot$, it reaches 90% at $300 M_\odot$, and $500 M_\odot$ stars with a convective core mass fraction of 95% are almost fully convective. This puts the convective core boundary far out into the stellar envelope, where the pressure scale height is rather small. Consequently, convective core overshooting does not have the same importance as at smaller stellar mass and plays only a minor role in most of the models presented here.

The effect of rotation on the evolution of massive stars is discussed previously, for example in Maeder & Meynet (2000b); Heger & Langer (2000); Brott et al. (2011a); Chieffi & Limongi (2013). In our models, there are two main changes in the stellar evolution tracks in the HR diagram. First, the effective gravity is reduced as a result of the centrifugal acceleration, which leads to a decrease in the effective temperature and luminosity of a star compared to a non-rotating model. Second, above a threshold rotational velocity for which the timescale of rotational mixing becomes smaller than the nuclear timescale, the stars evolve quasi-chemically homogeneously (Yoon & Langer 2005; Woosley & Heger 2006), and the corresponding models evolve directly towards the helium main sequence in the HR-diagram (Brott et al. 2011a).

Both effects are clearly visible in our models. For stellar evolution tracks with initial rotational velocities below 250 km/s, the first effect mentioned is dominant. It can be recognized most easily from the ZAMS position of our stellar models (Figs. 3.2 and 3.3), where the models are dimmer and cooler the faster they rotate.

The most rapidly rotating stellar models undergo quasi-chemically homogeneous evolution. As displayed in Fig. 3.2 for $v_{\rm ZAMS} = 400, 500$ km/s, those with initial masses below $\sim 125 M_\odot$ show a strong increase in luminosity and effective temperature. For more massive models, however, homogeneous evolution also leads to higher luminosities, but the surface temperature is decreased. Towards core helium exhaustion, strong Wolf-Rayet mass loss leads these stars to lower luminosities and larger surface temperatures (cf. Sect. 3.3.2). We return to the discussion of quasi-chemically homogeneous evolution in Sect. 3.3.4. Isochrones in the HR-diagram based on tracks discussed here are presented in Appendix A.

3.3.2. Mass loss and surface rotational velocity

The evolution of the models for the most massive stars is strongly affected by mass loss. According to our mass-loss prescription (Sect. 3.2), our models undergo mass loss of three different strengths. Initially, the mass-loss rate proposed by Vink et al. (2000, 2001) is used. For our adopted composition, the mass-loss rate is initially of the order of $3 \cdot 10^{-6} M_\odot\,{\rm yr}^{-1}$ for the $100 M_\odot$ models, while for the $500 M_\odot$ models it is $\sim 6 \cdot 10^{-5} M_\odot\,{\rm yr}^{-1}$. At this rate, only 10-20% of the initial mass will be lost over the lifetime of the stars (Fig. 3.4, right panel).

The models that do not experience quasi-homogeneous evolution undergo an increase in their mass-loss rate at effective temperatures of $\sim 25\,000$ K, which is referred to as the bi-stability jump (Vink et al. 1999), according to the Vink et al. prescription (Fig. 3.4). The corresponding mass loss is so intense that the models above $100 M_\odot$ stop evolving

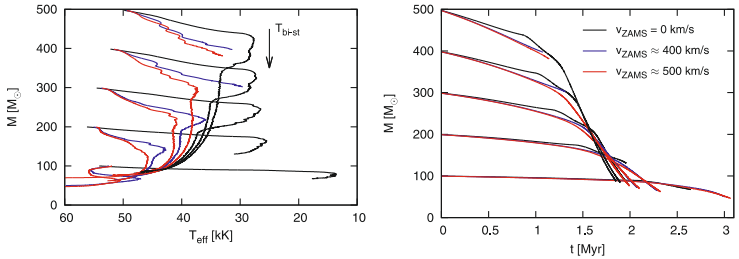

Figure 3.4.: Mass as a function of effective temperature (left panel) and as a function of time (right panel). Stellar models that evolve towards effective temperatures below 27 000 K are affected by the bi-stability jump leading to an increase in the mass-loss rate. This is followed by a change in the slope of the mass as a function of time. The increase in mass-loss rate for rapidly rotating models is related to the change to the Hamann et al. (1995) mass-loss recipe.

redward at this stage, since their surfaces become strongly helium-enriched. For our most massive models, the $500 M_\odot$ sequences, the maximum mass-loss rate at this stage is about $2 \cdot 10^{-4} M_\odot \, \mathrm{yr}^{-1}$.

Once the surface helium mass fraction has increased owing to mass loss to more than 40%, the Wolf-Rayet mass-loss rate is phased in, reaching its full strength at a surface helium mass fraction of 70%. As a consequence, our $100 - 500 M_\odot$ models lose 50-80% of their initial mass before core hydrogen exhaustion. During the phase of Wolf-Rayet winds, the models evolve at decreasing luminosity and all accumulate in a narrow region in the HR-diagram (Fig. 3.2).

The three different phases of mass loss can be clearly seen in both panels of Fig. 3.4. Again, for our most extreme models, the slowly rotating stars with an initial mass of $\sim 500 M_\odot$, the largest obtained mass-loss rate is $\sim 5 \cdot 10^{-4} M_\odot \, \mathrm{yr}^{-1}$, according to our Wolf-Rayet mass-loss prescription. At this moment, the stars have a luminosity of $\log L/L_\odot \simeq 7.1$. Assuming a terminal wind speed of 1000 km/s, we compute a wind-momentum-to-photon-momentum ratio of $\eta \simeq 2$ for this situation. With the same numbers, we obtain a wind-kinetic-energy-to-luminosity ratio of 0.003. The corresponding wind darkening is therefore negligible (Heger & Langer 1996) and significantly smaller than in Galactic Wolf-Rayet stars (Lucy & Abbott 1993).

The models that evolve quasi-homogeneously first increase their luminosity more than the models described above. Consequently, their mass-loss rate becomes larger than that of the inhomogeneous models. The homogeneous models do not reach the bi-stability limit as the increased helium surface abundance due to rotational mixing keeps

their surface temperature above 25 000 K. However, they can reach the Wolf-Rayet stage earlier, and in the end lose similar amounts of mass as the inhomogeneous models. During the Wolf-Rayet stage, there are no clear characteristics that can distinguish between the two types of evolution.

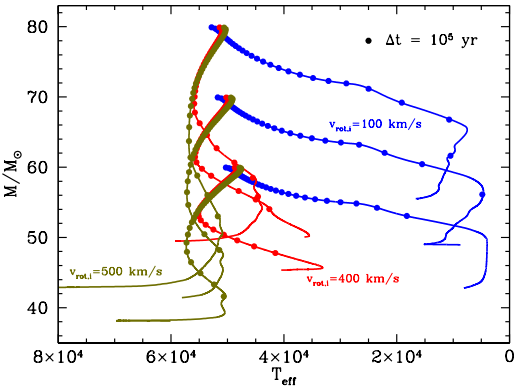

Figure 3.5.: Mass as a function of effective temperature for the models with initial masses of $60M_{\odot}$, $70M_{\odot}$, and $80M_{\odot}$, and for initial rotational velocities of 100, 400, and 500 km/s, as indicated. The time difference between two dots along each of the tracks is 10^5 yr.

Figure 3.5 compares the mass evolution of the homogeneously and inhomogeneously evolving $60M_{\odot}$ to $80M_{\odot}$ models. It shows that in this mass range, the homogeneously evolving models lose more mass, with more than half of the mass being lost during the Wolf-Rayet phase. The inhomogeneously evolving models lose almost equal amounts during their evolution through the hot part of the HR-diagram as at cool surface temperatures, where the latter mass loss occurs on a timescale of only 10^5 yr.

As a consequence of the initially rather moderate stellar wind mass loss, most of our models evolve at a constant rotational velocity for most of the core hydrogen burning. In this case the loss of angular momentum through the stellar wind (Langer 1998) and the increased momentum of inertia due to expansion is compensated by the transport of angular momentum from the contracting core to the envelope. As shown in Fig. 3.6, this holds even for the most massive stars in our grid. Only the models which undergo chemically homogeneous evolution, as a result of their increased luminosity and mass-

loss rate, show a moderate decline of their surface rotational velocity before entering the phase of Wolf-Rayet winds.

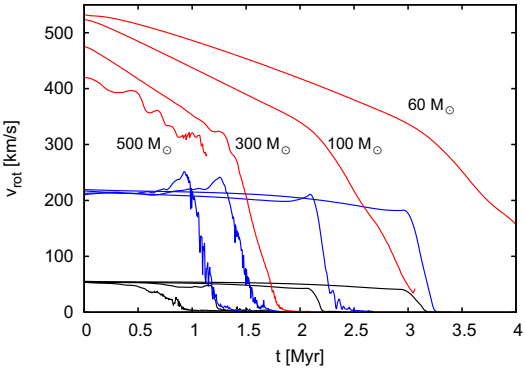

Figure 3.6.: The surface rotational velocity is shown as a function of time for stellar model sequences with four different initial masses (as indicated), and for three initial surface rotational velocities. The rapid decrease in rotation rate seen for $v_i \simeq 50, 200$ km/s is caused by the enhanced mass loss at the bi-stability jump, whereas the steep decline of the rotation velocity for the fast rotators ($v_i \simeq 500$ km/s) is a consequence of Wolf-Rayet type mass loss.

The strong mass loss for $T_{\rm eff} < 25\,000$ K for the inhomogeneously evolving models, and the Wolf-Rayet type mass loss for the homogeneously evolving ones both lead to a strong spin-down of the stars towards the end of their core-hydrogen burning evolution. In fact, this is only avoided for stars initially below $\sim 30 M_\odot$ (cf. Fig. 3 of Vink et al. (2010)). Since the magnetic coupling in our models ensures close-to-rigid rotation during core hydrogen burning, this implies that all our LMC models above $\sim 80 M_\odot$ lose so much angular momentum that they cannot be considered to produce candidates for long-duration gamma-ray bursts. In that respect, models that undergo chemically homogeneous evolution of lower mass are better suited (cf. Sect. 3.3.4).

Effective temperatures and radii of observed massive stars may be affected by optically thick stellar winds, making the star appear larger and cooler. We use Eq. (14) from Langer (1989)

$$\tau(R) = \frac{\kappa |\dot{M}|}{4\pi R\,(v_\infty - v_0)} \ln \frac{v_\infty}{v_0} \tag{3.1}$$

to estimate the optical depth of the stellar winds of our stellar models. Here, R designates the radius of the stellar model without taking the wind into account. This equation is derived from a β-velocity law with $\beta = 1$. In this case, we use the electron scattering opacity ($\kappa = \sigma\,(1 + X)$, where σ is the Thomson scattering cross section), an expansion velocity $v_0 = 20\,\mathrm{km/s}$ at the surface of the stellar model, and a terminal wind velocity of $v_\infty = 2000\,\mathrm{km/s}$.

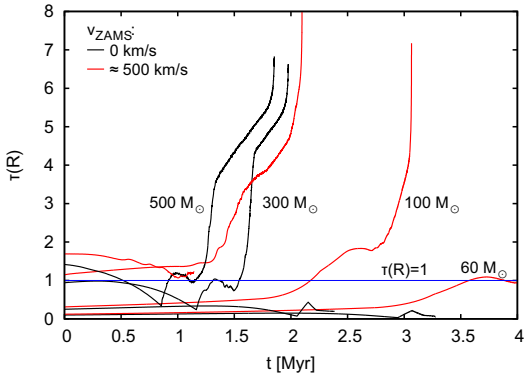

Figure 3.7.: Stellar wind optical depth according to Eq. (3.1), for some of our model sequences, shown as a function of time. We show eight stellar models with four different initial masses (60, 100, 300, 500 $M_\odot$), and two initial surface rotational velocities (0, 500 km/s) in black and red, respectively. The line for unit wind optical depth is plotted to facilitate the comparison.

Figure 3.7 shows the estimated optical depth of stellar winds as a function of time for several model sequences. The behaviour of the optical depths seen in the figure is mostly related to the change in the mass-loss rate. The optical depth increases for higher initial mass and higher rotation rate as a result of a corresponding increase in the mass-loss rate. While these numbers are only approximations, it shows that the winds of the most massive stars might already be optically thick ($\tau > 1$) on the zero-age main sequence, which implies that spectroscopically, these stars may already show Wolf-Rayet characteristics at this time (see also Gräfener & Hamann (2008a); Crowther et al. (2010)). Furthermore, while the stars of $100 M_\odot$ and below are expected to show optically thin winds for most of the core hydrogen burning evolution, the optical depths

of the winds for models for which a Wolf-Rayet type wind has been assumed may be quite large.

3.3.3. Surface abundance evolution

Deriving masses or ages of stars using stellar evolution tracks or isochrones in the HR diagram is no longer straightforward when rotational mixing is important. A given pair of effective temperature and luminosity can be explained by several combinations of masses, rotational velocities, and ages. To uniquely determine the initial parameters and the age of a star, it is necessary to include additional observables. The mass fractions or abundances of elements at the stellar surface are tracers of the rotational mixing. They can be used to uniquely identify the initial parameters and the age of a star in a three (or more) dimensional space of observables (cf. Köhler et al. (2012)). We therefore discuss the influence of time, initial rotational velocity and initial mass on the surface composition of our models.

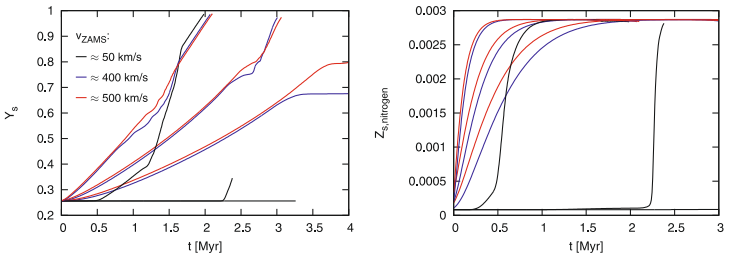

Figure 3.8.: Helium (left panel) and nitrogen (right panel) surface mass fraction as a function of time for models of 60, 100, and 300 $M_\odot$ and rotation rates explained in the figure key. While for the fast rotators the enhancements are mostly due to rotational mixing, for the slowly rotating models the increase in helium and nitrogen in the 100 $M_\odot$ and 300 $M_\odot$ mass models is solely due to mass loss.

The rotational mixing in our models is sensitive to the gradient of the mean molecular weight μ. Essentially, any significant μ-barrier prevents rotational mixing. Therefore, mixing of helium can only occur in our models as long as they are quasi-chemically homogeneous. This, in turn, requires the timescale for rotational mixing to be shorter than the nuclear timescale, as the star attempts to establish a μ-barrier on the nuclear timescale.

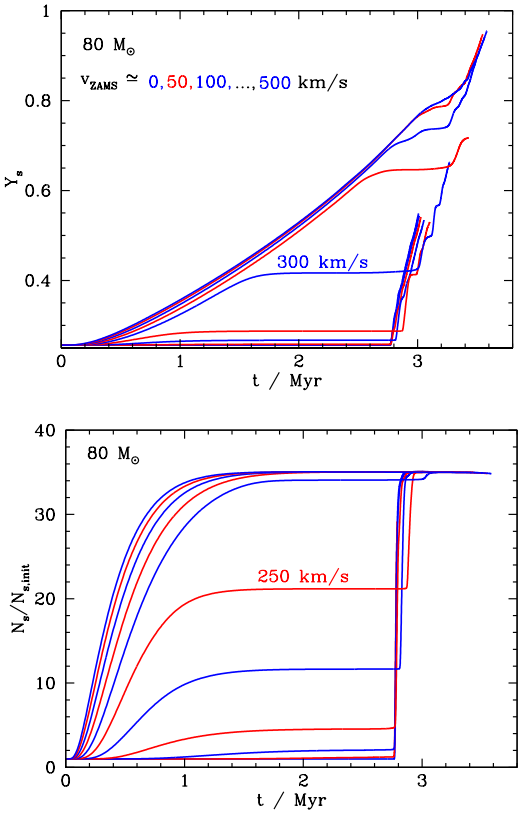

Figure 3.9.: Helium (upper panel) and nitrogen (lower panel) surface mass fraction as a function of time for models of 80 $M_\odot$ with approximate initial rotational velocities of 0, 50, 100, 150, 200, 250, 300, 350, 400, 450, and 500 km/s, during their core hydrogen burning evolution.

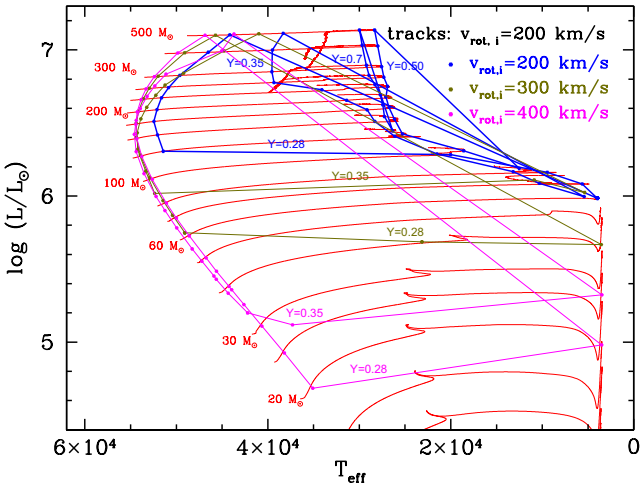

Figure 3.10.: Evolutionary tracks in the HR diagram of stellar models initially rotating with approximately 200 km/s, and with initial masses of 12, 15, 20, 25, 30, 40, 50, 60, 70, 80, 100, 125, 150, 175, 200, 230, 260, 300, 400, and 500$M_{\odot}$. Overlaid are lines (in blue) of constant helium surface mass fraction for Y=0.28, 0.35, 0.50, and 0.70. Lines of constant helium surface mass fraction for Y=0.28, 0.35 corresponding to models with approximate initial rotational velocities of 300 and 400 km/s are also shown.

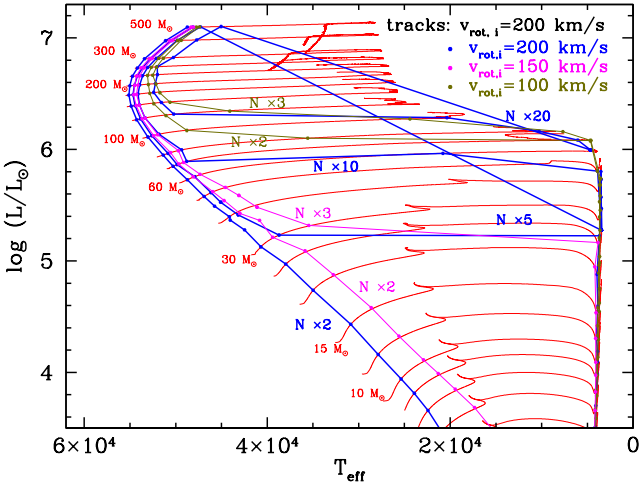

Figure 3.11.: Evolutionary tracks in the HR diagram of stellar models initially rotating with approximately 200 km/s, and with initial masses of 6, 7, 8, 9, 10, 12, 15, 20, 25, 30, 40, 50, 60, 70, 80, 100, 125, 150, 175, 200, 230, 260, 300, 400, and 500$M_{\odot}$. Overlaid are lines (in blue) of constant nitrogen surface mass fraction, corresponding to nitrogen enhancement factors of 2, 5, 10, and 20, as indicated in blue. Lines of constant nitrogen enhancement factors of 2 and 3 corresponding to models with approximate initial rotational velocities of 150 and 100 km/s are also shown.

In the fastest rotators, e.g. in the $100M_{\odot}$ and $300M_{\odot}$ models initially rotating with $\sim$ 400 and 500 km/s, the surface helium abundance goes almost all the way to $Y_{\rm s} = 1$ towards core hydrogen exhaustion (cf. Fig. 3.8). However, the same figure shows that this evolution is truncated for the rapidly rotating $60M_{\odot}$ models, at $Y_{\rm s} = 0.68$ and $Y_{\rm s} = 0.80$ for initial rotational velocities of $\sim$ 400 and 500 km/s, respectively. These models spin down during core hydrogen burning (Fig. 3.6) such that the timescale for rotational mixing eventually becomes larger than the nuclear timescale.

Figure 3.8 shows that the non-rotating $300M_{\odot}$ sequence also evolves to $Y_{\rm s} = 1$. The reason is the large convective core fraction of this model, and its large mass-loss rate. Whereas the model always keeps a small radiative envelope mass, the equivalent amount of mass is lost on a short timescale such that core and surface abundances become almost equal (cf. Sect. 3.3.4; Eq. 2). For the rapidly rotating $100M_{\odot}$ and $300M_{\odot}$ models, mass loss rather than rotational mixing must take over to enforce chemical homogeneity, since these models also spin down quite dramatically (Fig. 3.6).

Figure 3.9 (left panel) demonstrates the role of rotational mixing of helium in greater detail using the example of $80M_{\odot}$ sequences. In the models initially rotating with 0, 50, 100, 150, and 200 km/s, such mixing is essentially negligible, and only mass loss can increase the helium surface abundance close to core hydrogen exhaustion, which is why all of these models evolve along the same track in the HR-diagram (Fig. 3.3). The models between 250 and 400 km/s start out with chemically homogeneous evolution (though the one with $v_{\rm rot,i} = 250$ km/s only for a short amount of time), and truncate the homogeneous evolution later in time for higher initial rotation. The models which initially rotate with about 450 and 500 km/s undergo chemically homogeneous evolution all the way (though with the help of mass loss in the end), and their evolution in the HR diagram is also practically identical (Fig. 3.3).

The evolution of the surface nitrogen abundance in our models of rotating and mass losing stars follows different rules. During a phase of chemically homogeneous evolution, nitrogen is quickly mixed from the core to the surface establishing the CNO-equilibrium value in atmospheric layers (Figs. 3.8 and 3.9, left panels). Mass loss can also lead to nitrogen enhancements, even without rotational mixing (Fig. 3.8). Figure 3.9 shows that a strong nitrogen surface enhancement can be obtained even in models with initial rotational velocities well below the threshold value required for chemically homogeneous evolution. For example, the $80M_{\odot}$ models with $v_{\rm rot,i} = 150$ and 200 km/s enrich nitrogen at the stellar surface by factors of 4 and 12 by rotation, i.e. before mass loss kicks in. This order of magnitude of nitrogen enrichment is as expected, since our models were calibrated to increases the surface nitrogen abundance by a fac-

tor of about 3 for stars of 13–15$M_\odot$ for an initial rotational velocity of 150 km/s, and rotational mixing is stronger in more massive stars.

The reason is that nitrogen, carbon, and oxygen, with a maximum mass fraction of less than one per cent, are just trace elements, such that even significant internal gradients do not lead to strong μ-barriers. Therefore, at the beginning of core hydrogen burning, before significant amounts of hydrogen have been converted to helium, but after the CNO-cycle has already strongly enhanced the nitrogen abundance in the convective core, rotational mixing can bring nitrogen out of the core into the radiative envelope and later on also to the surface.

The surface enrichment of helium and nitrogen explained above allows a simple understanding of the occurrence of surface enrichments in the HR diagram. As shown in Fig. 3.10, stars initially rotating with rotational velocities of 200 km/s or less that are less luminous than $\log L/L_\odot \simeq 6.2$ are not expected to show any helium surface enrichment (i.e. $Y_s < 0.28$) as long as their surface temperature is higher than $\sim$ 20 000 K. The same is true for stars initially rotating slower than 300 km/s below $\log L/L_\odot \simeq 5.6$, and for those initially rotating slower than 400 km/s below $\log L/L_\odot \simeq 4.8$. Similar higher thresholds can be read off from Fig. 3.10 for larger surface helium mass fractions. Given that Ramírez-Agudelo et al. (2013) found that 75% of all O stars rotate slower than 200 km/s and that amongst the 31 O2 to O5 stars none was found to rotate faster than $\sim$ 300 km/s, the helium enrichment in LMC stars below $\sim 100 M_\odot$ is expected to be quite small during the main-sequence phase.

In contrast, as more than half of all O stars were found to rotate faster than 100 km/s, nitrogen enrichment by at least a factor of 2 is expected to be almost ubiquitous above $\log L/L_\odot \simeq 6.0$, and quite frequent in main-sequence O stars in general (Fig. 3.11).

Changes in the amount of neon, sodium, aluminum, and magnesium at the surface also occur, indicating that in very massive stars the MgAl- and the NeNa-cycles are active. In our models, the amount of magnesium is reduced while aluminum is produced. The mass fraction of neon increases in our models, while sodium decreases. For more details, we refer to the electronic data published with this paper.

Lithium, beryllium, and boron are destroyed in the stellar interior (McWilliam & Rauch 2004) at temperatures above $\sim 2.5 \cdot 10^6$ K for lithium, $\sim 3.5 \cdot 10^6$ K for beryllium, and $\sim 5.0 \cdot 10^6$ K for boron. In our models, temperatures below $5 \cdot 10^6$ K are only found in the outer envelope. Therefore lithium, beryllium, and boron can exist in the outer envelope, while they are destroyed in deeper layers. For the slowest rotating models, the surface abundances of these three elements remain constant until layers which were exposed to higher temperatures earlier in the evolution are exposed to the surface due to mass loss. When that happens, the mass fractions of beryllium, boron, and lithium

are quickly reduced. For fast rotating models, rotational mixing and mass loss lead to a gradual decrease in lithium, beryllium, and boron over time.

3.3.4. Chemically homogeneous evolution

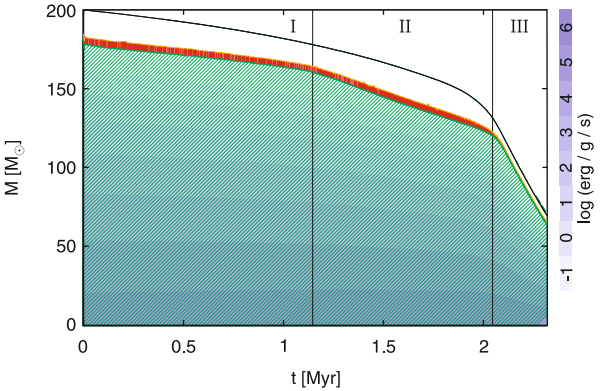

Figure 3.12.: Kippenhahn-diagram for our 200 $M_{\odot}$ model with $v_{\mathrm{ZAMS}} \simeq 300$ km/s. The black solid line gives the stellar mass as a function of time. Blue shading indicates thermonuclear energy generation (see colour bar to the right of the plot). Green hatched parts show convective regions, and convective core overshooting is indicated in red. Three different regimes can be distinguished according to the rate at which the mass of the convective core decreases (see text).

As mentioned in Sect. 3.3.1, we can divide our models into three classes. The first one (which we call Class O) likely corresponds to most stars in observed stellar samples and contains the models that evolve in the normal way, i.e. in which the rotationally induced mixing of helium is negligible. The second one describes the models that undergo quasi-chemically homogeneous evolution (Class H), which correspond to the initially fastest rotators. As the third class, we have the models that start out evolving homogeneously, but which spin down such that the rotational mixing of helium stops (Class HO), after which they evolve redward in the HR diagram as the ordinary models. These models retain a memory of their past homogeneous evolution, in that they will keep an enhanced helium surface abundance and a higher luminosity-to-mass ratio (Langer 1992) compared to ordinary stars throughout the rest of their core hydrogen burning evolution.

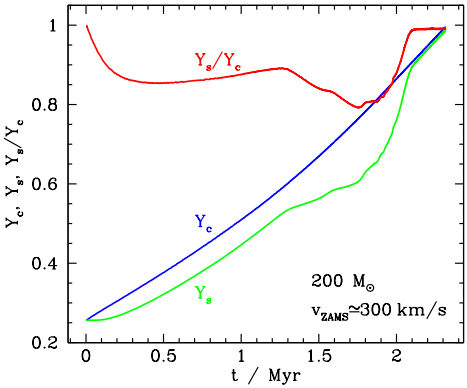

Figure 3.13.: Central Y_c and surface Y_s helium abundance of our 200 $M_\odot$ model with $v_{\rm ZAMS} \simeq 300$ km/s (cf. Fig. 3.12), and the ratio Y_s/Y_c as a function of time.

At the highest masses considered here ($M \gtrsim 150 M_\odot$), our models may also undergo quasi-chemically homogeneous evolution without rotationally induced mixing, which is due to a combination of an extremely high fraction of the convective core to the total stellar mass and a very high Wolf-Rayet type mass-loss rate. We illustrate this by the example of our 200 $M_\odot$ sequence with $v_{\rm ZAMS} \simeq 300$ km/s in Fig. 3.12. For such very massive stars, the convective core comprises a major fraction of the stellar mass.

We can divide the core hydrogen burning evolution of this model into three parts according to the mass evolution of the convective core. During the first part, the mass of the convective core decreases as a function of time, but more slowly than the mass of the star, such that the mass of the radiative envelope decreases and the convective core mass fraction increases. During this phase, the model undergoes quasi-chemically homogeneous evolution (cf. Fig. 3.13). At $t \simeq 1.2$ Myr, the model transitions to ordinary evolution, from which time on the convective core mass decreases somewhat faster than the total mass. During this second part of its evolution, the helium surface abundance increases, even though at a much lower rate than the central helium abundance (Fig. 3.13). Finally, in part three, the Wolf-Rayet mass loss kicks in, which leads to a very small mass of the non-convective stellar envelope ($M_{\rm env} \simeq 5 M_\odot$). The amount of mass corresponding to the non-convective envelope is lost (at a rate of $\sim 2\,10^{-4}\,M_\odot\,{\rm yr}^{-1}$) on a timescale of ~20 000 yr which corresponds to only about 1% of the core hydrogen burn-

ing time, $\tau_{\rm H}$. Consequently, the surface helium mass fraction during this stage is roughly equal to (within 1%) the central helium mass fraction. Thus, regardless of rotation, the model is extremely chemically homogeneous during this phase.

We define a fourth type of evolution (Type M) by

$$\frac{M_{\rm env}}{\dot{M}} < 0.1\tau_{\rm H}, \tag{3.2}$$

where $\tau_{\rm H}$ is the hydrogen burning timescale. Since this condition ensures that the surface-to-central helium abundance ratio is above ~ 0.9 — i.e. similar to or smaller than in the case of rotationally induced quasi-chemically homogeneous evolution — we can subdivide our models into further classes. For example, the $200\,M_\odot$ sequence discussed here can be considered of Class HOM, as it first undergoes chemically homogeneous evolution due to rotational mixing, then ordinarily, and finally chemically homogeneous evolution due to mass loss.

It is instructive to consider Fig. 3.14 to understand which evolutionary classes are realized by our models. The non-rotating sequences with initial masses of $300M_\odot$ and $500M_\odot$ achieve chemical homogeneity at a central helium mass fraction of 0.85 and 0.75, respectively, and thus belong to Class OM. The non-rotating $100M_\odot$ sequence does not reach homogeneity. Consequently, although it achieves a quite high final surface helium mass fraction of ~0.65, it belongs to Class O. The most rapidly rotating models depicted in Fig. 3.14 never show a significant discrepancy between their central and surface helium abundances, which implies that they evolve from H-type to M-type evolution and belong to Class HM. The stars rotating initially with ~ 300 km/s all undergo an H→O transition, where the two more massive ones move further on to Type M evolution. As stars in the Classes HOM and HM both start out and end their chemically homogeneous evolution, we will not distinguish them further and designate them both as Class HM.

Thus, we have five different classes of evolution, H, HM, HO, OM, and O, where all but the last involve quasi-chemically homogeneous evolution. Class O can be identified in Fig. 3.15 (right panel), which shows the close-to-final surface helium mass fraction for all our model sequences. Looking at the slowly rotating models, this figure shows that mass loss starts affecting the surface helium abundance above an initial mass of $\sim 65M_\odot$ ($\log M/M_\odot \simeq 1.8$), and that M-type chemically homogeneous evolution is obtained above $\sim 160M_\odot$ ($\log M/M_\odot \simeq 2.2$). According to our definition, the slow rotators below $\sim 160M_\odot$ are thus in Class O, the more massive ones in Class OM. For the fast rotators, the dividing line between homogeneous and inhomogeneous evolution depends on stellar mass. At $20M_\odot$ ($\log M/M_\odot \simeq 1.3$), stars rotating initially faster than

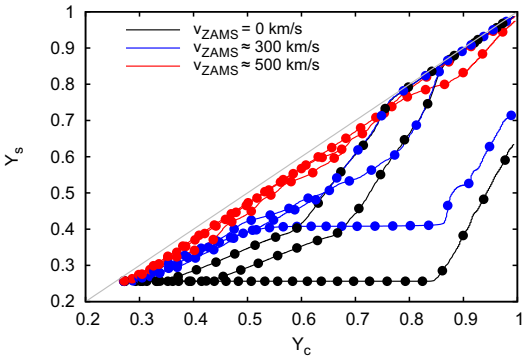

Figure 3.14.: The mass fraction of helium in the stellar core Y_c and at the surface Y_s are depicted for stellar models of 100, 300, and 500 $M_\odot$ and rotation rates explained in the figure key. For a given rotation rate, initially more massive stars increase their surface helium abundance more quickly. Every 10^5 yr the models are highlighted by filled circles. Chemically homogeneous evolution is indicated by equal changes in both mass fractions and corresponds to a slope unity. At $Y_c \geq 0.8$, all calculated stellar evolution models show an evolution toward the line of equal Y_c and Y_s, caused by mass loss.

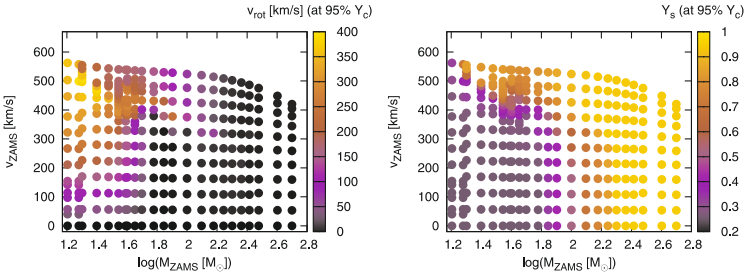

Figure 3.15.: The grid of all initial masses $M_{\rm ZAMS}$ and surface rotational velocities $v_{\rm ZAMS}$ is shown, including the stellar models with initial masses above 19 $M_\odot$ published in Brott et al. (2011a). The colour coding corresponds to the surface rotational velocity (left panel) and the helium mass fraction at the surface (right panel) at the time when the central helium mass fraction has reached 95%.

$\sim$ 500 km/s evolve homogeneously (Class H), while at $\sim$ 160$M_\odot$ the critical velocity is at $\sim$ 350 km/s, and more massive stars above this velocity are in Class HM. Below the dividing line defining Class H, between 20$M_\odot$ and 160$M_\odot$ is a stretch of Class HO models, which comprises a larger initial mass range for higher initial mass.

As mentioned in Sect. 3.3.1, rapidly rotating stellar models with initial masses greater than 125 $M_\odot$ show significantly different behaviour in the HR diagram (see Fig. 3.2) to the stellar models with $M \leq 125\,M_\odot$ (see also Sect. 3.3.6). Nevertheless, they behave in a similar way in the Kippenhahn diagram and when comparing the helium mass fraction in the core and at the surface.

Stellar evolution models above 80 $M_\odot$ have strong mass loss. Even the fastest rotators are slowed down significantly when the Hamann et al. (1995) mass-loss rate is applied. For models above $M_{\rm ZAMS} \simeq 100\,M_\odot$, the rotation rate at 95% helium mass fraction in the core is below 100 km/s. The surface rotational velocity goes down to less than 50 km/s for models above 150 $M_\odot$, independent of the initial surface rotational velocity (Fig. 3.15; right panel).

From the above, we can come to several conclusions which are relevant in comparison to observed stars. First, helium-enriched single stars below $\sim$ 65$M_\odot$ are prime suspects of H- or HO-type chemically homogeneous evolution, whereas M-type evolution can be excluded for them. These stars are expected to preserve their rapid rotation throughout their core hydrogen burning evolution. As a consequence, we may expect

some correlation of the helium surface abundance with the stellar rotation rate in the considered mass regime.

For very massive stars (above $\sim 200 M_\odot$) rotation, whether initially fast or not, makes little difference, i.e. the evolution becomes almost independent of the initial rotational velocity. These stars are efficiently spun down by mass loss, and all undergo chemically homogeneous evolution during their advanced hydrogen-burning evolution. Their surface helium abundance is always very close to their central helium abundance because of a rapid loss of the thin outer radiative envelope through mass loss. As a consequence, these sequences can produce models that have a very high surface helium mass fraction ($Y_s > 0.9$) and are still undergoing core-hydrogen burning.

3.3.5. Mass-luminosity relation

Stars of higher mass are increasingly luminous. The most massive models in our grids, at $500 M_\odot$, radiate at more than $10^7 L_\odot$. Figure 3.16 shows the evolution of selected non-rotating and of rapidly rotating model sequences in the mass-luminosity plane, from core hydrogen ignition to core hydrogen exhaustion. At the lowest considered masses ($15 M_\odot$), the models evolve vertically upward since their mass loss is negligible. The more massive, rapidly rotating models evolve to higher luminosity, and they turn left toward lower mass.

A comparison with the mass-luminosity relations for chemically homogeneous stars of Gräfener et al. (2011) reveals that, except for the depicted $15 M_\odot$ model, the rapidly rotating sequences shown in Fig. 3.16 undergo quasi-chemically homogeneous evolution. They start at the mass-luminosity (ML) relation for zero-age main sequence stars and finish close to the ML-relation for chemically homogeneous helium stars, indicating their nearly homogeneous chemical structure. This also demonstrates that the agreement of the ML-relations of Gräfener et al. (2011) (which represent fits to stellar models computed with a different code) with our models is very good.

We consider a mass-luminosity relation for chemically homogeneous stars as $L \sim M^\alpha \mu^\beta$, where μ is the mean molecular weight of the stellar gas. The power-law exponent α thus describes the slope of the ML-relation in the $\log M - \log L$-plane. According to Kippenhahn & Weigert (1990), we have $\alpha > 1$, and $\alpha \to 1$ for $M \to \infty$, due to the increasing radiation pressure for higher masses ($P_{\rm gas}/(P_{\rm gas} + P_{\rm rad}) \to 0$). The inequality $\alpha > 1$ implies that, in the frame of simple opacity laws, massive main sequence stars will never exceed the Eddington limit. The limit of $\alpha \to 1$ implies that for sufficiently massive stars, their hydrogen burning life time $\tau_H = E/\dot{E}$ becomes independent of mass, since their nuclear energy reservoir E is proportional to their mass, just as their energy

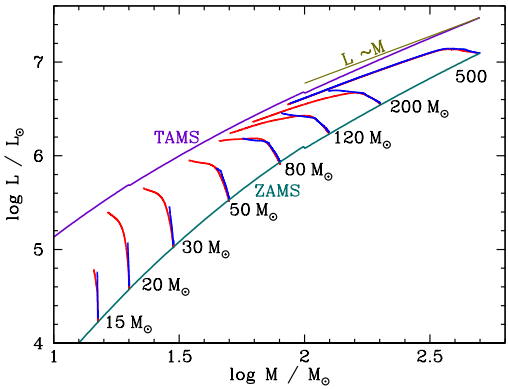

Figure 3.16.: Luminosity as a function of mass for selected non-rotating (blue) and rapidly rotating models ($v_{\rm rot,i}$ = 500 km/s; red). The labels indicate the initial mass of the considered sequences. The tracks end at a central helium mass fraction of Y_c = 0.98. Overplotted are the mass-luminosity relations of Gräfener et al. (2011) for chemically homogeneous stars with a hydrogen mass fraction of X=0.74 (labelled ZAMS) and X=0 (labelled TAMS). The straight line labelled "$L \sim M$" indicates the smallest expected slope of the mass-luminosity relation.

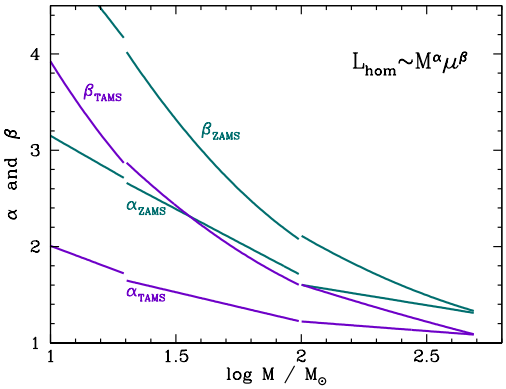

Figure 3.17.: Exponents of the mass-luminosity relation of the form $L \sim M^{\alpha}\mu^{\beta}$ for homogeneous stars from Gräfener et al. (2011), for a chemical composition corresponding to our zero-age main sequence models (labelled with the subscript ZAMS), and for pure helium stars of the corresponding metallicity (labelled with the subscript TAMS). Here, μ is the mean molecular weight of the stellar gas, which is computed as $1/\mu = 2X + 0.75Y + 0.5Z$, with X, Y, and Z being the hydrogen, helium, and metal mass fraction, and assuming complete ionization.

loss rate $\dot{E} = L$. Figure 3.16 shows that our most massive models reach α-values very close to one. We find the limiting stellar life time to be close to 1.9 Myr (cf. Table B1).

Figure 3.17 also shows that, at a given mass, the slope of the mass-luminosity relation is smaller for the homogeneous hydrogen-free stars, compared to that for the zero-age main sequence stars because the helium stars are much more luminous and thus more radiation pressure dominated. Furthermore, the power-law exponent β also approaches one for the highest considered masses. While a $15M_\odot$ helium star is about 20 times as luminous as a $15M_\odot$ zero-age main sequence star ($\bar{\beta}(15M_\odot) \simeq 3.7$, and $\mu_{\rm tams}/\mu_{\rm zams} \simeq 2.23$), the corresponding factor is only 2.4 at $500M_\odot$.

3.3.6. Near the Eddington limit

In its general form, the Eddington limit is complex as it involves an appropriate mean of the total of all opacity sources. This total opacity κ may be a function of depth in the stellar atmosphere; therefore, it is non-trivial to uniquely define the circumstances in which the star encounters its Eddington limit, nor to assess the consequences such an encounter may have. The proximity of a star of mass M and luminosity L to the Eddington limit is usually expressed in terms of the Eddington factor

$$\Gamma = \frac{\kappa L}{4\pi c G M} = \frac{\kappa \sigma T_{\rm eff}^4}{c g}, \tag{3.3}$$

where the constants have their usual meaning and $T_{\rm eff}$ is the effective temperature and g the surface gravity.

Considering only the dominant contributor to the opacity, i.e. photon scattering on free electrons, greatly simplifies the concept of Eddington limit as electron scattering is a grey process and, for the hot stars considered here, independent of depth in the atmosphere. For a star of mass M and luminosity L we obtain $\Gamma_{\rm e} = \kappa_{\rm e} L/(4\pi c G M)$, where $\kappa_{\rm e} = \sigma_{\rm e}(1 + X)$ is the opacity due to Thomson scattering. It holds that $\Gamma > \Gamma_{\rm e}$ as $\kappa > \kappa_{\rm e}$. Even in the most massive stars, the Eddington factor $\Gamma_{\rm e}$ will not exceed unity (see Sect. 3.3.5). Even so, since the mass-luminosity exponent $\alpha > 1$, main sequence stars will get ever closer to the Eddington limit for electron scattering the higher their mass.

Considering the true Eddington factor, we must expect that the situation $\Gamma = 1$ is actually achieved in very massive stars. Indeed, while $\kappa_e \simeq 0.34$ in our zero-age models, their true surface opacity is typically $\kappa_{\rm surface} \simeq 0.5$. We can thus expect that $\Gamma = 1$ is achieved at $\Gamma_e \simeq 0.7$.

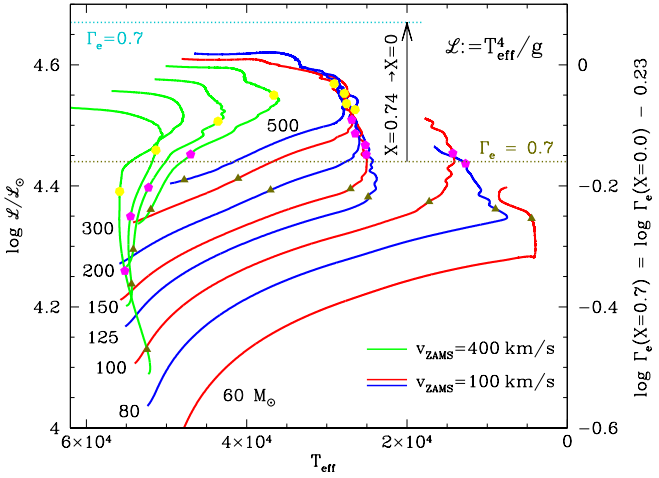

Figure 3.18.: The evolutionary tracks in the $\mathscr{D} - T_{\rm eff}$-diagram, where $\mathscr{D} = T_{\rm eff}^4/g$, for models initially rotating with 100 km/s (for 60, 80, 100, 125, 150, 200, 300, and $500 M_\odot$; alternating red and blue lines) and with 400 km/s (100, 150, 200, and $300 M_\odot$; green lines). The right y-axis shows the Eddington factor for electron scattering opacity Γ_e, which is proportional to $\mathscr{D}$, for a hydrogen mass fraction of $X = 0.74$. For $X = 0$, $\log \Gamma_e$ is larger by 0.23. Triangles, pentagons, and heptagons mark the locations where the surface helium mass fraction reaches 0.3, 0.5, and 0.7, respectively, for the presented evolutionary sequences. The dotted horizontal lines marks the value of $\Gamma_e = 0.7$ for $X = 0.74$ (green) and $X = 0$ (blue), approximately identifying the true Eddington limit that cannot be exceeded (see text).

In Fig. 3.18, we plot the quantity $\mathscr{L} := T_{\rm eff}^4/g = c/(\kappa_{\rm e}\sigma)\,\Gamma_{\rm e}$ as a function of the effective temperature of selected evolutionary sequences. We note that $\mathscr{L}$ is normalized to the solar value, $\log \mathscr{L}_\odot \simeq 10.61$ for convenience. For instance, for the initial composition of our stars we have $\log \mathscr{L}/\mathscr{L}_\odot \simeq 4.6 + \log \Gamma_{\rm e}$. The quantity $\mathscr{L}$ is proportional to $\Gamma_{\rm e}$ and can be derived from spectroscopic observation of stars without knowledge of their distance (cf. Langer & Kudritzki (2014)).

Since for stars of constant mass $\mathscr{L} \sim L$, the quantity $\mathscr{L}$ behaves in a similar way to the stellar luminosity, and the evolutionary tracks in the $\mathscr{L}$-$T_{\rm eff}$-diagram partly resemble those in the Hertzsprung-Russell diagram. However, unlike the latter, the $\mathscr{L}$-$T_{\rm eff}$-diagram has an impenetrable upper limit: the Eddington limit.

Comparing Fig. 3.18 with Fig. 3.2, we see that while the tracks of the slow rotators in Fig. 3.2 are almost horizontal, the corresponding tracks in Fig. 3.18 are significantly steeper. Their luminosities are nearly constant despite strong mass loss, because their increasing mean molecular weight μ compensates for their decreasing mass in the mass-luminosity relation (Sect. 3.3.5). While it remains hidden in Fig. 3.2, Fig. 3.18 reveals nicely that the mass loss drives these stars towards the Eddington limit. The same is true for the rapidly rotating stars; their tracks move steeply upward in both diagrams.

In Fig. 3.18, we have drawn the horizontal line indicating $\Gamma_{\rm e} = 0.7$ for our initial chemical composition — which corresponds to $\log \mathscr{L}/\mathscr{L}_\odot \simeq 4.445$. From the discussion above, we should expect that stellar models with unchanged surface composition should not be found above this line (as long as their hydrogen and helium can be considered fully ionized). This is confirmed by the triangles placed on the evolutionary tracks, indicating the position at which a surface helium mass fraction of $Y = 0.3$ is achieved, and which are all found below $\Gamma_{\rm e} = 0.7$. Similarly, even the models with the most helium-enriched surfaces stay below the upper horizontal line for $\Gamma_{\rm e}(X = 0) = 0.7$; in other words, the diagram shows that it is not the electron-scattering Eddington limit which constrains the evolution of the most massive stars, but the true Eddington limit. Furthermore, Fig. 3.18 indicates that the limiting electron-scattering Eddington factor — which can be read off from Fig. 3.18 to be a little bit below $\Gamma_e = 0.7$ — is independent of the hydrogen/helium surface abundances.

We find our models near the Eddington limit to undergo a significant envelope inflation. This phenomenon has been described before by Kato (1986) and Ishii et al. (1999) for zero-age main sequence stars of different metallicities, and by Ishii et al. (1999); Petrovic et al. (2006); Gräfener et al. (2012) for Wolf-Rayet stars. Figure 3.19 shows the location of our zero-age main sequence stars, and of zero-age helium stars with the same metallicity, in the HR-diagram. Both curves show a maximum effective temperature, which is reached at about $30 M_\odot$ (140 000 K) for the helium stars, and at $200 M_\odot$

(54 000 K) for the hydrogen-rich stars. Above these masses, the effective temperature decreases again owing to the envelope inflation.

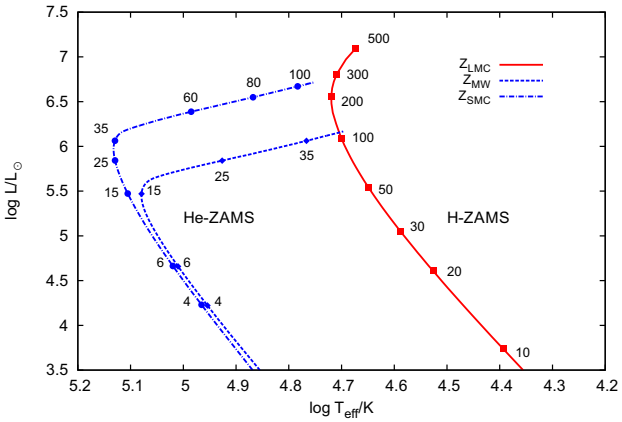

Figure 3.19.: The zero-age main sequence of our non-rotating stellar models in the indicated mass range (solid red line), compared with zero-age main sequences helium star models for Milky Way (dashed blue line) and SMC (dash-dotted blue line) composition. Labelled dots along the lines imply masses in solar units. Owing to envelope inflation the helium main sequences bend towards cooler temperatures close to the Eddington limit.

As seen in Fig. 3.19, the line describing the helium stars bends sharply to cooler temperatures at about $1\,000\,000 L_{\odot}$, and is even expected to cross the hydrogen-ZAMS (see also Ishii et al. (1999)), implying that more luminous helium stars are cooler than equally bright zero-age main sequence stars. This has the consequence that stars undergoing chemically homogeneous evolution above $\sim 125 M_{\odot}$ evolve to cooler surface temperature (see Fig. 3.2).

The envelope inflation occurs because layers inside the stellar envelope reach or exceed the true Eddington limit. The inflation begins before the critical value of $\Gamma_e \simeq 0.7$ is reached, i.e. the electron-scattering Eddington factors are only $\Gamma_e \simeq 0.31$ and $\Gamma_e \simeq 0.41$ for the $15 M_{\odot}$ helium star and $190 M_{\odot}$ zero-age main sequence star, respectively, because of the opacity peaks of iron and helium which can reach values of $1\,\mathrm{cm}^2/\mathrm{g}$ or more.

While the subsurface layers with such opacities always turn convectively unstable, convection, according to the mixing-length theory, is mostly very inefficient in transporting energy in these layers. Consequently, the high radiation pressure pushes the overlying layers outwards, until the opacity drops such that the true Eddington factor falls short of $\Gamma = 1$.

Many of these models also develop density inversions near the layer with the maximum Eddington factor (Joss et al. 1973). The corresponding inward directed gas pressure gradient then allows the star to retain layers whose Eddington factor exceed the critical value of $\Gamma = 1$. While the stability of these structures remains to be investigated, any instability which would tend to iron out the density inversion will likely lead to a further inflation of the overlying layers. A further degree of complexity is added by the fact that we find many models close to the Eddington limit to be unstable at least to radial pulsations (the only pulsation mode which we can see with our one-dimensional hydrodynamic stellar evolution code), and that convective velocities close to the sound speed may imply significant acoustic fluxes (Goldreich & Kumar 1990). A deeper investigation of these phenomena exceeds the scope of the present paper and will be pursued elsewhere.

3.4. Comparison with previous results

Recently, Yusof et al. (2013) published a grid of stellar evolution models for very massive stars. Eight of their evolutionary sequences were modelled using a similar initial composition to the one we used here, except that Yusof et al. used a scaled solar metal mix, while we take the measured LMC composition where possible (cf. Brott et al. (2011a)). Yusof et al. present non-rotating models with initial masses of $120 M_\odot$, $150 M_\odot$, and $500 M_\odot$ as well as rotating models at $120 M_\odot$, $150 M_\odot$, $200 M_\odot$, $300 M_\odot$, and $500 M_\odot$. The rotating models of Yusof et al. had initial rotational velocities of 400 km/s or more (cf. their Table 2).

3.4.1. Subsurface convection and envelope inflation

A major difference between the models of Yusof et al. and our models occurs because of the different treatment of convection in the stellar envelopes. Starting at zero age, all our models contain subsurface convection zones which occur because of the opacity peaks of iron and helium (cf. Cantiello et al. (2009)). When using the standard mixing-length theory, where the mixing length is assumed to be proportional to the pressure scale height, we find the convective energy transport in these zones to be mostly inef-

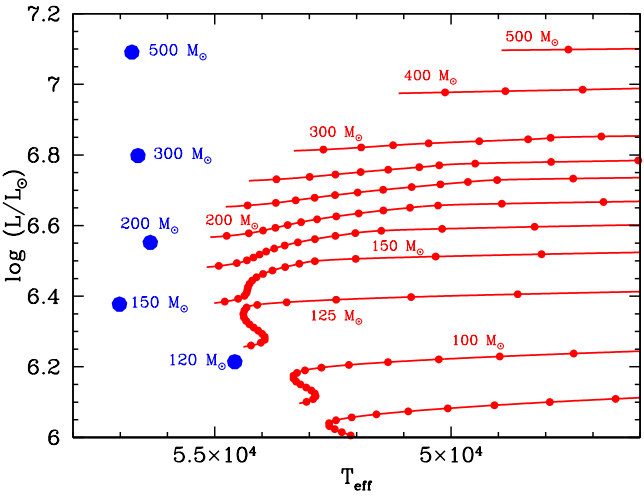

Figure 3.20.: Comparison of the ZAMS position of the models from Yusof et al. (2013) which include rotation (blue dots) with our tracks for $v_{\rm rot,i} \simeq 300$ km/s (red lines) in the HR diagram. We show tracks with initial masses of $80M_{\odot}$, $100M_{\odot}$, $125M_{\odot}$, $150M_{\odot}$, $175M_{\odot}$, $200M_{\odot}$, $230M_{\odot}$, $260M_{\odot}$, $300M_{\odot}$, $400M_{\odot}$, and $500M_{\odot}$. The time interval between two dots on the tracks corresponds to 10^5 yr.

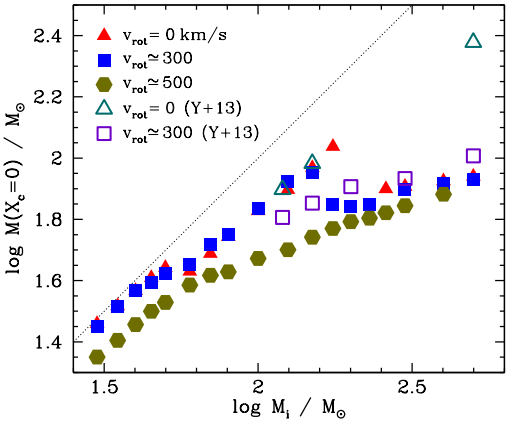

Figure 3.21.: Stellar mass at the end of core hydrogen burning versus initial mass for our sequences with initial rotational velocities of $v_{\rm rot,i} \simeq 0$ km/s, 300 km/s, and 500 km/s (filled symbols). The open symbols correspond to the LMC models of Yusof et al. (2013) with and without rotation. The dotted straight line corresponds to the location where the stellar mass at the end of core hydrogen burning equals the initial mass, i.e. to negligible mass loss.

ficient because of the small local thermal timescales imposed by the low densities. As a consequence, we obtain a rich envelope phenomenology as described in Sect. 3.3.6, including envelope inflation and density inversions.

Yusof et al. describe this situation as unphysical, and avoid it by assuming the convective mixing length to be proportional to the density scale height. As a consequence, when the star attempts to establish a density inversion, the density scale height tends to infinity, which imposes the convective energy transport to be extremely efficient, and opacity peaks will have few consequences. While the existence of inflated envelopes in nature remains to be shown (cf. Gräfener et al. (2012); Gräfener & Vink (2013)), we consider it likely, since the short thermal timescales of the envelopes of very massive stars cannot be in accordance with efficient convective energy transport. While this will surely be studied in more detail in the near future, we restrict ourselves here to pointing out the consequences of the different assumptions on the convective efficiency.

Strong differences between the models of Yusof et al. and our models already occur at the zero-age main sequence. As described in Sect. 3.3.1, our zero-age models (with our metallicity of $Z = 0.0047$) reach a maximum effective temperature of about 56 000 K at $\sim 190 M_{\odot}$, which agrees very well with the results of Ishii et al. (1999) for $Z = 0.004$. In Fig. 3.20, we compare the location of the rotating zero-age models of Yusof et al. (according to their Table 2) with the early hydrogen burning evolution of our models with an initial rotational velocity of ~ 300 km/s. Above $\sim 120 M_{\odot}$, the models of Yusof et al. are hotter than ours, and the more so the larger the mass.

This discrepancy is likely explained by the difference in the treatment of the envelope convection, since our treatment yields a larger radius inflation the closer the star is to its Eddington limit (Sect. 3.3.6). At a given initial mass, the discrepancy between the models of Yusof et al. and our models is therefore expected to increase with time at least initially, since the models increase their luminosity and decrease their mass (cf. Fig. 3.16), and thus their Eddington factors grow. The biggest consequence of this is that — although we use a very similar mass-loss prescription to that of Yusof et al. — our mass-loss rates are higher because our stars have cooler surfaces.

3.4.2. M_{ZAMS} versus M_{TAMS} relation

Figure 3.21 shows that as a result of the different treatment of envelope convection in our models and those of Yusof et al., our non-rotating models above $\sim 150 M_{\odot}$ undergo a dramatic mass loss during core hydrogen burning, leading to masses at core hydrogen exhaustion of the order of $80 M_{\odot}$ even up to the highest initial mass of $500 M_{\odot}$. Yusof et al. did not consider non-rotating models between $150 M_{\odot}$ and $500 M_{\odot}$. However,

their non-rotating models below $150 M_\odot$ and at $500 M_\odot$ remain close to the diagonal in Fig. 3.21. While our $500 M_\odot$ model ends hydrogen burning with a mass of $87 M_\odot$, theirs does so with $239 M_\odot$. We discuss the consequences for the final fate of the stars in Sect. 3.4. Remarkably, because of the low mass-luminosity exponent of the most massive stars considered here, the core hydrogen burning life time of the $500 M_\odot$ sequence of Yusof et al. (1.9 Myr) resembles ours, indicating that the life time of the most massive stars is not strongly affected by the differences discussed above.

The non-rotating $500 M_\odot$ sequence of Yusof et al. ends core hydrogen burning as a nearly chemically homogeneous helium star with a surface helium mass fraction of 0.97. Our Fig. 3.19 above shows that at the considered metallicity, our helium star models start to have inflated envelopes above $\sim 30 M_\odot$ (see also Ishii et al. (1999), and Petrovic et al. (2006)), and that a $239 M_\odot$ helium star model would be so enormously inflated that it would appear as a red supergiant, if a stable envelope structure existed at all. This demonstrates that while the envelope physics used in our models leads to pushing the outer layers of stars at the Eddington limit to large radii, this seems to occur to a much lesser degree in the models of Yusof et al., with the consequence of a smaller mass-loss rate.

When looking at the Eddington factor for electron scattering Γ_e, the models of Yusof et al. behave as our models do, i.e. they remain mostly lower than $\Gamma_e = 0.7$ (cf. Sect. 3.3.6). However, their non-rotating $500 M_\odot$ sequence is an exception, where $\Gamma_e = 0.82$ is reached at core hydrogen exhaustion. In comparison to the stellar wind calculations of Vink et al. (2011a), who found a strong mass-loss enhancement for stars above $\Gamma_e = 0.7$, we would again expect that the mass at core hydrogen exhaustion of this sequence could be considerably lower than that found by Yusof et al.

Our models show the largest mass-loss rates during their Wolf-Rayet phase (cf. Sect. 3.2). Nevertheless, it is not the choice of the Wolf-Rayet mass-loss prescription which makes our non-rotating models lose more mass than the comparable models of Yusof et al. We find, for example, that for our slowly rotating $500 M_\odot$ models at the time of the maximum mass-loss rate, the prescription by Nugis & Lamers (2000) leads to a mass-loss rate for our stars which is two times larger than the one we use. We conclude that the high pre-Wolf-Rayet mass loss imposed by the inflated envelopes of our models plays a crucial role in explaining the smaller TAMS-mass of our very massive slow rotators compared to those of Yusof et al.

3.4.3. Rotational mixing of helium

Another difference between the models of Yusof et al. and our models concerns the rotational mixing of helium. As shown in Sect. 3.3.3, the mixing of helium in our models is practically absent below a threshold rotational velocity, and nearly complete above the threshold. The mixed models suffer more mass loss since they become Wolf-Rayet stars earlier. As the threshold velocity decreases for higher masses, this results in a bimodal behaviour of the total mass lost during core hydrogen burning (Fig. 3.21). Our models with an initial rotational velocity of ~ 300 km/s follow the non-rotating models below $\sim 150 M_{\odot}$, while they behave in a similar way to our fastest rotators for higher mass. In the models of Yusof et al., the mixing of helium is gradually increased for larger rotational velocities. Therefore, their rotating models end core hydrogen burning with masses that exceed those of our homogeneously evolving models.

A more detailed comparison with the models of Yusof et al. is difficult because they considered only two rotational velocities, i.e. $v_{\rm rot,i} = 0$ km/s and $v_{\rm rot,i} \simeq 400$ km/s. This may also prevent a clear discrimination of their models from ours through observations, since Ramírez-Agudelo et al. (2013) showed that only very few O stars are expected with $v_{\rm rot,i} = 0$ km/s and $v_{\rm rot,i} \simeq 400$ km/s, while the majority rotate with $v_{\rm rot,i} = 100 \ldots 200$ km/s.

3.5. Summary

We present a detailed grid of stellar evolution models for single stars with initial masses from 70 to 500 $M_{\odot}$ and rotation rates up to 550 km/s. We used the same physics and assumptions as Brott et al. (2011a) did for stars in the mass range 5-60$M_{\odot}$, and this new grid therefore is an extension of their work. The initial composition of our models corresponds to abundance measurements for massive stars in the Large Magellanic Cloud. We follow the evolution of the stellar models through their core hydrogen burning phase, with some of them computed well beyond this stage.

Given the high fraction of close binaries in massive stars (Sana et al. 2012), we cannot hope to obtain a complete picture of massive star evolution from our models (de Mink et al. 2014), which is true in particular for the most massive stars (Schneider et al. 2014a). On the other hand, our rotating models may constitute a fair approximation for those mass gainers and mergers in close binaries which rejuvenate after the binary interaction (Braun & Langer 1995), even though their age, their detailed surface abundances, and their spin may still be peculiar (de Mink et al. 2013). In addition, since most mass donors in post-interaction close binaries either remain unobserved (de Mink et al. 2014) or show extreme surface enrichments (Langer 2012), and as Sana et al. (2012, 2013a)

suggest that 30-50% of the massive stars in 30 Dor appear not to have a close companion, a comparison of our single-star models with observed very massive stars will still be meaningful.

We find that stellar rotation can influence the evolution of our models significantly, mostly through mixing of helium. We find two threshold initial rotational velocities, which both decrease with increasing initial mass, one below which the rotational mixing of helium is negligible, and a second one above which the models undergo quasi-chemically homogeneous evolution. For initial rotational velocities in between the threshold values, the models start chemically homogeneously and develop helium-enriched surfaces, but transit to normal evolution as a result of spin-down.

Above an initial mass of $\sim 160 M_{\odot}$, we find that quasi-chemically homogeneous evolution can also be achieved through mass loss, which in fact ensures that all our more massive models end core-hydrogen burning as nearly pure helium stars, independent of their initial rotation rate. We find that single stars with initial rotational velocities below 300 km/s need to be more massive than $\sim 100 M_{\odot}$ in order to achieve a surface helium mass fraction above 35% (cf. Fig. 3.10).

Significant mixing of trace elements, including nitrogen and boron, is found well below the threshold velocities mentioned above. Because of the high core temperatures in our very massive models, the NeNa- and MgAl-cycles are also activated and lead to surface abundance changes of the involved isotopes. A tripling of the surface nitrogen abundance occurs in our models above an initial rotational velocity of 150 km/s and a mass of $\sim 25 M_{\odot}$, while a doubling at this rotation rate occurs even down to $6 M_{\odot}$ (Fig. 3.11). Because of the strong mass loss and large convective core masses, the surfaces of our models above $\sim 100 M_{\odot}$ become nitrogen-rich irrespective of their rotation rate.

Our zero-age models above $\sim 150 M_{\odot}$, as well as more evolved models down to $\sim 40 M_{\odot}$ show significant envelope inflation because the true Eddington factor inside the stellar envelope approaches or even exceeds the value of unity, while the electron-scattering Eddington factor remains below or near a value of $\Gamma_e = 0.7$ (cf. Sect. 3.3.6). Consequently, our zero-age main sequence models show a maximum surface temperature of 56 000 K at about $180 M_{\odot}$, with lower values for higher masses (Fig. 3.2).

During core hydrogen burning, the envelope inflation drives our slow rotators in the mass range $50 - 100 M_{\odot}$ to effective temperatures near or below 10 000 K. At these cool temperatures, partial hydrogen recombination leads to high opacities, which in turn produces true Eddington factors well above one in the envelopes of these models. While a detailed study of this phenomenon remains to be done, we speculate that this feature is related to the outbursts of luminous blue variables.

The inflation and the corresponding decrease of the surface temperature lead to enhanced mass loss compared to the models of Yusof et al. (2013). The enhanced mass loss has strong consequences for the final fate of very massive stars. In this context it is important to emphasize the metallicity dependence of inflation (Ishii et al. 1999). The reduced masses (Fig. 3.21) exclude very massive stars of the considered metallicity as progenitors of pair-instability supernovae. This is in agreement with Langer et al. (2007), who demonstrated that models with the same envelope physics as used here may produce pair instability supernovae at a metallicity of $Z_{\odot}/20$ (Kozyreva et al. 2014). This is in contrast to the finding of Yusof et al., who suggest that slow rotators above $\sim 300 M_{\odot}$ end up with CO-cores above $60 M_{\odot}$ at a metallicity of that of the LMC.

A further consequence of the strong mass loss of our inflated models is their distinct spin-down during core hydrogen burning (Fig. 3.6). This prevents all our models above $\sim 60 M_{\odot}$ from producing a long-duration gamma-ray burst upon collapse. From the models considered here and including those from Brott et al. (2011a), the highest chance to produce long-duration gamma-ray burst at LMC metallicity from the chemically homogeneous evolution scenario (Yoon & Langer 2005; Woosley & Heger 2006) may occur in the mass range $20 - 30 M_{\odot}$ (Langer 2012).

The VLT-FLAMES Tarantula Survey (Evans et al. 2011) provides one of the major motivations for this study. Our models will be extensively compared with these and other observations in the near future. To this end, we provide the main outputs of our stellar evolution models as electronic tables (stored at CDS) in the same format as those of Brott et al. (2011a). Additionally, we provide sets of isochrones in Appendix A.1.1.

Acknowledgements: We want to thank Durand D'Souza for fruitful discussions, and Jesús Maíz Apellániz, Matteo Cantiello, Joachim Puls, Jon Sundqvist and Paco Najarro for useful comments. SdM acknowledges support for this work by NASA through an Einstein Fellowship grant, PF3-140105. We are grateful to the referee for improving this paper.

4. Simulating populations of very massive rotating stars in the Large Magellanic Cloud (LMC)

4.1. Introduction

O-type stars are exceedingly interesting objects. They drive the chemical and dynamical evolution of galaxies by enriching the interstellar medium with heavy elements, by creating HII regions and by exploding as supernovae. The evolution of massive stars is strongly influenced by the physics of mass loss, rotational mixing, core overshooting and binary interaction.

Although stellar evolution models are very useful to compare to observations, simulated populations of stars based on stellar models additionally give information about the probability to observe stars at certain stages of evolution depending on the distribution functions of initial mass and initial surface rotational velocity and the star formation history applied. Several stellar evolution models for very massive stars are published, but only a few papers contain stellar models occupying the right mass range and metallicity taking into account rotation to compare to the data of the VLT-Flames Tarantula survey (VFTS). Usable stellar evolution tracks are presented in Crowther et al. (2010); Yusof et al. (2013); Köhler et al. (2015).

The stellar evolution models of Crowther et al. (2010); Yusof et al. (2013) cover the mass range and the metallicity of the massive stars in the VFTS, but unfortunately the models are only provided for two different surface rotational velocities. These models are not suitable to compute population synthesis models for a given distribution of surface rotational velocities. Therefore the populations presented in this chapter are based on the stellar evolution models published in Köhler et al. (2015), which have a dense spacing in initial rotation rates with steps of 50 km/s. Based on these models, several population synthesis models are computed to study the effect of the star formation history on the population of the very massive stars for distributions of initial mass and initial surface rotation rate tailored to the VFTS sample. To compute the populations, we use the method of Brott et al. (2011b) but taking into account stellar evolution models up to 500 $M_{\odot}$.

In Section 4.2 we describe the method to simulate populations of very massive stars, as well as the used initial distribution functions of mass and surface rotational veloc-

ity and stellar models. The results of the population synthesis calculations assuming starbursts of different ages are presented in Section 3 and the results for continuous star formation are given in Section 4. The results are discussed in Section 5 and final conclusions are given in Section 6.

4.2. Simulating a population of very massive stars

4.2.1. Population synthesis code Starmaker

Starmaker is a population synthesis code, which is based on detailed stellar evolution models of rotating stars (Brott et al. 2011b). Distribution functions of the initial mass, the initial surface rotational velocity and the star formation history are used as input, while a random distribution of stellar rotation axes is assumed. The underlying stellar evolution models have been calculated for fixed initial masses and rotation rates, so that an interpolation is needed for stellar parameters (mass and surface rotational velocity) that are not covered by the stellar evolution models.

For the interpolation, five points of interest (POIS) are defined for each stellar evolution track. These points are boundaries between different evolutionary phases of the stellar models to assure that interpolation will only be done within the same evolutionary phase.

- POI 1: ZAMS,
- POI 2: overall contraction phase near the end of the main sequence ($M_{\rm ZAMS}$ <50 $\rm M_{\odot}$),
- POI 2b: first blue-ward evolution in the HR diagram at low effective temperatures near the Eddington limit (before the end of the main sequence, $M_{\rm ZAMS}$ >50 $\rm M_{\odot}$),
- POI 3: the exhaustion of hydrogen in the core,
- POI 4: the end of thick hydrogen shell burning and
- POI 5: the ignition of helium in the core.

Figure 4.1 shows two stellar evolution models together with the corresponding POIS in the HR diagram. As the underlying stellar evolution models of the very massive stars are limited to the main sequence phase, the population synthesis calculations presented in this chapter focus on the main sequence evolution. Therefore POI 1 to POI 3 are used. If the stellar evolution models have not been calculated until hydrogen exhaustion, POI 3 is extrapolated linearly from the increase of helium abundance in the core. POIS

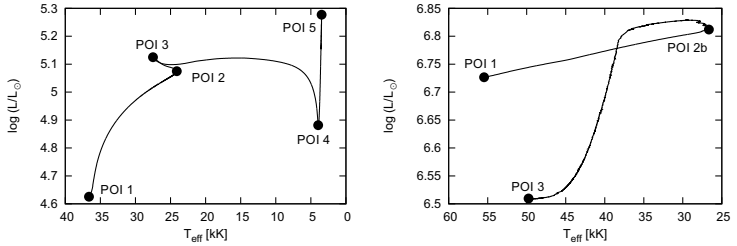

Figure 4.1.: The Hertzsprung Russel (HR) diagrams of the non-rotating 20 $M_\odot$ stellar model from Brott et al. (2011a) to the left and the non-rotating 260 $M_\odot$ stellar model from Köhler et al. (2015) to the right. The defined points of interest (POI), corresponding to boundaries of different evolutionary phases, are show in both cases.

for each drawn star are derived as explained in Brott et al. (2011b). Additionally, POI 2b is introduced to cope with the very massive stars which reach the Eddington limit before the end of the main sequence, leading to a blue-ward evolution in the HR diagram as shown in the right panel of Figure 4.1.

For each star of the simulated population with drawn values of mass and surface rotational velocity, the four nearest neighbours in a two dimensional grid of ZAMS mass and ZAMS rotational velocity are chosen. The interpolation is then done as a function of the fractional age between two POIS and therefore only within the same evolutionary phase. The three-dimensional interpolation works as follows. First, we interpolate linearly in mass between the closest stellar models. Second, we interpolate linearly in rotation rate.

The population synthesis code Starmaker produces among others the following output: age, effective temperature, luminosity, radius, surface gravity, mass loss rate, surface rotational velocity, mass and surface abundances of helium, boron, carbon, nitrogen, oxygen, neon, sodium and silicon.

4.2.2. Grid of stellar evolution models

The population synthesis calculations are based on massive rotating stellar evolution models of Brott et al. (2011a) and Köhler et al. (2015) for LMC metallicity. In total, the grid contains models in a mass range from 2 to 500 $M_\odot$. For simulating O-type stars, stellar evolution models are used starting at 15 $M_\odot$. The population synthesis calculations for stars up to 60 $M_\odot$ are performed as in Brott et al. (2011b) .

Initial surface rotational velocities up to 550 km/s are available for each initial mass to account for the effect of rotation on the evolution of massive and very massive stars. Rotational mixing significantly affects the enrichment of rapidly rotating stellar models above 20 $M_\odot$ and leads to partially-chemically homogeneous evolution of fast rotators and quasi-chemically homogeneous evolution of the rapid rotators as discussed in Brott et al. (2011a); Köhler et al. (2015).

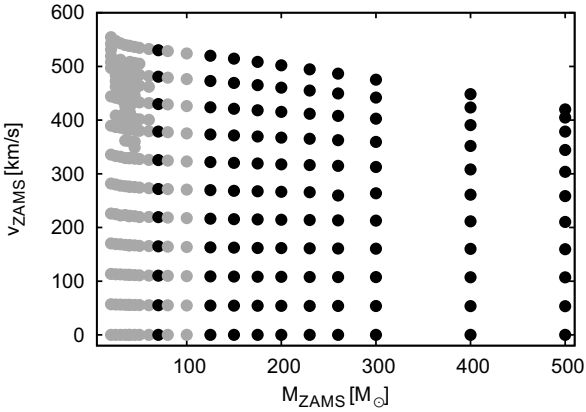

Figure 4.2.: Summary of stellar evolution models used in the population synthesis calculations. Each symbol in the grid corresponds to a stellar model with mass $M_{\rm ZAMS}$ and surface rotational velocity $v_{\rm ZAMS}$ at the ZAMS, that has been calculated until or near hydrogen exhaustion in the core. Grey dots indicate stellar models calculated by I. Brott and partly published in Brott et al. (2011a), while black dots point out models published in Köhler et al. (2015).

Figure 4.2 summarizes all available stellar evolution models in the $M_{\rm ZAMS} - v_{\rm ZAMS}$ plane. The different colours indicate whether these models are calculated and published in Brott et al. (2011a); Köhler et al. (2015) .

4.2.3. Initial mass distribution

We use the Salpeter initial mass function (IMF) for the distribution of initial masses (Salpeter 1955)

$$\mathrm{d}N \propto M^{\gamma}\mathrm{d}M, \tag{4.1}$$

giving the probability N for a a star to enter the main sequence with initial mass M and IMF slope γ.

Although the observed mass distribution for the very massive stars might differ from the applied IMF, several authors favour the idea of an overall Salpeter-IMF (Schweizer 2004; Selman & Melnick 2005; Selman et al. 2011). Selman & Melnick (2005) mention that differences above $40\,M_\odot$ are likely to occur due to selective incompleteness of the samples and support a universal Salpeter-IMF. For stars in 30 Dor an IMF slope of $\gamma = -2.35$ is supported by observation (Brandl et al. 1996; Massey & Hunter 1998; Massey 2003).

4.2.4. Distribution of inclination angles

We assume that stellar rotation axes are distributed equally in space. The inclination angle of a star is given as the angle between the line of sight and its rotational axis. An inclination angle of 0° corresponds to stars being observed pole-on, while 90° corresponds to to stars being observed equator-on. When assuming randomly distributed orientations, higher inclination angles are favoured. Two configurations exists to observe a stars pole-on with the rotational axis and the line of sight in the same direction, but there are several possibilities for a star to be seen equator-on with every possible rotational axis lying in the plane orthogonal to the line of sight.

The probability density function of the inclination angle i is given by $\mathrm{d}p/\mathrm{d}i = \sin(i)$, corresponding to a flat distribution in $\cos(i)$ with $\mathrm{d}p/\mathrm{d}\cos(i) = \mathrm{const}$,

$$\frac{\mathrm{d}p}{\mathrm{d}\sin(i)} = \frac{\mathrm{d}p}{\cos(i)\mathrm{d}i} = \frac{\sin(i)}{\cos(i)}. \tag{4.2}$$

Therefore within the population synthesis code Starmaker, the distribution of $\sin(i)$ is generated assuming a uniform distribution of $\cos(i)$.

4.2.5. Distribution of initial rotational velocities

We have an interest in producing population synthesis calculations to compare to the sample of O-type stars observed within the VFTS. Unfortunately, the complete O-star sample is not suitable for studying the very massive stars from the point of statistics, because it is dominated by stars of type O9. Stars of spectral type O8 and O9 are exclude them from the sample but it would be reasonable to investigate them separately in a subsequent study outside the scope of this thesis.

We are interested in the surface rotational velocity distribution of main-sequence stars with spectral class O2 to O7. O. Ramírez-Agudelo provided the distribution of

projected surface rotational velocities derived from a sub-sample (only main-sequence stars of spectral type O2 – O7) of single O-type stars within the VFTS (complete sample published in Ramírez-Agudelo et al. (2013)). P. Dufton derived the probability density function of the surface rotational velocities $P(v_{\rm rot})$ shown in Figure 4.3, assuming randomly oriented stellar spin axes as explained for B-type stars in Dufton et al. (2013)).

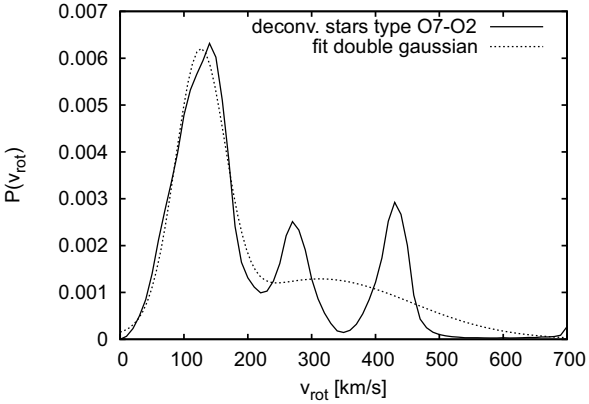

Figure 4.3.: Probability density function $P(v_{\rm rot})$ of the equatorial surface rotational velocity $v_{\rm rot}$ for VFTS stars of spectral type O7 to O2 is shown (black solid line), provided by P. Dufton. The sum of two Gaussian functions is used to fit the observed probability density function which is depicted in this figure by a dotted line.

This probability density function is characterized by a low velocity peak and a high velocity tail showing two strong peaks. Ramírez-Agudelo et al. (2013) find the low velocity peak consistent with other studies of late O-type stars and the high velocity tail being related to post-interacting binaries due to the agreement with population synthesis computations studying binary evolution (de Mink et al. 2013). The strong peaks in the high velocity tail might result from the low number of stars. Therefore it is reasonable to fit the probability density function by the sum of two Gaussian functions. The mean values, standard deviations and scaling factors of both derived Gaussian functions ($v_{\rm rot}$-distribution) of our sample are summarized in Table 4.1. The scaling factors a_1 and a_2 assure normalization.

We do not know the precise age distribution of stars in the O-type sample. To derive the initial surface rotational velocity distribution, the ages of the sample stars are neces-

Table 4.1.: Summary of mean values, standard deviations and scaling factors of all Gaussian functions.

Gaussian #	a	μ km/s	σ km/s
1	0.550	125.224	38.799
2	0.465	312.519	143.925

sary. The difference between the initial and the current rotational velocity distribution is due to the evolution of massive stars on the main sequence. They loose mass and angular momentum in stellar winds and change in radius because of stellar expansion, both affecting the surface rotational velocity with time.

Simulating a population of 2 Myr old stars, we find that the differences between initial and current distributions are negligible compared to the accuracy we need for our qualitative analysis. The mean value of the Gaussian function describing the low velocity peak of the surface rotational velocity distribution of the 2 Myr old stars is shifted by 5 km/s towards lower rotation rates compared to the initial distribution. We use the current surface rotational velocity distributions given by the deconvolved v_{rot}-distributions as our input in the simulations.

4.2.6. Initial mass and surface rotational velocity range

The probability density function of the surface rotational velocity derived from the VFTS data shows a high velocity tail. Therefore the initial surface rotational velocities should cover a range from 0 to 500 km/s for the population synthesis calculations. Our sample stars should be compared to stars having spectral classes between O7 and O2. Therefore we define our populations of O-stars to start with $20\,M_{\odot}$. Our models include stars up to $500\,M_{\odot}$.

4.2.7. Star formation history

The age distribution of the very massive stars in 30 Dor is highly discussed with ages reaching from 1 – 3 Myr for R136 (de Koter et al. 1998; Massey & Hunter 1998; Schweizer 2004; Sabbi et al. 2012). Additionally, Selman & Melnick (2001) mention several starbursts for the distinct populations within 30 Dor with discrete episodes of star formation at 1, 2.5 and 5 Myr.

Within this chapter we want to investigate the effect of different star formation histories on the population of the very massive stars. We start with four age distributions described by a delta function at one, two, three and five Myr. By comparing to the

observations we can gain insight into the age distribution of the very massive stars in 30 Dor. Additionally to these starbursts, we assume continuous star formation to investigate which regions in the HR diagram can be populated by our models. With the requirement to the maximum age, that even stars at the lower limit of the initial mass range can reach the end of the main-sequence phase. The differences between our predictions and the observations will tell us whether our models agree with the evolution of the very massive stars in 30 Dor or not. This will help us to improve the physical assumptions (rotational mixing, mass loss, Eddington factor, ...) in the stellar evolution models presented in Köhler et al. (2015).

As the very massive stars are low in number, to analyse them more precisely, the continuous star formation scenario is calculated for flat distributions of initial mass and initial surface rotational velocity.

Table 4.2.: Summary of distribution function applied for the population synthesis calculations.

Sim.	IMF slope	initial $v_{\rm rot}$	star formation history	rotation axis
1	-2.35	double gaussian	delta function: 1Myr	uniform dist.
2	-2.35	double gaussian	delta function: 2Myr	uniform dist.
3	-2.35	double gaussian	delta function: 3Myr	uniform dist.
4	-2.35	double gaussian	delta function: 5Myr	uniform dist.
5	-2.35	double gaussian	uniform dist.	uniform dist.
6	0	uniform dist.	uniform dist.	uniform dist.

4.3. Observational Data - VFTS

For a first qualitative analysis, the observational data of O-type stars in 30 Dor (VLT-Flames Tarantula Survey) is used. Our dataset contains information about spectral type, luminosity, effective temperature, projected surface rotational velocity and helium mass fraction of 244 O-type stars (data from Crowther & Smith (1997); Crowther & Dessart (1998); Massey & Hunter (1998); Foellmi et al. (2003); Crowther & Walborn (2011); Evans et al. (2011); Ramírez-Agudelo et al. (2013); Bestenlehner et al. (2014); Sabín-Sanjulián et al. (2014); Walborn et al. (2014)). These stars are shown in Figure 4.4.

We focus our population synthesis on massive stars of spectral type O7 and earlier. Stars of spectral type O8 and O9 (gray dots in Figure 4.4) are not taken into account for further comparison, as well as stars were no helium mass fraction is known (red dots). Additionally, 16 stars do not contain information about the projected surface rotational

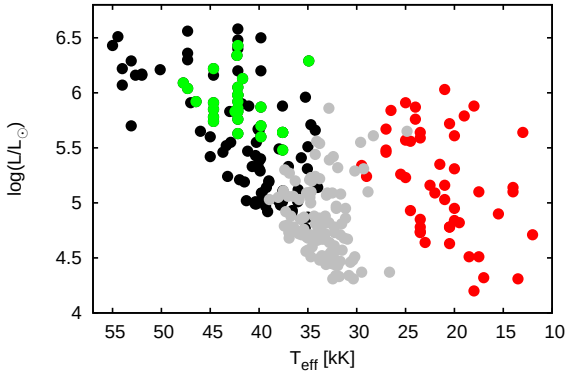

Figure 4.4.: The HR diagram of the O-type stars in the VLT-Flames Tarantula Survey. Stars of spectral type O8 and O9 are depicted as gray dots, while stars of type O7 and earlier are shown as black dots. Stars depicted in green do not contain information about the spectral type and stars depicted in red do not contain information about helium mass fraction.

velocity. The remaining sample (86 stars – later referred to as our observational sample) is given in Table C.1.

4.4. Results - starburst

4.4.1. Hertzsprung-Russel diagram

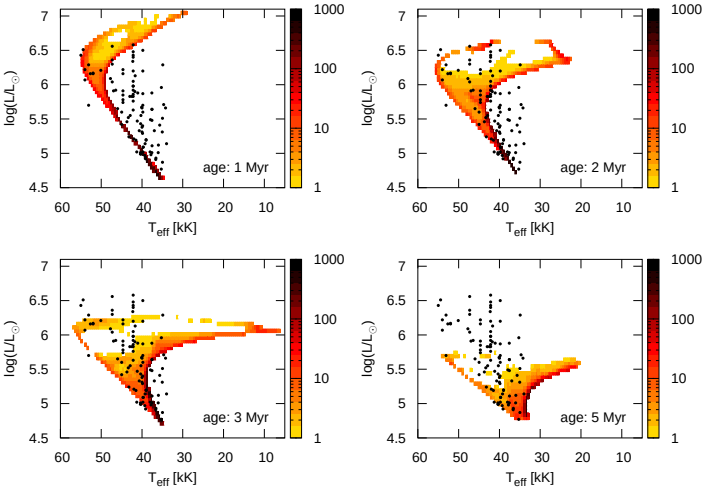

Figure 4.5.: The luminosity is depicted as a function of the effective temperature for starburst of one, two, three and five Myr old stars. The number of stars in each pixel normalized to 1000 given by the colour coding. Additionally, stars of our observational sample are given as black dots.

Figure 4.5 shows the simulated populations in the Hertzsprung-Russel (HR) diagram. Starbursts of one, two, three and five Myr old stars are assumed. For all density plots shown in this section, the color coding indicates the number of simulated stars in each pixel normalized to 1000.

Slowly rotating models (initially $v_{\rm rot} \leq 200\,$km/s) evolve similar to each other. The effective gravity is reduced, leading to a decrease in effective temperature and lumi-

nosity. In comparison, fast rotating models are mixed efficiently showing an increase in effective temperature and luminosity. Rapid rotating models even evolve chemically homogeneous and show characteristics similar to those of blue stragglers. At which velocity chemically homogeneous evolution starts, depends on the initial mass as discussed in Brott et al. (2011a); Köhler et al. (2015). In our case, the transition towards chemically homogeneous evolution is seen for stars in the velocity range of 200 to 400 km/s.

The distribution of stars in the HR diagram (see Figure 4.5 for each starburst age) shows a high density strip caused by slow rotating stars. Approximately 90% of all stars (the quantitative analysis is presented in Section4.6) populate this area. A second, but reduced, high density strip, caused by the rapid rotating stars effected by chemically homogeneous evolution, is located at higher effective temperatures. Chemically homogeneous evolving stars of different initial masses evolve very alike each other, which leads to the seen density increase on the blue side of the HR diagram found in each simulation. The sub-population produced by rapidly rotating stars is visible for all starburst simulations independent of age. Between them, we find the fast rotating stars. Fast rotating models spread a wide range in the HR diagram at a velocity range of approximately 200 to 400 km/s.

The main-sequence lifetime decreases with increasing initial mass. Therefore the maximum luminosity in Figure 4.5 decreases with increasing age of the stars in each starburst simulation. Stars more massive than 100 $M_\odot$ initially are only present in the starburst simulations of one, two and three Myr old stars. In case of the synthetic population of five Myr old stars, stars more massive than 100 $M_\odot$ initially have already left the main-sequence.

For the starburst of two and three Myr in age, two features are seen, caused by the evolution of the massive stars with $M_\odot \geq 80\,M_\odot$ (see Figure 3.2). As the stellar evolution models are affected by strong mass loss increase due to the bi-stability jump (Vink et al. 2000, 2001) at an effective temperature of 25 000 K or for stars near the Eddington limit, they turn blue-ward in the HR diagram, causing a limit similar to the Humphreys-Davidson limit. According to the simulation, we expect no stars to be observed beyond this limit. The other feature is obvious in the two Myr starburst simulation. At $\log L/L_\odot = 6.6 \pm 0.1$ we see an increase in density around 40 000 to 50 000 K. It is related to the very massive stars, as they are effected by the Hamann et al. (1995) mass loss rate (later referred to as WR mass loss rate). Due to the strong increase in mass loss, the very massive stars loose 50–80% of their initial mass until hydrogen exhaustion in the core. As a result, they evolve towards lower luminosities and higher effective temperatures, as explained in Section 3.3.2.

A widening of the main sequence band due to rotational mixing is clearly visible for our observational sample. Several stars are showing characteristics of chemically homogeneous evolution. This will be seen more clearly in comparison to continuous star formation in the Section 4.5. The position of stars from our observational sample in the HR digram is not typical for stars being born at the same time. The dataset favours the idea of stars being formed during several starbursts, with stars being one to five Myr old.

4.4.2. Enhancement of helium at the surface

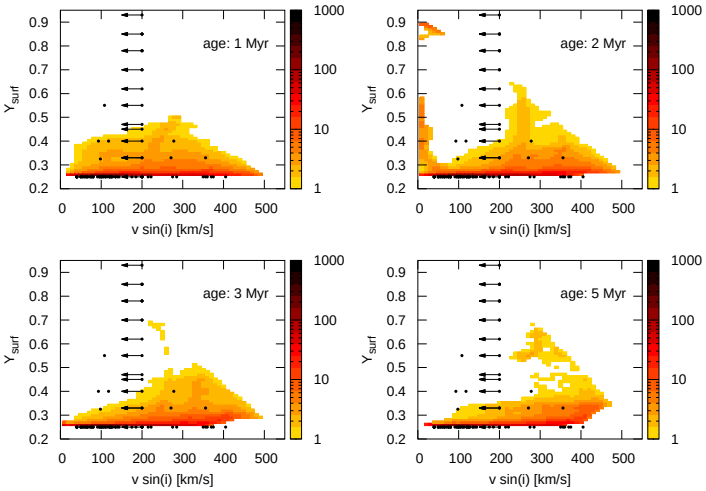

Figure 4.6.: The helium mass fraction at the surface is depicted as a function of the projected surface rotational velocity for starbursts of one, two, three and five Myr old stars. The number of stars in each pixel is given by the colour coding. Additionally, stars of our observational sample are given as black dots.

Figure 4.6 shows all density plots of the surface helium mass fraction Y as a function of the projected surface rotational velocity $v \sin(i)$ (later referred to as He-Hunter diagram) for starbursts of one, two, three and five Myr old stars.

For very massive stars, the enhancement of helium at the surface is affected by rotational mixing and mass loss. Stars more massive than $20\,M_\odot$ mix more efficient, the higher the rotation rate and the more massive they are. Due to the Salpeter-IMF and the surface rotational velocity distribution, the highest probability to find stars in the He-Hunter diagram (Figure 4.6) is at slow rotation rates showing no or only moderate enhancement of helium at the surface ($Y \leq 0.3$). The higher the initial surface rotational velocity, the more efficient is the rotational mixing and the stronger is the enrichment of helium at the surface.

Mass loss affects the enhancement of helium at the surface only for stars initially more massive than $100\,M_\odot$. The more mass is lost (depending on the initial mass and age), the higher $Y_{\rm surf}$ and the lower $v_{\rm rot}$. Stars which are stripped significantly by the WR mass loss, have lost the majority of their angular momentum and rotate with less than 50 km/s. These stars accumulate at the left of the He-Hunter diagrams. In case of one Myr old stars, the mass loss did not yet lead to the stripping of the star. For the three and five Myr old stars, the number of simulated stars with an initial mass $M_{\rm ZAMS} \geq 100\,M_\odot$ is negligible (see Section 4.4.3 - three Myr old stars: $\ll$1%; five Myr old stars: 0%). For these two synthetic populations, the enhancement of helium at the surface is caused by rotational mixing, not mass loss and therefore these stars have not lost the majority of their angular momentum. Only in case of the simulated two Myr old stars, the accumulation at the left of the He-Hunter diagram is seen ($v \sin(i) \leq 50$ km/s).

In general, for increasing $Y_{\rm surf}$, the velocity density profile first tends towards higher $v \sin(i)$ as rotational mixing is dominant and later to lower $v \sin(i)$ when mass loss becomes the dominant process.

Stars with high projected surface rotational velocities need to have high surface rotational velocities at the ZAMS. The older the population, the more time these stars had to mix and therefore the higher the surface helium mass fraction. As a result of the rapid rotators already being enriched, with increasing age of the stars we expect a decrease in the number of stars with helium mass fractions of $Y_{\rm surf} < 0.3$ and projected surface rotational velocities $v \sin(i)$ between 400 and 500 km/s.

75% of O-type stars in our observational sample are not enhanced in helium, what is consistent to our simulations (80-90%). Nine stars in Figure 4.6 show enhancement of helium at the surface and additional 16 stars with $Y > 0.3$ are shown in the Figure by arrows indicating that only upper limits to the projected surface rotational velocities are given. The high helium mass fractions up to 0.93 and low projected surface rotational

velocities substantiate the assumption that at least some of these stars will be enriched by mass loss and not by rotational mixing only. As predicted by the simulation, no stars are found in the upper right corner of Figure 4.6. The quantitative analysis follows in Section 4.7

4.4.3. Mass distribution

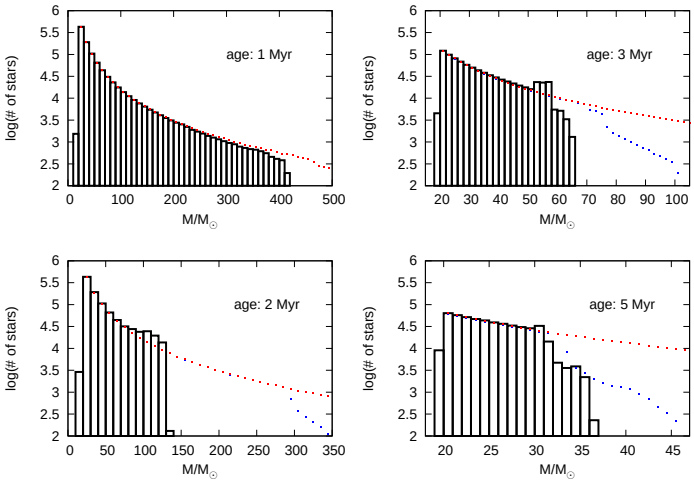

Figure 4.7.: Mass histograms containing the population synthesis data for one, two, three and five Myr old stars are shown in black columns normalized to 10^6 stars per simulation. Different mass binning is chosen to ease the comparison by eye. Additionally the initial mass function is shown in red and the starting mass function SMF (not counting stars that already left the main sequence) with blue dots.

Figure 4.7 shows the mass distributions of the simulated one, two, three and five Myr old stars. The histogram shows the mass distribution of the simulated stars for the assigned age (later referred to as present day mass) and the red dots correspond to the Salpeter-IMF. The blue dots give the distribution of initial masses of the simulated stars

(later referred to as starting mass function SMF), that means excluding stars that have left the main-sequence.

The underlying stellar models are not evolved equally far. Especially the stellar evolution models of the very massive fast rotators did not reach the core H-exhaustion. Fast rotating stars, that are drawn with $M \geq 300\,M_{\odot}$, are removed from the synthetic population if the fractional main-sequence lifetime of the star is not covered by the stellar evolution models of the four nearest neighbours (see Section 4.2). Comparing SMF and the Salpeter-IMF, we see that these simulation errors are negligible from the statistical point of view.

A reduced number of stars in the first bin exist due to the chosen starting mass of $20\,M_{\odot}$. During time, our stellar evolution models loose mass by stellar winds, so stars initially about $20\,M_{\odot}$ decrease in mass to less than $20\,M_{\odot}$ giving the number of stars in the first bin. But there are no stars initially below $20\,M_{\odot}$.

A reduction of the number of stars in the bins toward the upper mass end is seen in all simulations older than one Myr. The main sequence lifetime of the underlying stellar models depends on the initial surface rotational velocity. The higher the rotation rate, the longer the main sequence phase. This effect shapes the higher mass end of the underlying SMF.

Figure 4.7 shows the effect of strong wind mass loss of the massive and especially the very massive stars, as seen very well comparing initial (SMF) and present day mass distribution. With increasing age of the simulated starburst, the difference between initial and present day mass grows. The effect of mass loss on the evolution of the very massive stars can be seen when comparing the maximum starting mass and the maximum present day mass (see Table 4.3). The 2 Myr old stars lost a significant amount of their initial mass (55% for $M_{\mathrm{ZAMS}} = 400 M_{\odot}$) due to the WR mass loss.

Table 4.3.: Comparison of the maximum mass on the zero-age main sequence and the maximum present day mass

starburst	$M_{\mathrm{ZAMS,max}}$ $M_{\odot}$	$M_{\mathrm{present,max}}$ $M_{\odot}$
1 Myr	500	420
2 Myr	400	140
3 Myr	106	66
5 Myr	47	37

The population of one Myr old stars is different from the other populations, because the maximum initial mass of the cluster is defined by the grid boundary. Additionally, these stars are not yet affected by the Hamann et al. (1995) mass loss rate.

With time stars loose more mass and we see an accumulation around the maximum present day mass of the starbursts. This effect is seen in observations (Stolte et al. 2005) and stellar evolution calculations by (Schneider et al. 2014a, 2015), who shows that it is caused by mass loss.

Our observational sample does not contain information about the stellar mass yet. Therefore a comparison has to be done later.

4.4.4. Rotational Velocity distribution

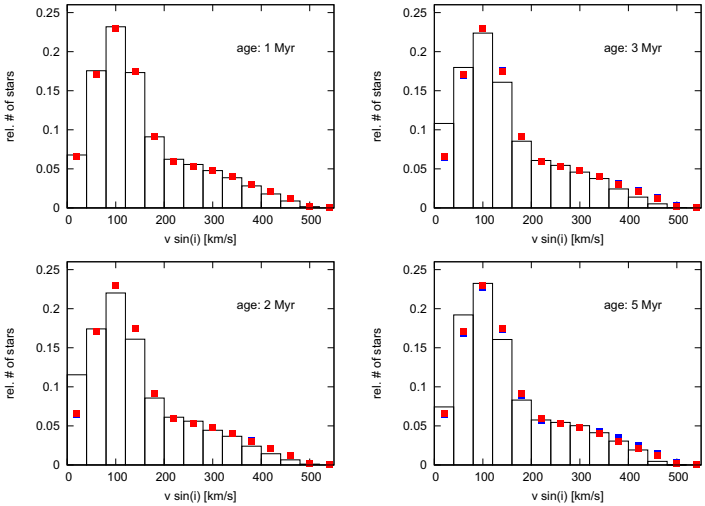

Figure 4.8.: Histograms of the projected surface rotational velocity of simulated stars are shown in black, the initial distribution in red and the starting velocity function SVF in blue. They contain the population synthesis data for starsburst of one, two, three and five Myr old stars. The velocity binning is chosen to be 40 km/s.

Figure 4.8 shows several histograms depicting the number of stars within a given range in surface rotational velocity of 40 km/s for one, two, three and five Myr. The black histogram gives the present day velocity distribution of the starbursts, the red dots the initial rotational velocity distribution and the blue dots correspond to the initial rotation rates of the simulated stars (referred to as SVF, comparable to the SMF).

On first sight, the present day projected surface rotational velocity distributions are very alike for each starburst. In all cases, the typical low velocity peak and the high velocity tail of the initial surface rotational velocity distribution remain visible. In general, age effects are small.

Table 4.4.: Comparison initial – present day projected surface rotational velocity distribution of the starbursts

$v \sin(i)$ range km/s	1 Myr	2 Myr	3 Myr	5 Myr	initial
≤ 200	0.74	0.76	0.76	0.74	0.73
200–400	0.23	0.22	0.22	0.23	0.23
≥ 400	0.03	0.02	0.02	0.02	0.04

The surface rotational velocities of stars change with time. As stars evolve, they are affected by mass loss due to stellar winds and therefore loss of angular momentum. Especially, very massive stars loose up to 50% of their initial mass until hydrogen exhaustion in the core and are slowed down significantly. Although these effects apply, it can be seen in Table 4.4 for starbursts of one – five Myr old stars that the differences in the distributions are only moderate. The reason is found in the fact, that the simulated populations (mass distribution: Salpeter IMF; mass range: 20–500$M_{\odot}$) are dominated by stars less massive than 80$M_{\odot}$ with 86% for 1 Myr old stars up to 100% for 5 Myr old stars. As the position of the observed stars (see Table C.1) in the HR diagramm is consistent with a lower mass limit of approximately 20$M_{\odot}$, we assume that the present day velocity distribution can be used as the initial distribution (for the given Salpeter-IMF) in our simulations. The fraction of stars initially more massive than 80$M_{\odot}$ (simulations: $\approx 10\%$; stars in the observational sample with $\log L/L_{\odot} \geq 6.0$: 25%;) and their influence on the projected surface rotational velocity distribution are moderate and already taken into account.

4.5. Results - continuous star formation

4.5.1. Hertzsprung-Russel diagram

Figure 4.9 shows HR diagrams for continuous star formation. The left panel give the ZAMS mass and ZAMS-velocity distributions explained in Sections 4.2.3 and 4.2.5, while the right panel show the results for flat distributions in initial mass and initial rotation rate. The flat distributions are chosen to line out features produced by the stellar evolution of the very massive stars and the very fast rotators, as they are difficult

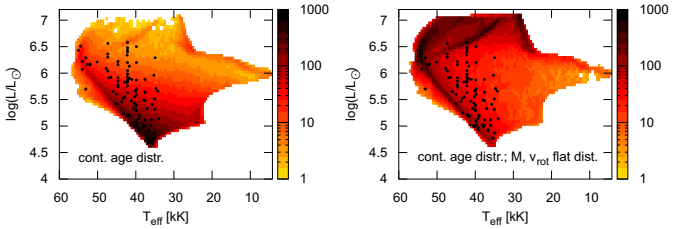

Figure 4.9.: The luminosity is shown as a function of the effective temperature for continuous star formation. The left panel shows the synthetic population assuming the VFTS tailored surface rotational velocity distribution, while the right panel shows the results for flat distributions in initial mass and initial surface rotational velocity. The colour coding gives the number of simulated stars in each pixel. Additionally, stars of our observational sample are given as black dots.

to see for the VFTS tailored distributions, as the number of drawn very massive stars is very low due to the Salpeter-IMF.

The HR diagrams in Figure 4.9 show that the difference between slowly and rapidly rotating models is significant. Rapid rotators evolve chemically homogeneously and therefore to the left of the ZAMS for stars with initial masses between 20 and 125 $M_\odot$ (Brott et al. 2011a; Köhler et al. 2015). Rapidly rotating stars more massive than 125 $M_\odot$ evolve to the right of the ZAMS, with increasing luminosity. The bending of the ZAMS toward low effective temperature, as occurring for very massive stars (Köhler et al. 2015), is seen in Figure 4.9 as well.

Additionally, stars are expected to be seen in the HR diagram along a narrow band from ($T_{\rm eff}$=33 000 K; $\log L/L_\odot = 7$) to ($T_{\rm eff}$=50 000 K; $\log L/L_\odot = 6.4$). This effect is caused by the very massive stars when affected by the Hamann et al. (1995) mass loss rate. They loose mass quickly and are stripped to reveal deeper hotter layers as mentioned in Köhler et al. (2015). There are no observational counterparts seen in Figure 4.9. Assuming the Salpeter-IMF and the VFTS tailored surface rotational velocity distributions less than 1% of the simulated stars are expected within this region (see Section 4.7.2).

In general, the underlying stellar models are consistent with the observational sample. A small number of stars show characteristics of chemical homogeneous evolution, being located to the left of the ZAMS, while the position of the remaining stars are spread on

the main sequence band to the right of the ZAMS. The observational sample contains only stars with $T_{\rm eff} \geq 30\,000$ K. Therefore a comparison to the Humphrey-Davidson limit can not be done. After the bending of the ZAMS, no chemical homogeneous stars are predicted to the left of the ZAMS, but this feature is difficult to analyse due to the low number of stars with these high luminosities. The total number of stars with $M \geq 100 M_{\odot}$ in our synthetic population is too small (3% for VFTS tailored distributions) for a qualitative analysis of the features of the very massive stars in the HR diagram.

4.5.2. Enhancement of helium at the surface

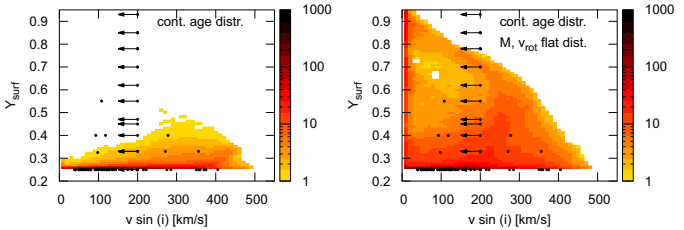

Figure 4.10.: Surface helium mass fraction as a function of the projected surface rotational velocity of simulated stars assuming continuous star formation. The left panel show the synthetic population for the VFTS tailored surface rotational velocity distribution and the right panel the results assuming flat distributions in initial mass and initial surface rotational velocity. The number of stars in each pixel is given by the colour coding. Additionally, stars of our observational sample are given as black dots.

Figure 4.10 shows the helium mass fraction as a function of the projected surface rotational velocity for the simulated stars assuming continuous star formation.

As for the starburst simulations, the majority of the simulated stars are characterized as massive stars with slow rotation showing no or moderate enhancement of helium ($Y_{\rm surf}$ less than 0.3). The higher the surface rotational velocity of the stars, the stronger they are mixed rotationally. This leads to the high probability in the density profile tending towards higher $v \sin(i)$ for higher $Y_{\rm surf}$.

The more massive the star, the stronger the mass loss affects the enhancement of helium at the surface while slowing down the star. For models initially more massive than 100 $M_{\odot}$, mass loss becomes important even for slowly rotating models, with the helium

mass fraction increasing to more than 50% with decreasing rotation rate, resulting in a band of increased probability leading to the upper left corner (low $v \sin(i)$, high Y). In general, with increasing helium mass fraction $Y_{\rm surf}$, the high probability in the velocity density profile first tends towards higher $v \sin(i)$ due to rotational mixing and than to lower $v \sin(i)$ due to mass loss being the dominant process.

26% of stars in our observational sample show enhancement of helium at the surface. As already mentioned in Section 4.4, the 18 highly enriched stars with $v \sin(i) <$ 200 km/s (21% of the observational sample) can not be explained by rotational mixing only, but in combination with mass loss.

4.5.3. Mass distribution

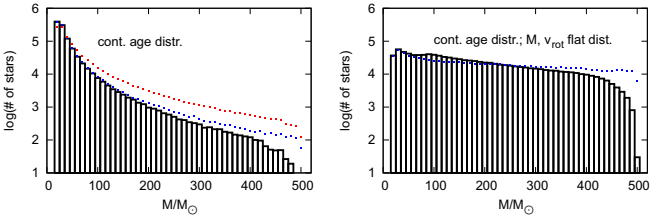

Figure 4.11.: Mass histograms containing the population synthesis data for continuous star formation are shown in black columns normalized to 10^6 stars per simulation. The left panel corresponds to the simulation assuming VFTS tailored distributions and the right panel to flat distributions in initial mass and rotation rate. Red dots show the Salpeter-IMF (in the left panel) and blue dots the starting mass function SMF. The size of each mass bin is 10 $M_\odot$.

Two histograms are given in Figure 4.11 showing the present day mass distributions (black) for our simulations using VFTS tailored (left panel) and flat distributions (right panel) in initial mass and initial surface rotational velocity. The number of stars in the first bin is low, because there are no stars drawn with an initial mass below 20 $M_\odot$, but in case of the present day mass they exist due to mass loss. The number of stars in the last bin is low as well because the highest mass in our simulations (500 $M_\odot$) does not equal the upper mass limit of the histogram bins (505 $M_\odot$). Deviations at the high mass end are visible caused by low number statistics.

The higher the initial mass, the shorter is the duration of the main sequence phase. Stars that already left the main sequence, are removed from the sample and are not part of the present day mass distribution (black) and the SMF (blue). Within the synthetic populations, the fraction of stars that are removed from the sample increases slightly with increasing initial mass. This effect explains the deviation of the SMF from the IMF. Therefore the initial distributions in mass for continuous star formation have a steeper slop (Salpeter IMF: $\gamma = -2.65$; flat distribution: $\gamma = -0.48$) than given in Table 4.2.

The difference between the SMF and our present day mass function is caused by wind mass loss and the decrease in mass due to nuclear fusion of hydrogen in the core. As the mass decreases with time, a steeper slope of the present day mass function is seen compared to the SMF and IMF for the presented simulations. The total number of all stars in the SMF and the present day mass function is equal, but the decrease in the high mass end is more highlighted than the increase at the low mass end of the histogram due to the logarithmic scale.

On the right panel of Figure 4.11 a bump is visible around $100\,M_{\odot}$. Stars with $M_{\mathrm{ZAMS}} \geq 100\,M_{\odot}$) are significantly affected by WR mass loss reducing their mass down to $50 - 120\,M_{\odot}$ at the end of the main sequence evolution (see Köhler et al. (2015)). This leads to an accumulation of stars around this mass range.

4.5.4. Rotational velocity distribution

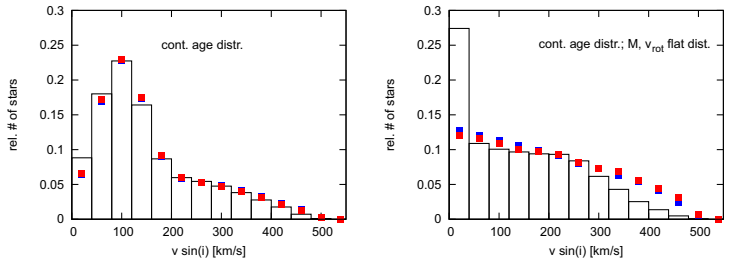

Figure 4.12.: Distribution of present-day (black), initial (red) and starting (SVF, blue) projected surface rotational velocity of simulated stars for continuous star formation in relation to the total number of stars in each simulation assuming VFTS tailored surface rotational velocity distributions (left panel) and flat distributions (right panel) in initial mass and initial surface rotational velocity. The velocity binning is chosen to be 40 km/s.

Figure 4.12 shows two histograms of the projected surface rotational velocity (present-day (black), initial (red) and starting (SVF, blue)) for continuous stars formation with a surface rotational velocity binning of 40 km/s. The number of stars in the high velocity tail is reduced due to transport of angular momentum as seen in the right panel of Figure 4.12. We have more slow rotating stars in the present-day surface rotational velocity distribution than initially.

Table 4.5.: Comparison of the initial and present day projected surface rotational velocity distribution of the continuous star formation (VFTS tailored) simulation.

$v \sin(i)$ range km/s	cont	initial
≤ 200	0.75	0.73
200–400	0.23	0.23
≥ 400	0.03	0.04

Although there are differences between the VFTS tailored initial and present day projected surface rotational velocity distribution as summarized in Table 4.5, we find a good agreement between both distributions with respect to the relative number of slow, fast and rapid rotators. As already discussed in Section 4.4, the simulated populations are dominated by stars initially more massive than $80 M_{\odot}$ (94% for continuous star formation). Stars with $M \geq 80 M_{\odot}$ are considered in the simulation, but their effect on the projected surface rotational velocity distribution is moderate due to the mass range of $20 - 500\, M_{\odot}$.

The assumption, that the present day rotational velocity distribution is used as the initial one, for simulations to compare to our observational sample, is justified for the continuous star formation history as well. The lower luminosity limit for the observed stars in our sample is consistent with a lower mass limit of approximately $20\, M_{\odot}$.

4.6. Defining reference boxes

In Sections 4.4 and 4.5 we presented synthetic stellar populations for different star formation histories. We introduce several regions in the different diagrams (He-Hunter and HR diagram) by means of interesting evolutionary features seen and count the number of models in them, which we present in Section 4.7.

4.6.1. HR diagram

As seen in Figure 4.5, the starburst simulations of 1 to 5 Myr old stars show two very dense fields of stars in the HR diagram, with a low populated area in-between. The separation of these two high density bands occurs at lower mass, the older the simulated population. The slowly rotating stellar models produce the right accumulation of simulated stars, which we define as stars in Box 1. Rapidly rotating stars accumulate, producing the left high density band, which we define as Box 2. The low populated area in-between is defined as Box 3. We therefore distinguish slow (non-chemically homogeneous evolution), fast (partially-chemically homogeneous evolution - Class HO defined in Section 3.3.4) and rapid (quasi-chemically homogeneous evolution) rotating stars.

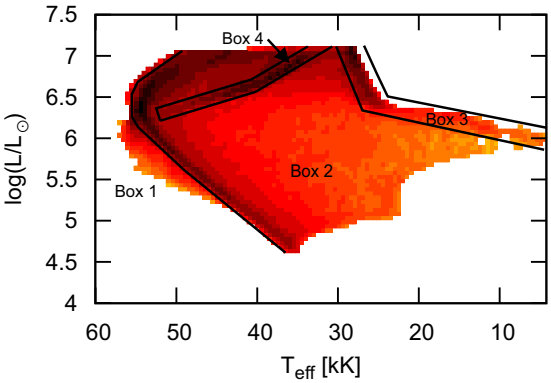

Figure 4.13.: Definition of Box 1 - Box 4 in the HR diagrams for the continuous star formation simulations.

For the HR diagrams of continuous star formation history, we define other boxes because the HR diagram is differently populated by stars than in case of starbursts (see Figure 4.13). Box 1 is assigned to stars to the left of the ZAMS, which are related to chemical homogeneous evolution by rotational mixing. Box 2 summarizes stars to the right of the ZAMS, except for two special areas where stars accumulate, which are taken into account in Boxes 3 and 4. Box 3 summarizes stars accumulated at the blue-ward turn of the underlying stellar evolution models in the HR-diagram, as they evolve near the Eddington limit. Box 4 contains the very massive stars affected by the WR mass

loss rate, but also stars not yet affected by the WR mass loss, which evolve red-ward through this region.

4.6.2. He-Hunter diagram

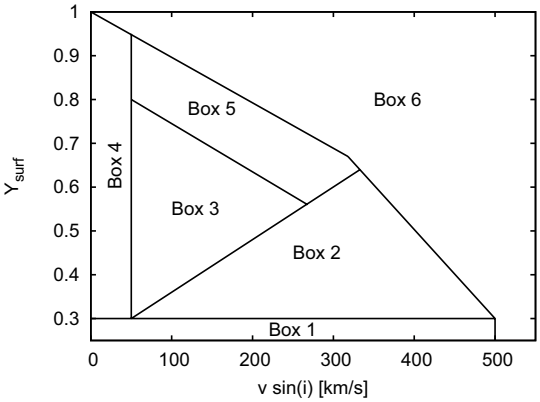

Figure 4.14.: Definition of Boxes 1 – 6 in the He-Hunter diagrams for our simulated starbursts and continuous star formation simulations.

Figure 4.14 defines all six boxes in the He-Hunter diagrams. Box 1 corresponds to the non or only moderate enriched stars with $Y_{\rm surf} \leq 0.3$. The triangular shape of Box 2 is chosen to cover the stars with helium enrichment affected by both rotational mixing and mass loss. Box 3 comprises the region in the He-Hunter diagram between Box 2, 4 and 5 where the likelihood of stars to be observed is small, as they evolve quickly through this part. Box 4 covers slowly rotating models with $v \sin(i) \leq 50$ km/s and Box 5 copes with the accumulation of stars in the band towards the left upper corner of the He-Hunter diagram. At last, Box 6 combines the remaining parts with no or very few models to be expected.

4.7. Discussion

4.7.1. Starburst

As expected due to the Salpeter-IMF, the majority of stars populate Box 1 with around 90% of each simulated starburst. The exact value varies from 92% (1 Myr) to 85%

Table 4.6.: Fraction of models per Box in the He-Hunter diagram for the simulated starbursts in comparison to the stars of our observational sample.

	1 Myr	2 Myr	3 Myr	5 Myr	observed
Box 1	0.920	0.852	0.882	0.897	0.73
Box 2	0.064	0.065	0.065	0.061	0.05
Box 3	0.010	0.014	0.011	0.012	0.03
Box 4	0.003	0.052	0.020	0.001	0.00
Box 5	0.000	0.011	0.012	0.010	0.00
Box 6	0.002	0.006	0.010	0.020	0.00

(2 Myr). As a result of the surface rotational velocity distribution and the Salpeter-IMF, approximately 6% of all stars are counted in Box 2, which correspond to the rapid rotating stars. Only 1% of stars are assigned to Box 3. The numbers of these three Boxes are very similar for all four different starbursts. We draw the conclusion, that the very massive stars are negligible from the statistical point of view (due to the IMF) for the number of stars in Boxes 1, 2 and 3 and that the effect of the age of the cluster is small as well.

Although low in probability, stars initially more massive than $100\,M_{\odot}$ have a strong influence on not only the number of stars in Boxes 4 and 5, but also whether there are models appearing at all. These are regions in the diagram that are populated exclusively (Box 5) or in great parts (Box 4) by the very massive stars. Especially Box 4 is of interest due to the strong changes in the number of stars depending on the age of the starburst. The 2 and 3 Myr old starbursts show a relatively high number of stars with 5% and 2%. Stars observed in Box 4 (only occupied if stars are old enough to have reached the phase of WR mass loss) and Box 5 can evaluate the existence of the very massive stars and the mass loss recipes we use in the stellar evolution calculations presented in Köhler et al. (2015).

The majority of stars (75%) show no or only moderate enhancement of helium. They are found in Box 1. Only 4 stars can be assigned to Box 2 and 3 star to Box 3. For 22% of stars in the sample, only upper limits to the projected surface rotational velocity are known, giving us a hint about the occupied boxes. We found 5 stars with $0.3 < Y < 0.5$, what refers to boxes 2, 3 or 4 and 11 stars with $Y > 0.5$ that would occupy boxes 3, 4 or 5. They are not included in Table 4.6.

Stellar evolution models of very massive stars are affected by the strong WR mass loss. We find 5 stars in the observational sample with $Y > 0.8$ (one of them even with $Y > 0.9$) what is consistent with the assumption that the enhancement of helium at the surface of very massive stars is affected by strong mass loss. Unfortunately, due to the

fact that in these cases only upper limits are known we can not evaluate the assumed phase of WR mass loss quantitatively.

Table 4.7.: Fraction of models per Box in the HR diagram for the simulated starbursts.

	1 Myr	2 Myr	3 Myr	5 Myr
Box 1	0.919	0.849	0.867	0.869
Box 2	0.035	0.076	0.089	0.102
Box 3	0.047	0.076	0.045	0.030

Table 4.8.: Fraction of stars in our observational sample compared to the Boxes defined for our starburst simulations.

	1 Myr	2 Myr	3 Myr	5 Myr
Box 1	0.13	0.13	0.14	0.01
Box 2	0.06	0.28	0.38	0.38
Box 3	0.03	0.09	0.24	0.18

90% of all simulated stars are counted in Box 1, only 3-10% are found to be in Boxes 2 and 3. The number of stars in Box 2 and Box 3 are very alike for each starburst simulation. The high density along Box 2 is the result of the stars occupying a small area in the HR diagram. Although low in number, the differentiation in Box 1 and 2 is very conspicuous and gives a good opportunity to distinguish slowly rotating and rapidly rotating models in the HR diagram in the case of starbursts. One clear trend is seen for the number of stars in all starbursts. The older the population, the more stars are found in Box 2. This and the luminosity, where the two high density bands separate, can be used to evaluate the age of a cluster. Particularly interesting is the increased density around $\log L/L_{\odot} = 6.6$ at 2 Myr corresponding to stars affected by the WR mass loss with 2% of all stars found there, which are counted in Box 2. From the point of statistics and the location in the HR diagram, it will be difficult to point out the stars affected by the WR mass loss.

Comparing the fraction of observed stars in each Box (boxes vary with age of the starburst) we find no good agreement to any of the starburst simulations. On one hand, the distribution of stars in the HR diagram starts to widen below $\log L/L_{\odot} = 5.0$, which is consistent to our 5 Myr starburst model. On the other hand, very massive stars are observed with luminosities up to $\log L/L_{\odot} = 6.5$, which fits well to our 2 Myr starburst. Therefore, we expect the stars in the observational sample to be formed from several starbursts with ages between 2 and 5 Myr or from continuous star formation.

4.7.2. Continuous star formation

Here, we analyse the populations, simulated for the two continuous star formation scenarios. The same boxes are used for the He-Hunter diagrams as seen in Figures 4.14.

Table 4.9.: Fraction of models per Box in the He-Hunter diagram for the continuous star formation scenarios in comparison to the stars of our observational sample.

	cont SF	flat dist.	observed
Box 1	0.899	0.439	0.73
Box 2	0.057	0.224	0.05
Box 3	0.010	0.084	0.03
Box 4	0.014	0.199	0.00
Box 5	0.008	0.045	0.00
Box 6	0.012	0.009	0.00

Table 4.9 summarizes the relative number of stars in Boxes 1 to 6 for stars in the He-Hunter diagram. The numbers are given for a Salpeter-IMF and the surface rotational velocity distribution derived from the VFTS (cont SF), and for flat distributions in mass and surface rotational velocity (flat dist.). We gain similar results as explained in the case of the starburst simulations. Most of the stars are assigned to Box 1 with the exact values of 90% and 44% depending on the IMF. We can see that even for a flat distribution in mass and rotation rate, almost half of all stars are counted in Box 1.

For the Salpeter-IMF and the surface rotational velocity distribution derived from the VFTS data, about 6% of models are assigned to Box 2 and 1% to Box 3. These numbers are similar to the one from the starburst simulations. This means, not only do the very massive stars have a negligible effect on the results in these three boxes, but also the star formation scenario. We expect to find about 1% of the stars in Boxes 4 and 5. As already mentioned in Section 4.7.1, for stars observed around Boxes 4 and 5 only upper limits to the projected surface rotational velocity are known. Therefore we can not evaluate the evolution of the very massive stars quantitatively from this point of view.

Assuming flat distributions in mass and surface rotational velocity, it can be seen, that Box 1 (and Box 6) are populated by the massive stars in large part. Boxes 2, 3, 4 and 5 on the other hand show a higher relative number of stars for these distributions, compared to the distributions derived from the VFTS. They are populated by the very massive and fast rotating stellar models predominantly. Especially in Box 4 are almost as many stars found as in Box 2 in this case. This shows that the features related to the very massive stars (Boxes 4 and 5) are low in probability only because of the Salpeter-IMF, as they are high in number for the flat distributions.

Comparing the fraction of stars in our observational sample with the two continuous star formation scenarios, we find a good agreement to the VFTS-tailored distributions.

Table 4.10.: Fraction of models per Box in the HR diagram for the continuous star formation scenarios in comparison to the stars of our observational sample.

	cont SF	flat dist.	observed
Box 1	0.008	0.014	0.01
Box 2	0.975	0.765	0.97
Box 3	0.012	0.093	0.00
Box 4	0.005	0.129	0.02

Table 4.10 summarizes the relative numbers for both simulations of continuous star formation. The majority of stars, with 97%, are found in Box 1, with about 1% of the models in Boxes 1, 2 and 3. Stars in Box 4 can only be distinguish from stars not affected by the WR mass loss rate when taking into account the helium mass fraction.

The simulation with flat distributions in mass and rotation rate shows that the features in Box 3 and 4, with about 10% in relative number, are only small in probability when using the Salpeter-IMF. The rapidly rotating stars to the left of the ZAMS double to about 1.4% compared to the simulation with Salpeter-IMF and rotational velocity distribution derived from the VFTS data. We can conclude, that the IMF has a strong influence on the number of stars in Boxes 2 to 4, but only a small one for Box 1.

The fraction of stars in our observational sample for each box are comparable to the results we gain for continuous star formation (VFTS-tailored distributions). The fraction of stars in the respective boxes are consistent between the simulation and the observational sample (boxes 1 and 2). No star within our sample is shown in Box 3. As the observational sample does only contain stars with $T_{\rm eff} \geq 30\,000$ K, the limit due to the blue-ward evolution in the HR diagram can not be proven.

According to the simulation assuming VFTS tailored distributions we expect chemically homogeneous evolved stars in Box 1 (0,8%) and in Box 4 (0,5%). Within our observed sample (see Table C.1) we find one star (VFTS-108) in Box 1 and two stars in Box 4 (VFTS-758 and VFTS-1025). All three of them show enhancement of helium at the surface with $Y > 0.7$ and upper limits to the surface rotational velocity are known with $v \sin(i) \leq 200$ km/s, what is consistent to chemically homogeneous evolution. In total we find 9 stars (10%) with $Y \geq 0.7$ and 11 stars (13%) with $Y \geq 0.5$ within our observational sample, what cannot be explained by continuous star formation of single stars.

4.8. Conclusion

We simulate stellar populations of rotating stellar models of Brott et al. (2011a) and Köhler et al. (2015) for LMC metallicity. The following assumptions are made:

- Salpeter-IMF (Salpeter 1955) with the slope $\alpha = -2.35$,
- projected surface rotational velocity distribution derived from the VFTS data for main sequence stars of spectral type O7–O2 (Ramírez-Agudelo et al. 2013),
- stellar spin axes are randomly oriented in space,
- delta starbursts of one, two, three and five Myr in age and
- continuous star formation scenarios (as well for flat distributions in mass and surface rotational velocity).

The population synthesis code Starmaker of Brott et al. (2011b) is used for our simulations.

Our goal is to study the effect of the star formation history on the population of O-type stars and first comparisons to observational data.

We present HR diagrams of our populations, the distributions of stars in the Y – $v \sin(i)$ plane (Y: helium mass fraction, $v \sin(i)$: projected surface rotational velocity) and the current mass and current surface rotational velocity histograms for all star formation scenarios.

Rapidly rotating stars are expected to be seen to the left of the ZAMS for M_{ZAMS} = 20 – 125 $\mathrm{M}_{\odot}$. Although low in probability (0.8% of all stars, cont. star formation) the specific location in the HR diagram and the properties of these stars will make the differentiation easily. Rapidly rotating stars initially more massive than 125 $\mathrm{M}_{\odot}$ are increased in luminosity, but are found to the right of the ZAMS. In the observational sample, we see no stars located left of the ZAMS for $\log L/L_{\odot} \geq 6.3$, confirming the simulation. For starbursts, the rapidly rotating stars will produce a sub-population of stars with blue-straggler characteristics (3 – 8% depending on age). Comparing the observations of 30 Dor with our stars burst simulation, we conclude stars to be born in several starburst between 2 and 5 Myr. In case of multiple starbursts, an explicit sub-population with blue-straggler characteristics is not visible anymore.

The very massive stars are affected by the Wolf-Rayet mass loss rate. They accumulate within a very small area in the HR diagram, with a low probability to be observed (0.5% of all stars in the case of continuous star formation). They can be distinguished from stars evolving red-wards through this area, due to the enhancement of helium at the

surface. We expect an unpopulated region in the HR diagram due to stars being effected due to strong increase in mass loss. Due to the fact that all stars within the observational sample show effective temperatures above 30 000 K the theoretically defined borderline can not be proven.

Within the stellar evolution models of massive stars (see Section 3.3), two major effects lead to an enhancement of the helium mass fraction at the surface – rotational mixing in case of quasi-chemically homogeneous stars and the stripping of stars more massive than 100 $M_\odot$ initially due to WR mass loss. Our populations show that for very massive stars, mass loss is the dominant effects leading to helium mass fractions up to $Y_{\rm surf} = 0.98$. According to the simulation, we expect 1% – 5% of stars within boxes 4 and 5 what is related to stars affected by the WR mass loss.

Comparing the initial and present day mass functions of our synthetic populations, it can be seen, that our simulated O-type stars suffer from strong mass loss with an accumulation of stars near the turn off mass. This effect is referred to as the wind mass-loss bump in literature (Schneider et al. 2014a, 2015).

We find only marginal changes between the initial and present day surface rotational velocity for all star formation history scenarios. For our analysis, we assume that the present day rotational velocity distribution can be used as the initial one for comparision with our observational data. Simulated populations assuming Salpeter IMF in a mass range of 20–500$M_\odot$ are dominated by stars less massive than 80$M_\odot$ (with more than 80% of the populations). Therefore the contribution of very massive stars on the surface rotational velocity distribution is negligible, except for the simulation assuming continuous star formation with flat initial distributions in mass and surface rotational velocity. That implies that for analysing very massive stars, the mass range should be reduced to approximately 60–500 $M_\odot$ (assuming Salpeter IMF). In that case the amount of very massive stars would be increased significantly (approximately 60% of star with $M \geq 80 M_\odot$ and 40% of star with $M \geq 100 M_\odot$).

We only assume single star evolution in our simulations. However, the existence of the high velocity tail in the rotational velocity distribution indicates post-interacting binaries to be present (de Mink et al. 2013; Ramírez-Agudelo et al. 2013), which must have evolved significantly different from single stellar evolution. de Mink et al. (2013) produced a projected surface rotational velocity distribution (low velocity peak and high velocity tail) similar to the ones presented in Sections 4.4 and 4.5 taking into account binary evolution assuming continuous star formation and a uniform initial surface rotational velocity distribution of low and moderate rotating stars ($v_{\rm rot} \leq 200$ km/s). According to her simulation, the high velocity tail is caused by post-interacting binaries

(after Roche-lobe overflow) and the enhancement of nitrogen at the surface is primarily caused by mass transfer instead of rotational mixing.

5. Summary and outlook

Detailed summaries are already presented in the respective chapters. An extended summary and pursued discussion will be given in this Section.

The age of an observed star is in general deduced by fitting isochrones derived from stellar evolution models to the position of the star in the Hertzsprung-Russel (HR) diagram. In Section 2, a method (referred to as nitrogen chronology) to determine age and inclination angle of a star is presented based on the surface nitrogen abundance, projected surface rotational velocity, mass and metallicity. This method is based on stellar evolution models of single rotating massive stars (Brott et al. 2011a). The method of nitrogen chronology is only suitable for single stars evolving as explained by the theory of rotational mixing. Therefore stars suspected to be affected by binary evolution causing a significantly different evolution are incompatible to be analysed by this method.

It could be useful to extend this study to higher masses and to stars showing signs of chemically homogeneous evolution by adapting the equations. Additionally, the method could be extended by using luminosity, effective temperature, surface nitrogen abundance and metallicity as input to derive mass, isochrone age, nitrogen age, inclination angle and rotation rate based on the stellar evolution models. A more advanced approach is presented in Schneider et al. (2014b), based on stellar models of Brott et al. (2011a) and the models discussed in Section 3. In Schneider et al. (2014b) Bonnsai is presented, a method which determines not only stellar parameters of a star but probability distribution for these parameters, depending on observables and their uncertainties, including distribution functions of mass, rotational velocity and age.

The huge benefit of Bonnsai lies in the fact, that stellar parameters which are not yet observed can be predicted and stars which can not be explained by the stellar evolution models will definitely be detected. As this method is based on the same massive single stellar evolution models as the presented nitrogen chronology, Bonnsai can not evaluate stars that are significantly affected by binary interactions as well. In Schneider et al. (2014b) Bonnsai is successfully applied to 18 binary systems from the Torres et al. (2010) sample (not significantly affected by binary evolution).

Comparing the derived ages using the nitrogen chronology for a few stars presented in Table A.2 with the results provided by Bonnsai for the given observables and their uncertainties lead to a general qualitative agreement between Bonnsai and the nitrogen

chronology. Discrepancies are mainly caused due to the fact that the nitrogen chronology is based on the evolutionary mass provided by Hunter et al. (2008b, 2009). In all evaluated cases, the evolutionary masses in Table A.2 is slightly higher than the mass determined by Bonnsai. One disadvantage of Bonnsai is the higher computing time than for the nitrogen chronology, what makes it time-consuming to evaluate a large samples of stars.

The general idea of deriving ages of stars using their observables can be applied to several different fields of astrophysics and other types of stars (like low mass stars or post main-sequence stars). The age constrain can be improved by using astroseismic data.

In Section 3 detailed stellar evolution models of rotating massive single stars on the main-sequence are presented. The grid contains stellar models of initial masses between 70 to 500 $M_{\odot}$ with initial surface rotational velocities of up to 550 km/s (0–550 km/s with velocity steps: 50 km/s). All stellar models are calculated assuming a metallicity adequate for the Large Magellanic Cloud (LMC).

The models presented in Section 3 are investigated further in Sanyal et al. (2015). Sanyal et al. (2015) shows that the presented stellar models exceed the Eddington limit in the outer envelope for all models initially more massive than 40 $M_{\odot}$, but almost never reach the Eddington limit at the surface. According to Sanyal et al. (2015), all the models presented in Section 3 show density inversion and envelope inflation, what leads to high mass loss. Stellar evolution models initially more massive than 125 $M_{\odot}$ reach the Eddington limit in their outer envelope already at the zero-age main-sequence.

The time steps in computation for the stellar evolution models presented in Section 3 is too high to resolve non-hydrostatic solutions. Sanyal et al. (2015) suggests that for smaller time steps the stellar models might show pulsations. These pulsations will likely not lead to the destruction or ejection of the envelope. Sanyal et al. (2015) discusses that inflation might be connected to S Doradus variability. Within the presented grid of stellar evolution models, stars of 40–100$M_{\odot}$ have the strongest inflation and hydrostatic equilibrium might be disturbed for these stars.

The effect of inflation on the radius of Wolf-Rayet (WR) stars and luminous blue variables (LBV) is studied in Gräfener et al. (2012). The radii of the presented stellar evolution models in Gräfener et al. (2012) with inflated envelopes (taking clumping into account) are in agreement with the radii of observed Wolf-Rayet stars. Gräfener et al. (2012) suggests that changes in the stellar rotation lead to instabilities causing S Doradus-type variability (LBVs).

Investigating whether inflation is observed in luminous massive star on the main sequence, will improve our understanding and the implementation in the stellar evolution

models. As the Eddington limit strongly affects the stellar evolution models on the main-sequence for luminous massive stars, it might be interesting how the Eddington limit influences other types of stars or evolutionary phases.

The evolution and fate of VMS is strongly effected by mass loss, in particular the evolution near the Eddington limit. The stellar evolution models of very massive stars presented in Section 3 loose a significant amount of mass during their main-sequence evolution. These stellar evolution models will not produce pair-instability supernovae. The quantitative comparison between observations and simulated populations of stars based on stellar evolution models will improve the understanding of mass loss in very massive stars.

In Section 3 the presented stellar models are compared in detail to the very massive stellar evolution models of Yusof et al. (2013). Furthermore, it should be mentioned that Yusof et al. (2013) only computed non-rotating very massive stellar models (120–500$M_{\odot}$) and models rotating at 40% critical velocity initially. Therefore these stellar evolution models are not suitable for simulating populations of rotating stars. Up until now, no very massive stellar evolution models assuming a metallicity adequate for the LMC are published that are usable for detailed simulations of synthetic populations of rotating stars, except for the ones presented in Section 3.

Synthetic populations of rotating very massive single stars are presented in Section 4. The simulations are based on stellar evolution models of Brott et al. (2011a) and the models introduced in Section 3 for a metallicity appropriate for the LMC. The population synthesis code Starmaker (Brott et al. 2011b) is used assuming different initial distribution functions for mass, age and surface rotational velocity.

Comparing the simulation result for continuous star formation history, with the stars observed in the VLT-Flames Tarantula survey (VFTS), it can be seen that the zero-age main-sequence including the predicted bending due to inflation is well followed by the stars of the VFTS sample. The slow rotating stellar evolution models presented in Section 3 penetrate below the Humphrey-Davidson (HD) limit. As the observational sample does not contain stars below this limit, the question arises whether the presented models contradict the observations. According to the simulated populations of stars, approximately 1% of stars (spectral type O2–O7, the exact value varies slightly with initial distributions of age, mass and rotational velocity) are expected below the HD limit. The observed number of stars near the HD limit is very low and the probability (according to the simulated populations of stars) is low to observe stars below this region. Therefore the comparison between the simulated populations and the observed stars near the HD limit is not generally in contradiction, but it is neither possible to argue in favour of an

agreement. Whether the stellar evolution models are going to penetrate the HD limit or not depends strongly on the mass loss prescription applied in the stellar models.

Sana et al. (2013a) derived a binary fraction of 35% for O-type stars in the VLT-Flames Tarantula Survey. Due to the large binary fraction it is important to take binaries into account in population synthesis calculations. de Mink et al. (2013) reproduced the observed low velocity peak and high velocity tail in the projected surface rotational velocity distribution of the VFTS sample, by assuming continuous star formation and a uniform initial surface rotational velocity distribution of low and moderate rotating stars ($v_{\rm rot} \leq 200\,$km/s), by taking binary interaction into account. de Mink et al. (2013) conclude that the high velocity tail in the projected surface rotational velocity distribution is likely caused by post-interacting binaries and the enhancement of the surface nitrogen abundance is primarily related to mass transfer instead of rotational mixing of rapidly rotating single stars.

Appendix A.

Nitrogen chronology of massive main sequence stars

A.1. Equations

A.1.1. Determining parameters a, b, c and d (Eq. (2.2)) for the example of the LMC metallicity

In this section, we derive the parameters a, b, c and d of Eq. (2.2). This is done for the example of the LMC grid of stellar evolution models presented in Brott et al. (2011a).

Our dataset of the stellar evolution models contains information about the time-evolution of the surface nitrogen abundance. We can derive the main sequence lifetime from our models and therefore obtain the surface nitrogen abundance as a function of the fraction of the main sequence lifetime.

The parameter a corresponds to the initial surface nitrogen abundance and is set to be the surface nitrogen abundance at $\tau = 0$, which for the LMC is given by the constant value

$$a = 6.9. \tag{A.1}$$

By fitting Eq. (2.2) to the data of the stellar evolution models of the LMC grid, we obtain the remaining three parameters for different masses and surface rotational velocities at the ZAMS.

In Fig. A.1, the fitted parameter b is shown as a function of v_{ZAMS} for several different initial masses. A polynomial function of second order reproduces the data for fixed mass well. The parameter b is therefore calculated as

$$b = b_1 \cdot v_{\mathrm{ZAMS}}^2 + b_2 \cdot v_{\mathrm{ZAMS}} + b_3.$$

Figure A.2 shows the coefficients b_1, b_2 and b_3 as a function of initial mass. They can be fitted well by linear approximations shown by the solid lines. Using $b_1(M)$, $b_2(M)$

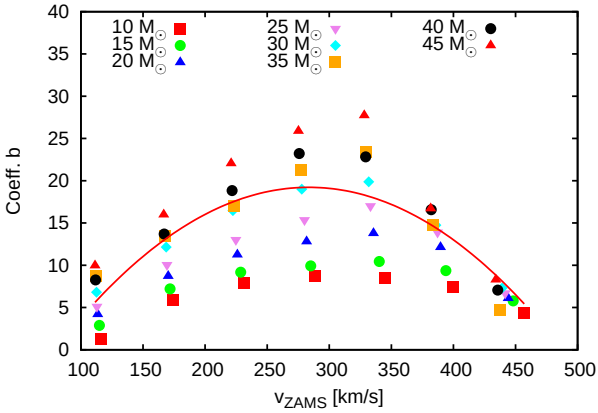

Figure A.1.: The parameter b is shown as a function of initial surface rotational velocity for several different masses, obtained by fitting Eq. (2.2) to the stellar evolution grid data (LMC). The solid line represents the best fit for the 30 $M_\odot$ models.

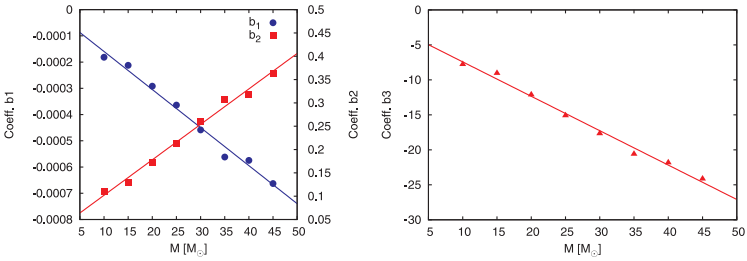

Figure A.2.: The three coefficients $b_1(M)$, $b_2(M)$ and $b_3(M)$ of the polynomial function to describe the parameter b are depicted as functions of mass. All parameters can be fitted well using linear functions which are plotted by solid lines.

and $b_3(M)$ the parameter $b\,(M\,[M_\odot]\,, v_{\rm ZAMS}\,[{\rm km/s}])$ can be calculated using

$$b = -\frac{M+4.6}{2.0} + (M+3.2)\cdot\frac{v_{\rm ZAMS}}{131} - (M+0.8)\cdot\left(\frac{v_{\rm ZAMS}}{263}\right)^2. \qquad \text{(A.2)}$$

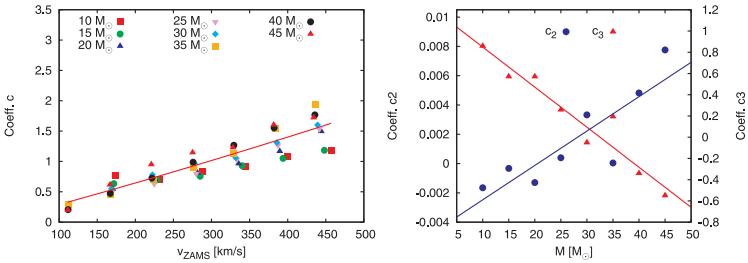

Figure A.3.: On the left panel, the parameter c is shown as a function of initial surface rotational velocity for several different masses. The line represents the best fit for the $30\,M_\odot$ model. On the right panel, the coefficients $c_2(M)$ and $c_3(M)$ are plotted as functions of the initial mass. They can be reproduced best using linear functions shown by solid lines.

Similarly we obtained parameter c as a function of initial mass and surface rotational velocity by fitting Eq. (2.2) to the data of the stellar model grids. The result is shown in Fig. A.3 on the left panel. The data is fitted well as a function of $v_{\rm ZAMS}$ using the polynomial function of second order

$$c = c_1 \cdot v_{\rm ZAMS}^2 + c_2 \cdot V_{\rm ZAMS} + c_3.$$

The coefficients c_1, c_2 and c_3 are obtained for different initial masses to consider a mass dependence.

In the case of LMC models the dataset seen on the left panel in Fig. A.3 can be reproduced well by a linear function. Therefore parameter $c_1(M)$ is set to zero. This is not the case for SMC and MW were the polynomial function need to be used.

Figure A.3 shows the mass dependent coefficients $c_2(M)$ and $c_3(M)$ which can be fitted well using linear functions shown by the solid lines. Using $c_1(M)$, $c_2(M)$ and $c_3(M)$, $c\,(M\,[M_\odot]\,, v_{\rm ZAMS}\,[km/s])$ can be calculated by

$$c = -\frac{M-29.5}{54} + (M+7.3)\cdot\frac{v_{\rm ZAMS}}{10455}. \qquad \text{(A.3)}$$

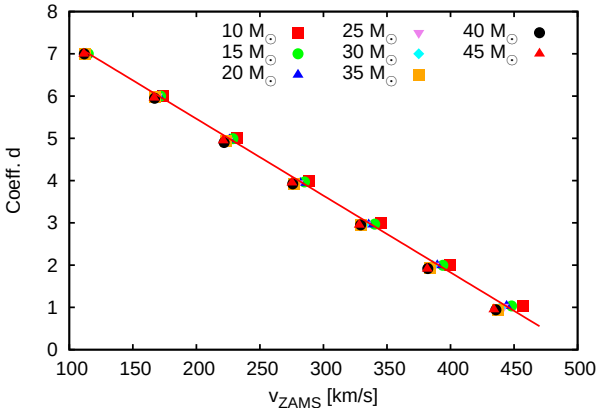

Figure A.4.: The parameter d is shown as a function of initial surface rotational velocity for several different masses, obtained by fitting Eq. (2.2) to the stellar evolution grid data (LMC). The line represents the best fit using a linear approximation. A small mass dependence can be seen, which will be neglected for simplification.

Parameter d is obtained for different masses and surface rotational velocities at the ZAMS. The resulting values are shown in Fig. A.4. It can be seen, that only a weak mass dependence exists in the case of our data. For simplification, we neglect the mass dependence. Therefore a linear approximation is used to describe parameter d as depicted in Fig. A.4, which can be described by

$$d = 9.1 - \frac{v_{\mathrm{ZAMS}}}{55}. \tag{A.4}$$

A.1.2. The main sequence lifetime and the surface rotational velocity

The fraction of the main sequence lifetime is used in Eq. (2.2) to calculate the surface nitrogen abundance. To be able to constrain the absolute age of the star it is necessary to know the time a star spends on the main sequence for given initial parameters.

We therefore derive a formula for the main sequence lifetime for stars of a given initial mass and surface rotational velocity with MW, LMC and SMC metallicity. Figure A.5 shows the main sequence lifetime as a function of the initial surface rotational velocity for the example of the LMC data for different initial masses. The higher the initial

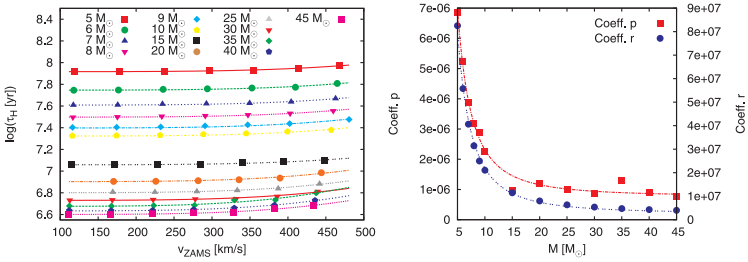

Figure A.5.: On the left panel the main sequence lifetime is shown as a function of the initial surface rotational velocity. Stellar evolution grid models for LMC metallicity are depicted for several different initial masses from 5 to 45 $M_\odot$. The data can be fitted well using Eq. (A.5) as shown by the additional lines. On the right panel the two coefficients p and r are depicted as a function of mass. The dotted lines represent the best fit using Eq. (A.6).

surface rotational velocity the higher the main sequence lifetime. Considering Fig. A.5 it is noticeable that the main sequence lifetime is a strong function of the initial mass, but shows only a weak dependence on the initial surface rotational velocity. The data can be fitted well using

$$\frac{\tau_\mathrm{H}}{\mathrm{yr}} = p \cdot (v_\mathrm{ZAMS})^q + r, \tag{A.5}$$

taking mass dependent parameters p, q and r into account. For reproducing the data best, q is chosen to be a linear function of mass, which in case of LMC and MW can be simplified to a constant value. p and r can be calculated depending on the initial mass. We therefore have

$$\begin{aligned} p &= p_1 \cdot M^{p_2} + p_3, \\ q &= q_1 \cdot M + q_3, \\ r &= r_1 \cdot M^{r_2} + r_3. \end{aligned}$$

By fitting the parameters p, q and r, we gain the following formula to calculate the main sequence lifetime:

$$\begin{aligned} \frac{\tau_\mathrm{H}}{\mathrm{yr}} &= \left(\frac{M^{-2} + 4.9804 \cdot 10^{-3}}{6.4689 \cdot 10^{3}} \right) \cdot (v_\mathrm{ZAMS})^{4.57} \\ &+ \frac{M^{-2} + 1.3251 \cdot 10^{-3}}{5.1564 \cdot 10^{-10}}. \end{aligned} \tag{A.6}$$

In our stellar evolution models, mass loss is included as described in Vink et al. (2010). During the main sequence evolution the stars loses angular momentum due to mass loss. The value of the surface rotational velocity therefore changes as a function of time. Figure A.6 depicts the surface rotational velocity of a few exemplary models as functions of time (left panel) and effective temperature $T_{\rm eff}$ (right panel). An initial surface rotational velocity of about 170 km/s is chosen.

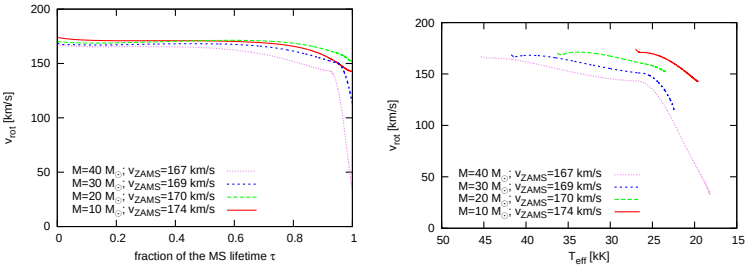

Figure A.6.: The evolution of the surface rotational velocity over time is shown on the left panel, while the surface rotational velocity as a function of the effective temperature is given on the right panel. Models of the stellar evolution grid in the case of LMC metallicity are used for different initial masses and surface rotational velocities of about 170 km/s.

During the evolution on the main sequence the surface rotational velocity of a star remains almost constant. At the end a sudden drop is visible for the highest considered masses, caused by an increase in mass loss and therefore a decrease of angular momentum when the effective temperature falls below 25 000 K, caused by the bi-stability braking (Vink et al. 2000, 2001). Stars with masses up to 30 $M_{\odot}$ reach the end of the main sequence at temperatures higher than 20 000 K (see Fig. A.6). They do not stay long enough on the main sequence at $T_{\rm eff} \leq 25000$ K to be significantly slowed down. In the case of stars more massive than 30 $M_{\odot}$ the assumption is valid for $T_{\rm eff} \geq 25000$ K. For stars which have not been influenced noticeably by this effect it is reasonable to estimate the surface rotational velocity by the value at the ZAMS.

A.1.3. Small Magellanic Cloud

For the SMC, the parameters specifying Eq. (2.2) are:

$$
\begin{aligned}
a &= 6.5, \\
b &= -\frac{M+0.9}{1.4} + (M+3.4)\cdot\frac{v_{\mathrm{ZAMS}}}{122} - (M+2.0)\cdot\left(\frac{v_{\mathrm{ZAMS}}}{262}\right)^2, \\
c &= -\frac{M-71}{67} + (M-40)\cdot\frac{v_{\mathrm{ZAMS}}}{18457} + (M+213)\cdot\left(\frac{v_{\mathrm{ZAMS}}}{6294}\right)^2, \\
d &= 9.0 - \frac{v_{\mathrm{ZAMS}}}{58},
\end{aligned}
$$

$$
\begin{aligned}
\frac{\tau_{\mathrm{H}}}{\mathrm{yr}} &= \left(\frac{M^{-5.85}}{8.5881\cdot 10^{-4}}\right)\cdot (v_{\mathrm{ZAMS}})^{0.1121\cdot M+2.4187} \\
&\quad + \frac{M^{-2.065} + 1.6507\cdot 10^{-3}}{5.0320\cdot 10^{-10}}.
\end{aligned}
$$

The formula to calculate the main sequence lifetime for SMC stars is valid for all stars analyzed, but not in the complete range given in Table 2.2. Table A.1 summarizes the mass and velocity ranges valid for this specific formula.

Table A.1.: Range of initial stellar parameters for which the main sequence lifetime calculation for SMC stars is validated.

v_{ZAMS} km/s	M $M_\odot$
0–50	5–50
50–100	5–30
100–225	5–21
225–350	5–15

A.1.4. Milky Way

For the MW, the parameters specifying Eq. (2.2) are:

$$
\begin{aligned}
a &= 7.64, \\
b &= -\frac{M+20.3}{4.0} + (M+10.3)\cdot\frac{v_{\mathrm{ZAMS}}}{204} - (M+9.9)\cdot\left(\frac{v_{\mathrm{ZAMS}}}{338}\right)^2, \\
c &= -\frac{M-86}{69} + (M-137)\cdot\frac{v_{\mathrm{ZAMS}}}{22561} + (M+240)\cdot\left(\frac{v_{\mathrm{ZAMS}}}{4737}\right)^2, \\
d &= 9.1 - \frac{v_{\mathrm{ZAMS}}}{53},
\end{aligned}
$$

$$\frac{\tau_{\mathrm{H}}}{\mathrm{yr}} = \left(\frac{M^{-2.05} + 2.3107 \cdot 10^{-3}}{1.6504 \cdot 10^{-1}}\right) \cdot (v_{\mathrm{ZAMS}})^{2.89} + \frac{M^{-2.35} + 1.1714 \cdot 10^{-3}}{2.6032 \cdot 10^{-10}}.$$

A.2. Dataset

star	number	$v \sin(i)$ km/s	$T_{\rm eff}$ K	$M_{\rm evol}$ $M_\odot$	$\mathcal{N}$ dex	$\tau_{\rm H}$ Myr	$\sin(i_{\rm N})$	$\sin(i_{\rm iso})$	$t_{\rm N}$ Myr	$t_{\rm isochrone}$ Myr	binary	class
N 11–34	L1	203	25500	20	7.12	7.5	1.00	–	$2.7^{+1.0}_{-1.5}$	7.8	yes	1
N 11–37	L2	100	28100	23	≤7.17	6.2	0.76	≥0.76	6.2	6.8	yes	2
N 11–46	L3	205	33500	28	≤7.71	5.1	0.88	≥0.88	$5.1_{-2.5}$	4.8	yes	2
N 11–77	L4	117	21500	12	6.96	16.0	0.90	0.89	$16.0_{-16.0}$	15.4	yes	2
N 11–88	L5	240	24150	14	≤6.96	12.6	1.00	–	$2.6^{+1.9}_{-2.6}$	12.6	–	1
N 11–89	L6	117	21700	12	6.91	16.0	1.00	–	$14.6^{+1.4}_{-14.6}$	16.4	yes	1
N 11–95	L7	267	26800	15	7.46	11.4	1.00	–	$4.9^{+2.4}_{-1.3}$	10.4	–	1
N 11–102	L8	218	31000	18	≤7.58	8.6	1.00	–	$6.6^{+2.0}_{-2.2}$	7.0	–	1
N 11–104	L9	153	25700	14	≤7.20	12.5	0.99	≥0.97	$12.5_{-4.2}$	11.8	–	2
N 11–111	L10	101	22950	12	6.93	16.0	0.83	0.81	$16.0_{-16.0}$	15.4	–	2
N 11–114	L11	299	32500	19	≤7.92	8.2	0.91	≥0.90	$8.2_{-4.7}$	5.8	–	2
N 11–116	L12	160	21700	11	6.98	18.6	1.00	–	$12.4^{+6.2}_{-12.4}$	18.4	–	1
N 11–117	L13	247	26800	13	≤7.06	14.2	1.00	–	$4.1^{+1.9}_{-4.1}$	11.2	–	1
N 11–118	L14	150	25700	13	7.39	14.1	0.83	0.79	14.1	12.6	yes	2
N 11–120	L15	207	31500	17	≤7.56	9.3	1.00	0.91	$8.2^{+1.1}_{-2.8}$	6.4	–	1
N 11–121	L16	265	27000	14	≤7.48	12.6	1.00	–	$6.1^{+3.4}_{-1.6}$	11.2	–	1
N 11–122	L17	173	33000	18	≤7.72	8.6	0.68	≥0.61	8.6	4.6	–	2
NGC 2004–20	L18	145	22950	18	7.46	8.6	0.83	0.83	8.6	9.6	yes	2
NGC 2004–30	L19	123	29000	19	7.43	7.9	0.71	0.71	7.9	7.6	yes	2
NGC 2004–47	L20	133	21700	12	7.03	16.0	0.94	0.94	$16.0_{-16.0}$	16.4	yes	2
NGC 2004–50	L21	109	20450	11	7.10	18.6	0.71	0.68	$18.6_{-18.6}$	17.0	yes	2
NGC 2004–54	L22	114	21700	12	6.97	16.0	0.86	0.86	$16.0_{-16.0}$	16.4	yes	2
NGC 2004–62	L23	106	31750	17	≤7.33	9.3	0.67	≥0.61	9.3	7.6	–	2
NGC 2004–63	L24	107	21700	11	6.97	18.6	0.79	0.79	$18.6_{-18.6}$	18.0	–	2
NGC 2004–65	L25	223	20450	11	≤7.19	18.7	1.00	–	$9.7^{+3.7}_{-3.6}$	19.8	–	1
NGC 2004–66	L26	238	25700	13	7.98	14.2	0.60	0.59	14.2	12.0	–	2
NGC 2004–69	L27	178	28000	15	7.84	11.2	0.57	0.56	11.2	9.8	–	2
NGC 2004–74	L28	130	27375	14	≤7.42	12.5	0.72	≥0.67	12.5	10.6	yes	2

NGC 2004–75	L29	116	21700	11	7.06	18.6	0.78	0.77	$18.4_{-18.6}$	18.0	–	2
NGC 2004–77	L30	215	29500	16	7.65	10.2	0.93	0.90	$10.2_{-3.6}$	8.4	–	2
NGC 2004–79	L31	165	21700	11	7.60	18.6	0.70	0.70	18.6	18.4	yes	2
NGC 2004–81	L32	105	26800	13	7.14	14.0	0.70	0.63	14.0	11.2	–	2
NGC 2004–82	L33	161	25700	13	7.47	14.1	0.83	0.79	14.1	12.6	–	2
NGC 2004–85	L34	150	20450	10	7.25	22.0	0.85	0.84	22.0	21.4	–	2
NGC 2004–88	L35	200	20450	10	≤7.18	22.0	1.00	–	$15.1^{+5.7}_{-5.7}$	21.6	yes	1
NGC 2004–95	L36	138	25700	13	7.13	14.1	0.92	0.89	$14.1_{-4.8}$	12.8	–	2
NGC 2004–99	L37	119	21700	10	7.06	22.0	0.78	0.74	$22.0_{-22.0}$	19.6	–	2
NGC 2004–100	L38	323	26800	13	≤7.29	14.5	1.00	–	$3.6^{+1.3}_{-1.2}$	11.6	–	1
NGC 2004–101	L39	131	21700	10	7.59	22.0	0.55	0.53	22.0	19.6	–	2
NGC 2004–104	L40	274	25700	12	≤7.28	16.3	1.00	–	$6.0^{+2.2}_{-1.8}$	13.2	–	1
NGC 2004–105	L41	235	25700	12	≤7.11	16.2	1.00	–	$6.1^{+2.5}_{-3.7}$	13.2	–	1
NGC 2004–107	L42	146	28500	14	≤7.12	12.5	1.00	0.88	$12.3^{+0.2}_{-6.2}$	9.4	yes	1
NGC 2004–110	L43	121	21700	10	6.95	22.0	0.91	0.87	$22.0_{-22.0}$	19.4	–	2
NGC 2004–113	L44	307	20450	9	≤7.29	27.1	1.00	–	$9.5^{+3.6}_{-3.1}$	22.2	–	1

Table A.2.: Properties of the analyzed LMC stars. From left to right: catalogue number (Evans et al. 2005), reference number used in this paper, projected surface rotational velocity, effective temperature, evolutionary mass and surface nitrogen abundance (all from Hunter et al. (2008b, 2009)), main sequence lifetime, nitrogen inclination angle, inclination angle derived using the nitrogen abundance and the isochrone age, maximum age based on the surface nitrogen abundance, isochrone age, identification of binarity and class. For Class 2 stars, adopting an error in the nitrogen abundance does not lead to an increased upper age limit, and in many cases also not to an decreased lower age limit.

star	number	$v \sin(i)$ km/s	$T_{\rm eff}$ K	$M_{\rm evol}$ $M_\odot$	$\mathcal{N}$ dex	$\tau_{\rm H}$ Myr	$\sin(i_{\rm N})$	$\sin(i_{\rm iso})$	$t_{\rm N}$ Myr	$t_{\rm isochrone}$ Myr	binary	class
NGC 346–27	S1	220	31000	18	≤7.71	9.7	0.57	≥0.57	9.7	7.6	–	2
NGC 346–32	S2	125	29000	17	≤6.88	9.1	0.85	≥0.85	9.1	9.2	yes	2
NGC 346–53	S3	170	29500	15	≤7.44	10.9	0.57	≥0.57	10.9	9.4	yes	2
NGC 346–55	S4	130	29500	15	≤7.25	10.9	0.64	≥0.58	10.9	9.4	–	2
NGC 346–58	S5	180	29500	14	≤7.56	12.0	0.51	≥0.51	12.0	9.6	yes	2
NGC 346–70	S6	109	30500	15	≤7.50	11.0	0.34	≥0.33	11.0	8.2	–	2
NGC 346–79	S7	293	29500	14	≤7.88	13.4	0.65	≥0.64	13.4	9.4	–	2
NGC 346–80	S8	216	27300	12	≤7.85	15.4	0.48	≥0.48	15.4	12.8	–	2
NGC 346–81	S9	255	21200	9	≤7.52	25.1	0.73	≥0.73	25.1	24.4	–	2
NGC 346–82	S10	168	21200	9	≤7.55	24.7	0.46	≥0.46	24.7	24.4	yes	2
NGC 346–83	S11	207	27300	12	≤7.73	15.3	0.50	≥0.50	15.3	12.8	yes	2
NGC 346–84	S12	105	27300	12	≤7.06	15.0	0.59	≥0.55	15.2	12.8	–	2
NGC 346–92	S13	234	27300	12	≤7.52	15.5	0.69	≥0.68	15.5	12.8	–	2
NGC 346–100	S14	183	26100	11	≤7.41	17.5	0.63	≥0.61	17.5	15.0	–	2
NGC 346–106	S15	142	27500	12	≤7.51	15.1	0.42	≥0.42	15.1	12.4	yes	2
NGC 346–108	S16	167	26100	11	≤7.42	17.4	0.56	≥0.55	17.4	15.0	–	2
NGC 346–109	S17	123	26100	11	≤7.09	17.4	0.67	≥0.62	17.4	15.0	–	2
NGC 346–114	S18	287	27300	12	≤7.80	16.0	0.66	≥0.65	16.0	12.6	–	2
NGC 330–21	S19	204	30500	21	≤7.64	9.2	0.57	≥0.57	9.2	7.0	–	2
NGC 330–38	S20	150	27300	14	≤7.16	11.9	0.81	≥0.79	11.9	11.2	–	2
NGC 330–39	S21	120	33000	18	≤7.61	8.4	0.34	≥0.34	8.4	6.4	–	2
NGC 330–40	S22	106	21200	11	≤7.12	17.4	0.56	≥0.56	17.4	20.6	–	2
NGC 330–41	S23	127	32000	17	7.73	9.1	0.32	0.32	9.1	7.2	–	2
NGC 330–45	S24	133	18450	9	≤7.28	24.6	0.56	≥0.56	24.6	29.0	yes	2
NGC 330–51	S25	273	26100	12	≤7.20	15.8	1.00	–	$8.7^{+7.1}_{-2.2}$	14.2	–	1
NGC 330–56	S26	108	21200	9	≤6.93	24.6	0.63	≥0.62	24.6	24.0	–	2
NGC 330–57	S27	104	29000	13	≤7.48	13.3	0.33	≥0.32	13.3	10.2	–	2
NGC 330–59	S28	123	19000	8	7.27	30.5	0.51	0.51	30.5	30.8	–	2

NGC 330–66	S29	126	18500	8	≤7.77	30.5	0.28	≥0.28	30.5	34.6	–	2
NGC 330–69	S30	193	19000	8	≤7.91	30.6	0.32	≥0.32	30.6	33.2	–	2
NGC 330–79	S31	146	19500	8	≤7.69	30.5	0.35	≥0.35	30.5	32.6	yes	2
NGC 330–83	S32	140	18000	7	≤7.66	39.1	0.34	≥0.34	39.1	39.8	–	2
NGC 330–97	S33	154	27300	11	7.60	17.4	0.41	0.40	17.4	12.0	–	2
NGC 330–110	S34	110	21200	8	7.23	30.4	0.48	0.48	30.4	30.0	–	2
NGC 330–120	S35	137	18500	6	≤7.85	52.5	0.28	≥0.28	52.5	46.8	–	2

Table A.3.: Properties of the analyzed SMC stars. From left to right: catalogue number (Evans et al. 2005), reference number used in this paper, projected surface rotational velocity, effective temperature, evolutionary mass and surface nitrogen abundance (all from Hunter et al. (2008b, 2009)), main sequence lifetime, nitrogen inclination angle, inclination angle derived using the nitrogen abundance and the isochrone age, maximum age based on the surface nitrogen abundance, isochrone age, identification of binarity and class. For Class 2 stars, adopting an error in the nitrogen abundance does not lead to an increased upper age limit, and in many cases also not to an decreased lower age limit.

Appendix B.

The evolution of rotating very massive stars with LMC composition

B.1. Isochrones

The evolution of our rapidly rotating stellar models is influenced significantly by rotation (see Sect. 3.3.1). Therefore, isochrones of rotating models calculated for the same age differ from isochrones of non-rotating models.

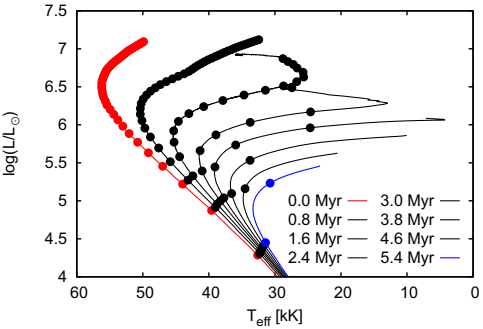

Figure B.1.: Isochrones of non-rotating stellar evolution models in the mass range 10 - 500 $M_{\odot}$ are depicted for ages up to 5.4 Myr. The different line colours explained in the figure key indicate the age of every isochrone. Models in 10 $M_{\odot}$-steps are highlighted by filled circles.

Figure B.1 depicts isochrones of non-rotating models for ages up to 5.4 Myr in the HR diagram. Eight different isochrones are shown with age steps of 0.8 Myr. The core hydrogen burning stellar evolution models presented in Sect. 2.3 are used to gen-

erate the isochrones. Because more massive stellar models have shorter lifetimes, older isochrones terminate at the less massive model at the upper end of the track.

For a given initial composition and age, isochrones span an area in the HR diagram when different initial surface rotational velocities are considered simultaneously (Brott et al. 2011a). Isochrones of 16 different ages from 0.2 to 6.2 Myr for rotating stellar models are shown in Fig. B.2 and B.3 for different ages. Switching from inhomogeneous to chemically homogeneous evolution, the isochrone is located at higher effective temperatures and luminosities than for the non-chemically homogeneous evolution.

The more massive a stellar model is, the earlier it reaches the point in the HR diagram where the stellar evolution track starts to evolve blueward. The related turn in the isochrones in Fig. B.2 is first visible for 1.4 Myr (bottom left panel). The minimum effective temperature depends on the surface rotational velocity at the ZAMS, which is reflected by the isochrones of different rotation rates. The 2.2 Myr and 2.6 Myr isochrones show that the more massive a stellar model is, the earlier the Hamann et al. (1995) mass-loss rate is applied to the stellar evolution calculation. The isochrones therefore show a decrease in luminosity for the most massive models.

Figure B.4 depicts a population synthesis of stars with the age and distributions of mass and surface rotational velocity given in Table B.1. The calculation was done using the code Starmaker (Brott et al. 2011b), using the parameters listed in Table A1.

Table B.1.: Parameters used in our population synthesis calculation (cf. Fig. B.4).

parameter	
age	1.5 Myr
velocity distribution	Gaussian distribution (Brott et al. 2011b)
	(σ = 141 km/s, μ=100 km/s)
velocity range	0 – 500 km/s
mass distribution	uniform distribution
mass range	10 – 500 $M_\odot$

It can be seen that the randomly drawn stellar models with the same age do not lie on one line, but instead spread over a certain area in the HR diagram. The initial mass distribution determines the model density along the line corresponding to the isochrone of non-rotating stellar models of this age. We choose a flat mass distribution for the simulation to have a better view of the behaviour of the most massive stars. The velocity distribution on the other hand shapes the stellar model density as a function of the effective temperature for (roughly) constant luminosity. The colour coding indicates the number of stars within one pixel of 500 K and $\log(L/L_\odot)$=0.05.

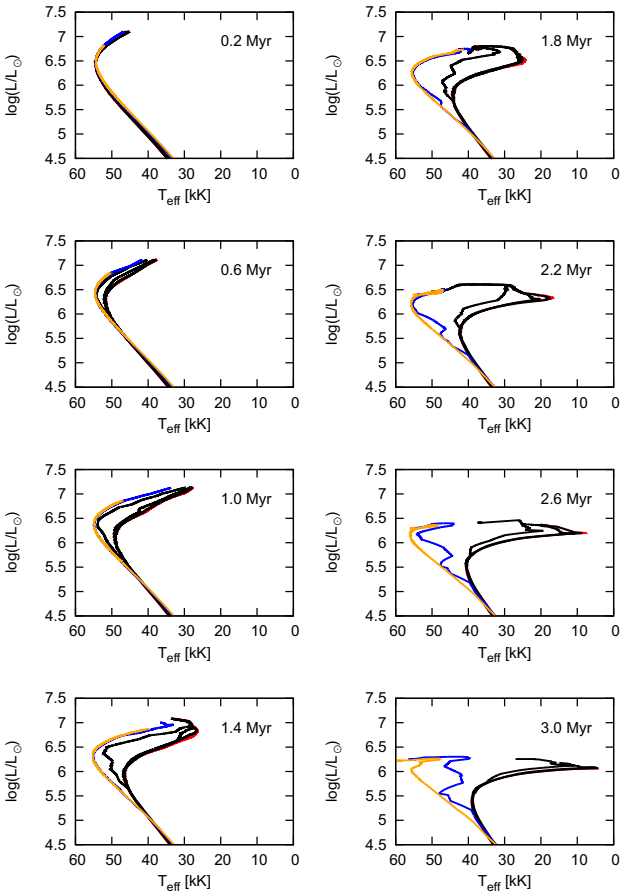

Figure B.2.: Several isochrones of different ages and rotating stellar evolution models are shown in the HR diagram. The surface rotational velocity at the ZAMS is chosen in steps of 100 km/s from non-rotating to 400 km/s and additionally 450 km/s. Three initial surface rotational velocities are highlighted in particular. The isochrones of non-rotating models are shown in red, 400 km/s in blue, and 450 km/s in orange.

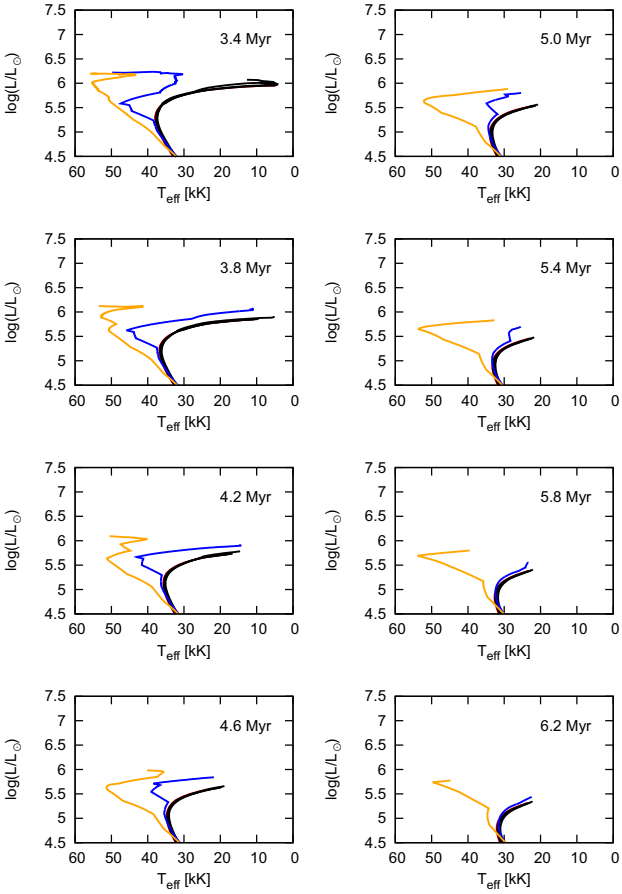

Figure B.3.: Several isochrones of different ages and rotating stellar evolution models are shown in the HR diagram. The surface rotational velocity at the ZAMS is chosen in steps of 100 km/s from non-rotating to 400 km/s and additionally 450 km/s. Three initial surface rotational velocities are highlighted. The isochrones of non-rotating models are shown in red, 400 km/s in blue, and 450 km/s in orange.

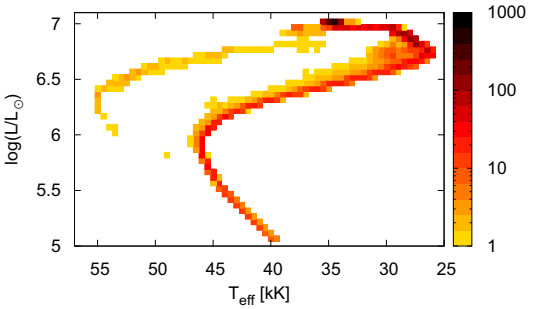

Figure B.4.: STARMAKER population-synthesis calculation for 1.5 Myr (and other parameters as explained in Table B.1). The luminosity is depicted as a function of the effective temperature. The colour coding explained at the right bar indicates the number of stars within one pixel of 500 K and $\log(L/L_{\odot})$=0.05.

Figure B.4 shows similar information as discussed in Fig. B.2. Additionally, it gives the probability of observing a star for the conditions given in Table B.1 depending on the surface rotational velocity distribution.

Isochrones for slow rotating stellar evolution models that undergo non-chemically homogeneous evolution do not differ significantly in the HR diagram. The probability of observing a star along these isochrones is highest. The change from non-chemically homogeneous to quasi-chemically homogeneous evolution occurs at a small velocity range related to a significant change of the position in the HR diagram.Therefore, the probability of observing a star between isochrones of slow-rotating and rapidly rotating models is small. Again, isochrones of rapidly rotating stellar evolution models are close in the HR diagram, leading to a higher probability of observation.

B.2. Summary of data

M_i	$v_{rot,i}$	τ_{MS}	$\log L_i/L_\odot$	$T_{eff,i}$	$M_{conv,i}$	$M_{over,i}$	$M_{conv,0.2}$	$M_{over,0.2}$	M_f	$v_{rot,f}$	$Y_{s,f}$	$Y_{c,f}$	$\log L_f/L_\odot$	$T_{eff,f}$	j
$M_\odot$	km/s	Myr		K	$M_\odot$	$M_\odot$	$M_\odot$	$M_\odot$	$M_\odot$	km/s				K	10^{15} cm^2/s
60	0	3.373	5.704	50000	42.6	-	30.7	-	43	0	0.393	0.995	6.022	6600	0
60	220	3.407	5.701	49500	43.8	-	30.7	-	42	0	0.398	0.995	6.023	8800	89
60	273	3.464	5.699	49200	43.6	-	30.8	-	42	0	0.384	0.995	6.023	5600	89
60	326	3.619	5.698	48900	43.5	3.0	32.4	2.6	45	1	0.418	0.995	6.056	14200	85
60	379	3.676	5.694	48600	43.4	3.1	32.7	2.6	45	1	0.412	0.995	6.061	14800	84
60	432	4.038	5.691	48300	43.3	3.1	38.6	2.1	45	518	0.677	0.995	6.133	38900	237
60	532	4.167	5.684	47600	43.0	3.2	40.4	1.6	38	383	0.865	0.995	6.098	69600	212
100	0	2.648	6.102	54100	80.6	3.8	57.2	3.8	68	0	0.636	0.993	6.336	17600	0
100	217	2.692	6.099	53700	82.1	3.6	57.4	3.7	66	1	0.674	0.991	6.331	22200	98
100	271	2.740	6.098	53500	81.9	3.5	58.2	3.7	65	12	0.722	0.993	6.337	27800	97
100	323	2.817	6.096	53200	81.7	4.3	60.1	3.5	67	7	0.720	0.993	6.354	26400	105
100	375	2.973	6.094	53000	81.6	3.5	66.3	2.6	61	64	0.929	0.991	6.345	47700	130
100	426	3.016	6.093	52700	81.4	3.5	66.3	2.2	50	39	0.974	0.993	6.236	58900	88
100	524	3.065	6.088	52100	81.0	3.7	66.1	1.8	46	64	0.975	0.995	6.213	73000	83
150	0	2.313	6.382	56000	131.6	3.7	91.3	4.4	94	0	0.839	0.975	6.553	30200	0
150	216	2.339	6.381	55600	131.3	4.1	91.5	4.4	94	4	0.836	0.973	6.553	30200	121
150	268	2.417	6.380	55400	131.1	3.7	95.4	4.2	99	11	0.821	0.966	6.573	28900	144
150	320	2.465	6.378	55200	130.9	3.8	97.9	3.5	91	17	0.931	0.966	6.550	41100	139
150	371	2.544	6.377	55000	130.7	3.9	98.0	2.3	57	15	0.978	0.991	6.313	55000	47
150	421	2.557	6.376	54700	130.6	3.8	96.8	2.1	55	17	0.979	0.993	6.300	56400	48
150	514	2.579	6.372	54200	130.2	3.9	95.3	2.1	55	17	0.977	0.991	6.293	55600	51
200	0	2.140	6.567	56200	181.5	3.9	126.1	4.7	131	0	0.809	0.916	6.698	30700	0
200	214	2.155	6.566	55800	181.1	4.0	125.4	4.7	126	9	0.843	0.927	6.693	32300	159
200	267	2.185	6.565	55600	180.9	3.9	126.7	5.6	133	8	0.792	0.912	6.700	30300	190
200	318	2.255	6.564	55400	180.7	4.0	130.2	3.8	70	2	0.986	0.995	6.436	51100	37
200	367	2.291	6.563	55300	180.6	3.9	129.1	2.8	64	3	0.985	0.995	6.383	53800	37
200	415	2.302	6.562	55100	180.4	4.1	127.6	2.3	65	2	0.980	0.991	6.387	50900	41
200	502	2.334	6.560	54700	179.8	4.1	121.7	2.1	62	6	0.979	0.991	6.362	52400	43
300	0	1.979	6.811	54500	281.1	4.7	195.3	4.7	82	0	0.988	0.993	6.519	46800	0
300	213	2.003	6.810	54300	280.6	3.8	193.4	4.9	80	1	0.988	0.993	6.509	47300	17

300	264	2.023	6.810	54200	280.6	3.8	193.7	4.7	80	1	0.988	0.993	6.507	47600	17
300	313	2.037	6.809	54100	280.6	3.8	193.7	4.7	79	1	0.987	0.995	6.505	48100	18
300	359	2.062	6.808	54000	280.2	4.0	191.8	3.2	75	1	0.987	0.993	6.473	49500	19
300	403	2.076	6.807	53800	280.2	4.0	187.0	1.7	73	1	0.986	0.993	6.459	49800	21
300	475	2.099	6.806	53600	279.8	3.9	173.6	2.0	70	2	0.987	0.995	6.447	58900	24
500	0	1.855	7.097	49800	480.3	4.3	289.0	2.7	88	0	0.989	0.993	6.563	44900	0
500	210	1.885	7.096	49700	480.3	4.3	283.1	2.4	86	0	0.988	0.993	6.551	45300	7
500	259	1.883	7.096	49700	479.9	4.7	282.9	2.1	86	0	0.988	0.993	6.550	45700	7
500	304	1.894	7.096	49600	478.6	4.9	280.8	2.3	86	0	0.988	0.993	6.549	45200	7
500	344	1.900	7.096	49500	476.8	4.7	359.1	7.7	400	345	0.534	0.659	7.134	29200	1077
500	379	1.922	7.095	49500	476.8	4.7	360.1	6.9	398	342	0.546	0.652	7.131	31500	1201
500	420	1.936	7.095	49400	476.3	4.8	354.7	5.0	380	154	0.609	0.676	7.129	33100	1051

Table B.2.: Summary of important stellar characteristics. From left to right: Mass and surface rotational velocity at the ZAMS (index i); main-sequence lifetime; luminosity and effective temperature at the ZAMS; mass of the convective core and the overshoot zone at the first calculated model after the ZAMS and when hydrogen in the core drops below 0.2; mass, surface rotational velocity, helium mass fraction at the surface and in the core, luminosity, effective temperature; and surface specific angular momentum at the end of the main sequence evolution (index f). Several stellar evolution models have not been calculated until the TAMS. In these cases, the main sequence lifetime is extrapolated until the exhaustion of hydrogen in the core and the final values in Cols. 6 – 16 correspond to the last calculated values. Dashes in the table indicate data which is not available.

Appendix C.

Simulating populations of very massive rotating stars in the Large Magellanic Cloud (LMC)

C.1. Observational sample: summary of data

Star-ID	SpT	$\log L_i/L_\odot$	$T_{\rm eff}$	$\log g$	$v\sin(i)$	$Y(He)$
			K		km/s	
VFTS-072	O2	6.07	54000	4	185	0.25
VFTS-089	O6.5	5.09	39700	4.02	50	0.25*
VFTS-096	O6	5.67	40100	3.9	125	0.25*
VFTS-110	O6	5.4	39850	3.86	175	0.25*
VFTS-117	O6	5.02	41300	4.14	75	0.25*
VFTS-123	O6.5	4.99	40400	4.1	65	0.25*
VFTS-169	O2.5	5.91	47000	3.9	200	0.25
VFTS-216	O4	5.83	43000	3.8	100	0.25
VFTS-285	O7.5	4.77	35280	3.63	600	0.25*
VFTS-355	O4	5.52	43360	3.84	135	0.25*
VFTS-356	O6	5.14	39250	3.99	215	0.25*
VFTS-380	O6-7	4.92	39120	4.13	65	0.25*
VFTS-382	O4-5	5.31	40000	3.8	75	0.25*
VFTS-385	O4-5	5.55	42900	3.86	120	0.25*
VFTS-392	O6-7	5.11	37560	3.87	40	0.25*
VFTS-398	O5.5	5.47	41170	4.03	65	0.25*
VFTS-410	O7-8	5.14	34000	3.8	40	0.25*
VFTS-418	O5	5.24	43220	4.09	135	0.25*
VFTS-435	O7-8	5.12	36000	3.9	80	0.25*
VFTS-436	O7-8	4.87	35000	3.9	60	0.25*
VFTS-468	O2	6.17	52000	4.2	80	0.25
VFTS-470	O6	4.97	39330	3.93	75	0.25*
VFTS-472	O6	5.01	40365	4.12	40	0.25*

VFTS-484	O6-7	5.41	35680	3.67	120	0.25*
VFTS-488	O6	5.33	40700	3.87	55	0.25*
VFTS-491	O6	5.43	40360	3.84	50	0.25*
VFTS-506	ON2	6.43	55000	4.2	100	0.25
VFTS-511	O5	5.46	43700	4.27	105	0.25*
VFTS-536	O6	5.19	41500	4.24	40	0.25*
VFTS-537	O5	5.19	39000	3.8	60	0.25*
VFTS-549	O6.5	5.09	39760	4.04	110	0.25*
VFTS-550	O5	5.2	39000	3.8	50	0.25*
VFTS-564	O6-8	5.33	37000	4.1	40	0.25*
VFTS-577	O6	5.21	42000	4	40	0.25*
VFTS-581	O4-5	5.38	40000	3.7	70	0.25*
VFTS-586	O4	5.42	45000	4	100	0.25*
VFTS-601	O5-6	5.55	40275	3.93	125	0.25*
VFTS-621	O2	6.22	54000	4.2	80	0.25
VFTS-648	O5.5	5.66	40000	3.8	55	0.25*
VFTS-706	O6-7	5.02	38030	3.8	375	0.25*
VFTS-722	O7	4.91	36640	3.84	405	0.25*
VFTS-724	O7	5.01	37600	3.78	370	0.25*
VFTS-746	O6	5.29	39885	3.86	275	0.25*
VFTS-751	O7-8	5.01	36045	3.9	360	0.25*
VFTS-755	O3	5.65	46000	3.9	285	0.25
VFTS-761	O6.5	4.99	40280	4.15	110	0.25*
VFTS-770	O7	4.98	37815	3.95	350	0.25*
VFTS-797	O3.5	5.6	45000	3.8	140	0.25
VFTS-849	O7	5.02	39800	4.16	95	0.25*
VFTS-016	O2	6.16	52000	4.07	104	0.25
VFTS-064	O7.5	5.71	34700	3.75	128	0.25
VFTS-151	O6.5	5.88	37600	3.77	118	0.4
VFTS-180	O3	5.9	41750	3.6	108	0.55
VFTS-185	O7.5	5.31	35050	3.51	124	0.25*
VFTS-244	O5	5.49	37950	3.65	222	0.25*
VFTS-259	O6	5.96	35250	3.44	98	0.325
VFTS-267	O3	5.88	41050	3.7	200	0.25
VFTS-440	O6	5.66	34250	3.5	144	0.25
VFTS-513	O6-7	4.93	36600	4.16	114	0.25*
VFTS-599	O3	6.16	52650	4.13	120	0.25

VFTS-664	O7	5.51	35000	3.63	96	0.25
VFTS-108	WN7h	5.7	53089	-	<200	0.78
VFTS-145	-	5.87	39811	-	93	0.4
VFTS-147	-	5.83	42462	-	<200	0.7
VFTS-208	-	5.64	37584	-	271	0.33
VFTS-402	-	5.92	46452	-	<200	0.85
VFTS-406	-	5.48	37584	-	356	0.33
VFTS-422	-	5.7	39811	-	356	0.25
VFTS-427	-	6.13	41687	-	<200	0.93
VFTS-457	O3.5	6.2	39811	-	<200	0.4
VFTS-482	O2.5	6.4	42170	-	<200	0.33
VFTS-509	-	6.43	42170	-	<200	0.78
VFTS-542	O2	6.16	44668	-	<200	0.47
VFTS-545	O2	6.3	47315	-	<200	0.25
VFTS-566	-	5.85	44668	-	91	0.25
VFTS-617	WN5ha	6.29	53088	-	<200	0.62
VFTS-626	-	5.6	39811	-	278	0.4
VFTS-682	WN5h	6.51	54450	-	<200	0.45
VFTS-695	WN6h	6.5	39811	-	<200	0.85
VFTS-758	WN5h	6.36	47315	-	<200	0.78
VFTS-1001	WN6	6.2	42170	-	<200	0.85
VFTS-1017	O2	6.21	50119	-	<200	0.55
VFTS-1021	-	6.34	42267	-	<200	0.25
VFTS-1022	O3.5	6.48	42170	-	<200	0.25
VFTS-1025	WN5h	6.58	42170	-	<200	0.7
MK42	O2	6.56	47315	-	<200	0.33

Table C.1.: Data of the observational sample. From left to right: Star-ID, spectral type, luminosity, effective temperature, surface gravity, projected surface rotational velocity and helium mass fraction. Dashes in the table indicate data which is not available. In case no helium mass fraction is provided (value labelled with *) we assume $Y(He) = 0.25$ if the helium number fraction does not indicate enhancement at the surface.

Bibliography

Abbott, D. C. 1982, ApJ, 259, 282

Arnault, P., Kunth, D., & Schild, H. 1989, A&A, 224, 73

Bally, J., Moeckel, N., & Throop, H. 2005, 341, 81

Belkus, H., Van Bever, J., & Vanbeveren, D. 2007, ApJ, 659, 1576

Bestenlehner, J. M., Gräfener, G., Vink, J. S., et al. 2014, A&A, 570, A38

Bjorkman, J. E. & Cassinelli, J. P. 1993, ApJ, 409, 429

Böhm-Vitense, E. 1958, Zap, 46, 108

Bond, J. R., Arnett, W. D., & Carr, B. J. 1984, ApJ, 280, 825

Bonnell, I. A., Bate, M. R., Clarke, C. J., & Pringle, J. E. 2001, MNRAS, 323, 785

Bonnell, I. A., Clarke, C. J., & Bate, M. R. 2006, MNRAS, 368, 1296

Bonnell, I. A. & Smith, R. J. 2011, in IAU Symposium, Vol. 270, Computational Star Formation, ed. J. Alves, B. G. Elmegreen, J. M. Girart, & V. Trimble, 57–64

Bonnell, I. A., Vine, S. G., & Bate, M. R. 2004, MNRAS, 349, 735

Bouret, J.-C. 2004, in EAS Publications Series, Vol. 13, EAS Publications Series, ed. M. Heydari-Malayeri, P. Stee, & J.-P. Zahn, 271–291

Bouret, J.-C., Hillier, D. J., Lanz, T., & Fullerton, A. W. 2012, A&A, 544, A67

Bouret, J.-C., Lanz, T., & Hillier, D. J. 2005, A&A, 438, 301

Brandl, B., Sams, B. J., Bertoldi, F., et al. 1996, ApJ, 466, 254

Braun, H. & Langer, N. 1995, A&A, 297, 483

Bresolin, F., Crowther, P. A., & Puls, J., eds. 2008, IAU Symposium, Vol. 250, Massive Stars as Cosmic Engines

Bressert, E., Bastian, N., Evans, C. J., et al. 2012, ArXiv e-prints

Brott, I., de Mink, S. E., Cantiello, M., et al. 2011a, AAP, 530, A115

Brott, I., Evans, C. J., Hunter, I., et al. 2011b, A&A, 530, A116

Buonanno, R. 1986, Mem. Soc. Astron. Italiana, 57, 333

Cantiello, M., Langer, N., Brott, I., et al. 2009, A&A, 499, 279

Castor, J. I., Abbott, D. C., & Klein, R. I. 1975, ApJ, 195, 157

Cerviño, M. & Mas-Hesse, J. M. 1994, A&A, 284, 749

Cesaroni, R., Galli, D., Lodato, G., Walmsley, C. M., & Zhang, Q. 2007, Protostars and Planets V, 197

Cesaroni, R., Galli, D., Lodato, G., Walmsley, M., & Zhang, Q. 2006, Natur, 444, 703

Charbonnel, C., Meynet, G., Maeder, A., Schaller, G., & Schaerer, D. 1993, A&AS, 101, 415

Chieffi, A. & Limongi, M. 2013, ApJ, 764, 21

Crowther, P. A. & Dessart, L. 1998, MNRAS, 296, 622

Crowther, P. A., Schnurr, O., Hirschi, R., et al. 2010, MNRAS, 408, 731

Crowther, P. A. & Smith, L. J. 1997, A%A, 320, 500

Crowther, P. A. & Walborn, N. R. 2011, MNRAS, 416, 1311

de Koter, A., Heap, S. R., & Hubeny, I. 1998, ApJ, 509, 879

de Mink, S. E., Langer, N., & Izzard, R. G. 2011, Bulletin de la Societe Royale des Sciences de Liege, 80, 543

de Mink, S. E., Langer, N., Izzard, R. G., Sana, H., & de Koter, A. 2013, ApJ, 764, 166

de Mink, S. E., Sana, H., Langer, N., Izzard, R. G., & Schneider, F. R. N. 2014, ApJ, 782, 7

Dufton, P. L., Langer, N., Dunstall, P. R., et al. 2013, A&A, 550, A109

Dufton, P. L., Smartt, S. J., Lee, J. K., et al. 2006, A&A, 457, 265

Eggenberger, P., Meynet, G., & Maeder, A. 2009, Communications in Asteroseismology, 158, 87

Eichler, D., Bar Shalom, A., & Oreg, J. 1995, ApJ, 448, 858

Ekström, S., Georgy, C., Eggenberger, P., et al. 2012, A&A, 537, A146

Endal, A. S. & Sofia, S. 1978, ApJ, 220, 279

Evans, C. J., Bastian, N., Beletsky, Y., et al. 2010, in IAU Symposium, Vol. 266, IAU Symposium, ed. R. de Grijs & J. R. D. Lépine, 35–40

Evans, C. J., Lennon, D. J., Smartt, S. J., & Trundle, C. 2006, A&A, 456, 623

Evans, C. J., Smartt, S. J., Lee, J.-K., et al. 2005, A&A, 437, 467

Evans, C. J., Taylor, W. D., Hénault-Brunet, V., et al. 2011, A&A, 530, A108+

Figer, D. F. & Kim, S. S. 2002, in Astronomical Society of the Pacific Conference Series, Vol. 263, Stellar Collisions, Mergers and their Consequences, ed. M. M. Shara, 287

Fitzpatrick, E. L. & Garmany, C. D. 1990, ApJ, 363, 119

Fliegner, J., Langer, N., & Venn, K. A. 1996, A&A, 308, L13

Foellmi, C., Moffat, A. F. J., & Guerrero, M. A. 2003, MNRAS, 338, 1025

Freitag, M., Gürkan, M. A., & Rasio, F. A. 2006, MNRAS, 368, 141

Fryer, C. L., Woosley, S. E., & Heger, A. 2001, ApJ, 550, 372

Fullerton, A. W., Massa, D. L., & Prinja, R. K. 2006, ApJ, 637, 1025

Garmany, C. D. & Conti, P. S. 1985, ApJ, 293, 407

Goldreich, P. & Kumar, P. 1990, ApJ, 363, 694

Gräfener, G. & Hamann, W.-R. 2008a, A&A, 482, 945

Gräfener, G. & Hamann, W.-R. 2008b, in IAU Symposium, Vol. 250, IAU Symposium, ed. F. Bresolin, P. A. Crowther, & J. Puls, 63–70

Gräfener, G., Owocki, S. P., & Vink, J. S. 2012, A&A, 538, A40

Gräfener, G. & Vink, J. S. 2013, A&A, 560, A6

Gräfener, G., Vink, J. S., de Koter, A., & Langer, N. 2011, A&A, 535, A56

Gürkan, M. A., Freitag, M., & Rasio, F. A. 2004, ApJ, 604, 632

Hamann, W.-R., Koesterke, L., & Wessolowski, U. 1995, A&A, 299, 151

Heap, S. R., Lanz, T., & Hubeny, I. 2006, ApJ, 638, 409

Heger, A. & Langer, N. 1996, A&A, 315, 421

Heger, A. & Langer, N. 2000, ApJ, 544, 1016

Heger, A., Langer, N., & Woosley, S. E. 2000, ApJ, 528, 368

Heger, A. & Woosley, S. E. 2002, ApJ, 567, 532

Heger, A., Woosley, S. E., Fryer, C. L., & Langer, N. 2003, in From Twilight to Highlight: The Physics of Supernovae, ed. W. Hillebrandt & B. Leibundgut, 3–540

Hénault-Brunet, V., Evans, C. J., Taylor, W. D., Gieles, M., & VLT-FLAMES Tarantula Consortium. 2011, Bulletin de la Societe Royale des Sciences de Liege, 80, 376

Hubeny, I. & Lanz, T. 1995, ApJ, 439, 875

Humphreys, R. M. & Davidson, K. 1994, PASP, 106, 1025

Hunter, I., Brott, I., Langer, N., et al. 2009, A&A, 496, 841

Hunter, I., Brott, I., Lennon, D. J., et al. 2008a, ApJ, 676, L29

Hunter, I., Dufton, P. L., Smartt, S. J., et al. 2007, A&A, 466, 277

Hunter, I., Lennon, D. J., Dufton, P. L., et al. 2008b, A&A, 479, 541

Ishii, M., Ueno, M., & Kato, M. 1999, PASJ, 51, 417

Jia, J. 2002, The Turn Off Luminosity and the Age of the Globular Clusters

Jijina, J. & Adams, F. C. 1996, ApJ, 462, 874

Joss, P. C., Salpeter, E. E., & Ostriker, J. P. 1973, ApJ, 181, 429

Kato, M. 1986, Ap&SS, 119, 57

Kennicutt, Jr., R. C. 1998, A&A, 36, 189

Kippenhahn, R. & Weigert, A. 1990, Stellar Structure and Evolution

Köhler, K., Borzyszkowski, M., Brott, I., Langer, N., & de Koter, A. 2012, A&A, 544, A76

Köhler, K., Langer, N., de Koter, A., et al. 2015, A&A, 573, A71

Kozyreva, A., Blinnikov, S., Langer, N., & Yoon, S.-C. 2014, A&A, 565, A70

Krumholz, M. R. & Bonnell, I. A. 2007, ArXiv e-prints

Krumholz, M. R., Klein, R. I., McKee, C. F., Offner, S. S. R., & Cunningham, A. J. 2009, Science, 323, 754

Kudritzki, R.-P. & Puls, J. 2000, ARA&A, 38, 613

Lamers, H. J. G. L. M. & Cassinelli, J. P. 1999, Introduction to Stellar Winds

Lamers, H. J. G. L. M., Snow, T. P., & Lindholm, D. M. 1995, ApJ, 455, 269

Langer, N. 1989, A&A, 210, 93

Langer, N. 1991, A&A, 252, 669

Langer, N. 1992, A&A, 265, L17

Langer, N. 1997, in Astronomical Society of the Pacific Conference Series, Vol. 120, Luminous Blue Variables: Massive Stars in Transition, ed. A. Nota & H. Lamers, 83

Langer, N. 1998, A&A, 329, 551

Langer, N. 2012, ARA&A, 50, 107

Langer, N., Cantiello, M., Yoon, S., et al. 2008, in IAU Symposium, Vol. 250, IAU Symposium, ed. F. Bresolin, P. A. Crowther, & J. Puls, 167–178

Langer, N., Fricke, K. J., & Sugimoto, D. 1983, A&A, 126, 207

Langer, N., Hamann, W.-R., Lennon, M., et al. 1994, A&A, 290, 819

Langer, N. & Kudritzki, R. P. 2014, A&A, 564, A52

Langer, N., Norman, C. A., de Koter, A., et al. 2007, A&A, 475, L19

Leitherer, C. & Ekstrom, S. 2011, ArXiv e-prints

Lennon, D. J., Evans, C. J., Bastian, N., et al. 2011, 272, 296

Lucy, L. B. & Abbott, D. C. 1993, ApJ, 405, 738

Maeder, A. 1981, A&A, 102, 401

Maeder, A. 1987, A&A, 178, 159

Maeder, A. 1991, A&A, 242, 93

Maeder, A. 1998, 131, 85

Maeder, A. 2000, New A Rev., 44, 291

Maeder, A. & Meynet, G. 2000a, A&A, 361, 159

Maeder, A. & Meynet, G. 2000b, ARA&A, 38, 143

Maeder, A. & Meynet, G. 2001, A&A, 373, 555

Maeder, A. & Meynet, G. 2008a, 388, 3

Maeder, A. & Meynet, G. 2008b, 33, 38

Maeder, A. & Meynet, G. 2011, ArXiv e-prints

Maeder, A. & Meynet, G. 2012, Reviews of Modern Physics, 84, 25

Maeder, A. & Meynet, G. 2015, in IAU Symposium, Vol. 307, IAU Symposium, ed. G. Meynet, C. Georgy, J. Groh, & P. Stee, 9–19

Maeder, A., Meynet, G., & Hirschi, R. 2005, 332, 3

Maeder, A. & Zahn, J.-P. 1998, A&A, 334, 1000

Markova, N., Evans, C. J., Bastian, N., et al. 2011, Bulgarian Astronomical Journal, 15, 29

Massey, P. 2003, ARA&A, 41, 15

Massey, P. & Hunter, D. A. 1998, ApJ, 493, 180

McKee, C. F. & Tan, J. C. 2003, ApJ, 585, 850

McWilliam, A. & Rauch, M. 2004, Origin and Evolution of the Elements

Meynet, G. 1995, A&A, 298, 767

Meynet, G., Ekström, S., & Maeder, A. 2006, 314

Meynet, G. & Maeder, A. 1997, A&A, 321, 465

Meynet, G. & Maeder, A. 2000, A&A, 361, 101

Meynet, G. & Maeder, A. 2002, A&A, 390, 561

Meynet, G. & Maeder, A. 2003, A&A, 404, 975

Meynet, G., Maeder, A., Schaller, G., Schaerer, D., & Charbonnel, C. 1994, A&AS, 103, 97

Mokiem, M. R., de Koter, A., Evans, C. J., et al. 2007, A&A, 465, 1003

Mokiem, M. R., de Koter, A., Evans, C. J., et al. 2006, A&A, 456, 1131

Muijres, L. E., Vink, J. S., de Koter, A., Müller, P. E., & Langer, N. 2012, A&A, 537, A37

Müller, P. E. & Vink, J. S. 2008, A&A, 492, 493

Müller, P. E. & Vink, J. S. 2014, A&A, 564, A57

Nakano, T. 1989, ApJ, 345, 464

Nieuwenhuijzen, H. & de Jager, C. 1990, A&A, 231, 134

Nugis, T. & Lamers, H. J. G. L. M. 2000, A&A, 360, 227

Pauldrach, A., Puls, J., & Kudritzki, R. P. 1986, A&A, 164, 86

Pauldrach, A. W. A., Vanbeveren, D., & Hoffmann, T. L. 2012, A&A, 538, A75

Petrovic, J., Langer, N., Yoon, S.-C., & Heger, A. 2005, A&A, 435, 247

Petrovic, J., Pols, O., & Langer, N. 2006, A&A, 450, 219

Pols, O. 2009, Stellar Structure and Evolution, lecture notes

Portegies Zwart, S. F., Makino, J., McMillan, S. L. W., & Hut, P. 1999, A&A, 348, 117

Prinja, R. K. 1987, MNRAS, 228, 173

Przybilla, N., Firnstein, M., Nieva, M. F., Meynet, G., & Maeder, A. 2010, A&A, 517, A38

Puls, J., Markova, N., & Scuderi, S. 2008a, 388, 101

Puls, J., Sundqvist, J. O., & Markova, N. 2015, in IAU Symposium, Vol. 307, IAU Symposium, ed. G. Meynet, C. Georgy, J. Groh, & P. Stee, 25–36

Puls, J., Vink, J. S., & Najarro, F. 2008b, A&AR, 16, 209

Quinlan, G. D. & Shapiro, S. L. 1990, ApJ, 356, 483

Ramírez-Agudelo, O. H., Simón-Díaz, S., Sana, H., et al. 2013, A&A, 560, A29

Randich, S. 2009, in IAU Symposium, Vol. 258, IAU Symposium, ed. E. E. Mamajek, D. R. Soderblom, & R. F. G. Wyse, 133–140

Richer, J. S., Shepherd, D. S., Cabrit, S., Bachiller, R., & Churchwell, E. 2000, Protostars and Planets IV, 867

Sabbi, E., Lennon, D. J., Gieles, M., et al. 2012, ApJL, 754, L37

Sabín-Sanjulián, C., Simón-Díaz, S., Herrero, A., et al. 2014, A&A, 564, A39

Salpeter, E. E. 1955, ApJ, 121, 161

Sana, H., de Koter, A., de Mink, S. E., et al. 2013a, A&A, 550, A107

Sana, H., de Mink, S. E., de Koter, A., et al. 2012, Science, 337, 444

Sana, H., Gosset, E., & Evans, C. J. 2009, MNRAS, 400, 1479

Sana, H., van Boeckel, T., Tramper, F., et al. 2013b, MNRAS, 432, L26

Sanyal, D., Grassitelli, L., Langer, N., & Bestenlehner, J. M. 2015, A&A, 580, A20

Schaerer, D., Meynet, G., Maeder, A., & Schaller, G. 1993, A&AS, 98, 523

Schneider, F. R. N., Izzard, R. G., de Mink, S. E., et al. 2014a, ApJ, 780, 117

Schneider, F. R. N., Izzard, R. G., Langer, N., & de Mink, S. E. 2015, ApJ, 805, 20

Schneider, F. R. N., Langer, N., de Koter, A., et al. 2014b, A%A, 570, A66

Schnurr, O., Casoli, J., Chené, A.-N., Moffat, A. F. J., & St-Louis, N. 2008, MNRAS, 389, L38

Schnurr, O., Moffat, A. F. J., Villar-Sbaffi, A., St-Louis, N., & Morrell, N. I. 2009, MNRAS, 395, 823

Schweizer, F. 2004, in Astronomical Society of the Pacific Conference Series, Vol. 322, The Formation and Evolution of Massive Young Star Clusters, ed. H. J. G. L. M. Lamers, L. J. Smith, & A. Nota, 111

Selman, F. J., Espinoza, P., & Melnick, J. 2011, in Astronomical Society of the Pacific Conference Series, Vol. 440, UP2010: Have Observations Revealed a Variable Upper End of the Initial Mass Function?, ed. M. Treyer, T. Wyder, J. Neill, M. Seibert, & J. Lee, 39

Selman, F. J. & Melnick, J. 2001, in Bulletin of the American Astronomical Society, Vol. 33, American Astronomical Society Meeting Abstracts #198, 1181

Selman, F. J. & Melnick, J. 2005, A&A, 443, 851

Smartt, S. J. 2009, A&A, 47, 63

Smith, N. 2013, MNRAS, 429, 2366

Smith, R. J., Longmore, S., & Bonnell, I. 2009, MNRAS, 400, 1775

Soderblom, D. R. 2010, in IAU Symposium, Vol. 268, IAU Symposium, ed. C. Charbonnel, M. Tosi, F. Primas, & C. Chiappini, 359–360

Spruit, H. C. 2002, A&A, 381, 923

Spruit, H. C. 2006, ArXiv Astrophysics e-prints

Stolte, A., Brandner, W., Grebel, E. K., Lenzen, R., & Lagrange, A.-M. 2005, ApJ, 628, L113

Sundqvist, J. O., Owocki, S. P., & Puls, J. 2012, 465, 119

Taylor, W. D., Evans, C. J., Hénault-Brunet, V., et al. 2011, Bulletin de la Societe Royale des Sciences de Liege, 80, 430

Torres, G., Andersen, J., & Giménez, A. 2010, A%ARv, 18, 67

Umeda, H. & Nomoto, K. 2002, ApJ, 565, 385

Vink, J. S. 2011, Ap&SS, 336, 163

Vink, J. S., Brott, I., Gräfener, G., et al. 2010, A&A, 512, L7+

Vink, J. S., de Koter, A., & Lamers, H. J. G. L. M. 1999, A&A, 350, 181

Vink, J. S., de Koter, A., & Lamers, H. J. G. L. M. 2000, A&A, 362, 295

Vink, J. S., de Koter, A., & Lamers, H. J. G. L. M. 2001, A&A, 369, 574

Vink, J. S. & Gräfener, G. 2012, ApJ, 751, L34

Vink, J. S., Muijres, L. E., Anthonisse, B., et al. 2011a, ArXiv e-prints

Vink, J. S., Muijres, L. E., Anthonisse, B., et al. 2011b, A&A, 531, A132

Walborn, N. R., Sana, H., Simón-Díaz, S., et al. 2014, A&A, 564, A40

Woosley, S. E. 1986, in Saas-Fee Advanced Course 16: Nucleosynthesis and Chemical Evolution, ed. J. Audouze, C. Chiosi, & S. E. Woosley, 1

Woosley, S. E. & Heger, A. 2006, ApJ, 637, 914

Yoon, S. & Langer, N. 2005, A&A, 443, 643

Yoon, S.-C., Dierks, A., & Langer, N. 2012, ArXiv e-prints

Yoon, S.-C., Woosley, S. E., & Langer, N. 2010, ApJ, 725, 940

Yorke, H. W. & Sonnhalter, C. 2002, ApJ, 569, 846

Yungelson, L. R., van den Heuvel, E. P. J., Vink, J. S., Portegies Zwart, S. F., & de Koter, A. 2008, A&A, 477, 223

Yusof, N., Hirschi, R., Meynet, G., et al. 2013, MNRAS, 433, 1114

Zinnecker, H. & Yorke, H. W. 2007, A&A, 45, 481

List of Figures

List of Tables

Danksagung

Ich möchte als erstes meinem Betreuer Prof. Norbert Langer danken, für die Möglichkeit meine Dissertation in der Professur Stellar Astrophysics am Argelander-Institut für Astronomie der Universität Bonn anzufertigen. Vielen Dank für die langjährige Betreuung und Unterstützung, sowie die Begutachtung der Dissertation. Des Weiteren möchte ich meinem Zweitgutachter Prof. Thomas Reiprich danken, dass er sich bereit erklärt hat meine Arbeit zu begutachten. Zusätzlichen Dank möchte ich den Mitgliedern der Promotionskommission Prof. Frank Bertoldi und Prof. Klaus Mohr entgegen bringen.

Einen besonderen Dank richte ich an Ines Brott Furrer für die sehr enge Zusammenarbeit. Vielen Dank für all die Hilfestellungen deinerseits und für deine Freundschaft, die weit über unsere Arbeit hinaus ging. Ich konnte immer auf deine Unterstützung zählen, besonderes während der Einarbeitung in das Thema, sowie der Berechnung der Sternenmodelle und der Umsetzung der Populationssynthese warst du mir eine sehr große Hilfe.

Vielen Dank an alle Mitarbeiter der Professur Stellar Astrophysics: Alina, Enrique, Fabian, Herbert, Hilding, Ilka, Jonathan B., Jonathan M., Norbert, Rob, Sasha, Shazrene, Sung-Chul, Thibaut, Thomas und Vincent. Danke für die 3 Jahre, die wir zusammen arbeiten durften. Ich danke euch für eure Unterstützung, die vielen effektiven Diskussionen und Erfahrungen die ich mit euch gesammelt habe. Sie haben mich und meine Arbeit bereichert. Ich habe nicht nur aus fachlicher Sicht sehr viel von euch gelernt.

Im speziellen möchte ich meinen beiden Bürokolleginnen Sasha und Maryam danken, für die schöne Zeit und die vielen gemeinsamen lustigen Stunden. Vielen Dank für eure Hilfsbereitschaft, Freundlichkeit und euer Verständnis. Ich habe sehr gern mit euch beiden zusammen gearbeitet.

Einen weiteren Dank möchte ich meinen Kollegen vom VLT-Flames Tarantula Survey aussprechen. Danke für eure Zusammenarbeit und die rege Unterstützung beim Schreiben der Artikel. Ich habe sehr viel neues von euch gelernt und ich danke euch für die vielen schönen Stunden.

Vielen Dank an Qioptiq Photonics für die Möglichkeit mich seit Anfang 2014 mit meiner neuen Arbeit verwirklichen zu können. Einen ganz besonderen Dank an meine Kollegen (u.a. Gunnar, Ingmar, Jan, Maike, Martin, Nicole, Oliver, Sarah und Tobias) von Coating Center Göttingen für den unglaublich herzlichen Empfang in eurer Gruppe. Vielen Dank für eure Hilfsbereitschaft, euer Verständnis und eure Unterstützung in allen Lebenslagen. Ihr seit mir nicht nur gute Arbeitskollegen, sondern sehr gute Freunde.

Zum Abschluss einen ganz besonderen Dank an meine Familie, sowie unserer Familienfreundin Sandra Geilsdorf. Vielen herzlichen Dank an meinen Mann Markus und unseren Sohn Hendrik, der während meines Promotionsstudiums geboren wurde. Ihr

beide wart mein größter Antrieb. Danke für die seelische Unterstützung, Ermutigung und Geduld, die ihr beide mitbringen musstet. Hendrik - dein Lachen war das größte Geschenk während dieser Zeit. Markus - danke dass du mir immer wieder weitergeholfen hast, mich aufgebaut hast, wenn es nicht so glatt lief. Vielen dank an meine Eltern, Schwiegereltern, Markus und Sandra, dass ihr mich immer wieder ermutigt habt und euch regelmäßig um Hendrik gekümmert habt, damit ich gezielt an der Dissertation arbeiten konnte.

Publikationsliste

- Stenzel, O. and Wilbrandt, S. and Friedrich, K. et. al. 2009, Realistische Modellierung der NIR/VIS/UV-optischen Konstanten dünner optischer Schichten im Rahmen des Oszillatormodells, Vakuum in Forschung und Praxis, 21, 15

- Friedrich, K. and Wilbrandt, S.and Stenzel, O. et. al. 2010, Computational manufacturing of optical interference coatings: method, simulation results, and comparison with experiment, Applied optics, 49, 3150

- Langer, N. and Brott, I. and Cantiello, M et. al. 2010, Massive Stars as Progenitors of SNe & GRBs, Progenitors and Environments of Stellar Explosions

- Lederer, S.M. and French, L.M. and Rohl, D.A. et. al. 2010, Rotation Properties of Three Jovian Trojan Asteroids, AAS/Division for Planetary Sciences Meeting Abstracts # 42

- Bestenlehner, J.M. and Vink, J.S. and Gräfener, G. et. al. 2011, The VLT-FLAMES Tarantula Survey. III. A very massive star in apparent isolation from the massive cluster R136, Astronomy and Astrophysics, 530, L14

- Bischoff, M. and Stenzel, O. and Friedrich, K. et. al. 2011, Plasma-assisted deposition of metal fluoride coatings and modeling the extinction coefficient of as-deposited single layers, Applied optics, 50(9), C232

- Evans, C.J. and Taylor, W.D. and Hénault-Brunet, V. et. al. 2011, The VLT-FLAMES Tarantula Survey. I. Introduction and observational overview, Astronomy and Astrophysics, 530, A108

- Evans, C.J. and Taylor, W.D. and Hénault-Brunet, V. et. al. 2011, VLT-FLAMES Tarantula Survey (Evans+, 2011), VizieR Online Data Catalog, 353, 9108

- Evans, C. and Taylor, W. and Sana, H. et. al. 2011, The VLT FLAMES Tarantula Survey, The Messenger, 145, 33

- de Koter, A. and Sana, H. and Evans, C.J. et. al. 2011, The O stars in the VLT-FLAMES Tarantula Survey, Journal of Physics Conference Series, 328, 012022

- Taylor, W.D. and Evans, C.J. and Sana, H. et. al. 2011, The VLT-FLAMES Tarantula Survey. II. R139 revealed as a massive binary system, Astronomy and Astrophysics, 530, L10

- Köhler, K. and Borzyszkowski, M. and Brott, I. et. al. 2012, Nitrogen chronology of massive main sequence stars, Astronomy and Astrophysics, 544, A76
- Doran, E.I. and Crowther, P.A. and de Koter, A. et. al. 2013, The VLT-FLAMES Tarantula Survey - XI. A census of the hot luminous stars and their feedback in 30 Doradus, Astronomy and Astrophysics, 558, A134
- Köhler, K. and Langer, N. and de Koter, A. et. al. 2015, The evolution of rotating very massive stars with LMC composition, Astronomy and Astrophysics, 573, A71